UNIVERSIDADE FEDERAL DE SANTA CATARINA
PROGRAMA DE PÓS-GRADUAÇÃO EM
ENGENHARIA MECÂNICA

ANÁLISE TEÓRICA E EXPERIMENTAL DA PARTIDA
SUPERCRÍTICA DE TUBOS DE CALOR CRIOGÊNICOS

TESE SUBMETIDA À
UNIVERSIDADE FEDERAL DE SANTA CATARINA
PARA A OBTENÇÃO DO GRAU DE DOUTOR EM
ENGENHARIA MECÂNICA

PAULO COUTO

FLORIANÓPOLIS, 21 DE MARÇO DE 2003

UNIVERSIDADE FEDERAL DE SANTA CATARINA
PROGRAMA DE PÓS-GRADUAÇÃO EM
ENGENHARIA MECÂNICA

ANÁLISE TEÓRICA E EXPERIMENTAL DA PARTIDA
SUPERCRÍTICA DE TUBOS DE CALOR CRIOGÊNICOS

PAULO COUTO

Esta tese foi julgada adequada para a obtenção do título de

DOUTOR EM ENGENHARIA
ESPECIALIDADE ENGENHARIA MECÂNICA

sendo aprovada em sua forma final.

_____

Profª. Márcia B. H. Mantelli, Ph.D. – Orientadora.

_____

Prof. Jay M. Ochterbeck, Ph.D. – Co-orientador.

_____

Prof. José Antonio Bellini da Cunha Neto, Dr. – Coordenador do Curso.

BANCA EXAMINADORA

_____

Profª. Márcia B. H. Mantelli, Ph.D. – Presidente.

_____

Prof. Renato Machado Cotta, Ph.D. – Relator.

_____

Prof. Sérgio Colle, D. Sc.

_____

Prof. Celso Peres Fernandes, Dr. Eng.

_____

Prof. M. Michael Yovanovich, D.Sc.

"A companhia escolhida por nós e que dizemos amar deverá seguir conosco por entre caminhos de espinhos e flores e sempre lado a lado"

À Guadalupe, minha amada esposa, companheira e cúmplice que sempre me apoiou neste trabalho. Devo a ela todo o meu progresso, e nossas famílias têm sido um referencial do que é realmente importante.

Aos meus pais, Décio e Marina, por todo o seu amor e dedicação, e pela maravilhosa educação a mim conferida; e a toda minha família que sempre me apoiou e me incentivou a prosseguir pelos caminhos da carreira acadêmica.

Aos meus sogros, "Seu" Turos e D. Elvira, por tudo o que fizeram, e ainda fazem por mim e por Guadalupe. Eu sou muito grato por seu amor e carinho.

"The one we chose and that we say to love should proceed with us through roads of thorns and flowers and always side by side"

To Guadalupe, my beloved wife, companion and partner that always supported me during this work. I owe her all my progress, and our families have been a referential of what is really important.

To my parents, Décio and Marina, for all their love and dedication, and for the wonderful education they offered me; and to all my family that always supported and motivated me to continue for the paths of the academic career.

To my parents-in-law, Mr. Turos and Mrs. Elvira, for everything that they did, and still do for me and for Guadalupe. I am very thankful for their love and affection.

Agradecimentos

> *"A maravilhosa disposição e harmonia do universo só pode ter tido origem segundo o plano de um Ser que tudo sabe e tudo pode. Isto fica sendo a minha última e mais elevada descoberta".*
>
> Isaac Newton.

Aos amigos Brasileiros, Americanos, Alemães, Franceses, Turcos, Sul-africanos, etc: Samuel, Ana Lígia, e Beatriz. Kupka e Cíntia. Fabrício "Cabeção" Colle e Dani. Rex e Zelita. Milá, Simone, Heitor e Rafaela. Danilo, Simone, Marcelo e Felipe. Alexandre Matelli, Letícia, e Valentina. André Lopes, Anne Delmot, Arthur Gorka, Bahar, Bernardo Rodrigues, Christof Sodke, Curt Wilcox, Donatas Mishkinis, Fernando Pereira, François Maugin, Gabriel Oba, Gabriel Tápia, Guilhermina Torrão, Jackson, Jimmy Stanley, Johann Meulemans, Juan Pablo, Kleber, Manfred Kratzenberg, Manfred Moltz, Marc Spinella, Marcelo Dacorégio, Markus e Virgínia, Michael e Sybil Hughey, Pascal Brocheny, Ralph Natter, Rosângela, Sylvio, Tatiana Guimarães, Thomas Franz, Uzay Damali, Viviane†, e Walid por suas preciosas amizades e palavras de apoio, tão necessárias para vencer as fases mais difíceis deste trabalho.

À todos aqueles que não recordo o nome, mas que de alguma forma contribuíram para a realização deste trabalho.

Acknowledgements

"The wonderful disposition and harmony of the universe might only have had origin according to the plan of a Being that knows and can everything. This is my last and greatest discovery."

Isaac Newton.

Summary

List of Figures

List of Tables

List of Symbols

A	Area [m^2]
B	Constant coefficient
C	Heat capacity (ρc) [J/m^{3}K]
c	Specific heat [J/kg.K]
D	Wire diameter [m]
D_h	Hydraulic diameter [m]
F	View factor
F_{cap}	Capillary force [N]
F_{fric}	Frictional force [N]
F_ℓ	Liquid friction factor [N/W.m^3]
F_v	Vapor friction factor [N/W.m^3]
f	Friction coefficient
g	Gravitational acceleration [m^2/s]
L_{slug}	Liquid slug length [m]
L_{tot}	Total heat pipe length [m]
h	Groove depth [m]
h_{fg}	Latent heat [J/kg]
K	Permeability [m^2]
$K_{\ell,s}$	Non-dimensional conductivity
k	Thermal conductivity [W/m.K]
m	Working fluid mass [kg]
$\dot{m}$	Mass flux [kg/s]
N	Liquid fill rate, Liquid transport factor
P	Pressure [kPa]
Q_e	Heat load [W]

q_p	Parasitic heat load [W]
Re_{Dh}	Reynolds number based on the hydraulic diameter
Re_K	Reynolds number based on the permeability
Re_ℓ	Reynolds number for the liquid flow
Re_v	Reynolds number for the vapor flow
R_g	Gas constant [J/kg.K]
r	radius [m], radial coordinate
r_{eff}	effective pore radius [m]
s	Liquid column length [m]
T	Temperature [K]
T_c	Condenser temperature [K]
T_{crit}	Critical temperature [K]
T_{sat}	Saturation temperature [K]
t	Time [s]
U	Average liquid velocity [m/s]
U_r	Rewetting velocity [m/s]
V	Volume [m^3]
W	Wire spacing [m]
w	Groove width [m]
x	Axial position [m], axial coordinate, quality
Y	Experimental data (temperature) [K]
Z	Compressibility factor
ΔE	Total internal energy change [J]

Greek Symbols:

α_{eff}	Effective thermal diffusivity [m^2/s]
β	Constant coefficient for the working fluid heat capacity
δ	Thickness [m]
μ	Dynamic viscosity [N.s/m^2]
ε	Emissivity
ϕ	Tilt angle [degrees]
φ	Porosity
ρ	Density [kg/m^3]
σ	Surface tension [N/m], Stefan-Boltzmann constant [W/m^{2}K^4]
τ_w	Wall shear stress [N/m^2]

Subscripts:

a	Adiabatic section
E	East volume (finite volume method)
e	Evaporator section
c	Condenser section
crit	Critical point, critical point properties
f	Supercritical/super-heated fluid, supercritical/superheated properties
j	Finite volume index
ℓ	Liquid layer, liquid properties
o	Outer diameter
P	Central volume (finite volume method)
s	Solid wall, solid wall properties
sat	Saturation properties
W	West volume (finite volume method)
w	Wick layer, wick structure.
v	Vapor layer, vapor properties

About the Author

Paulo Couto graduated in Mechanical Engineering in 1996, and achieved Master of Science degree in Mechanical Engineering in 1999 at the Federal University of Santa Catarina, Florianópolis, Brazil. Ph.D. scholar in Mechanical Engineering, beginning in 1999, at the same university, spent one year at Clemson University, South Carolina, USA, as an exchange visitor working on the development of this thesis. Paulo Couto was born in Tubarão, south of Santa Catarina State, south of Brazil, on March 24, 1971.

Abstract

Cryogenic heat pipe is a satellite thermal control device that is used mainly for the thermal control of optical surfaces, infrared-scanning systems, telescopes, and X-ray detectors in the space environment. Actually, investigations are being conducted to include other applications of cryogenic heat pipes, such as the cooling of electronic devices, particularly in microgravity environments. The most recent theoretical and experimental development on the analysis of the supercritical startup of cryogenic heat pipes, carried out at the Satellite Thermal Control Laboratory, at the Federal University of Santa Catarina in cooperation with Clemson University, is presented. This research project was funded by the Brazilian Council for Research and Development – CNPq, CAPES Foundation, and Brazilian Space Agency, as part of the University Program for Space Development. The purpose of this work is to describe the theoretical and experimental techniques used to perform the analysis of the supercritical startup of cryogenic heat pipes under various operational conditions. Although the main text of this thesis is written in English, a synopsis in Portuguese is presented at the end of each chapter.

Chapter 1 presents an introduction to cryogenic heat pipes and to the supercritical startup phenomena. Some basic material and principles of operation of cryogenic heat pipes are presented. This chapter also presents the current and some potential applications of cryogenic heat pipes to various microgravity and ground environment, and the motivation and the goals to this research.

A fundamental understanding of the supercritical startup phenomena of cryogenic heat pipes is necessary to predict the performance of the device during startup. A literature review, including cryogenic heat pipe testing, modeling and supercritical startup analysis are summarized in Chapter 2.

The theoretical analysis of cryogenic heat pipes is presented in Chapter 3. The analysis includes the supercritical startup phenomena analysis, thermal modeling of the heat pipe, and

model validation. The supercritical startup analysis is based on thermodynamic diagrams, such as pressure-specific volume. A one-dimensional thermal modeling of the supercritical startup of cryogenic heat pipes subject to parasitic heat load is presented. A numerical solution of the model was used to predict the transient axial temperature gradient, rewetting velocity, liquid front position, and working fluid pressure. The working fluid temperature is considered to be equal to the adjacent wall temperature. The working fluid pressure is considered essentially uniform and it is estimated based on the wall temperature profile and on the working fluid charge. The thermodynamic properties of the working fluid and heat pipe wall are considered functions of the temperature. The theoretical temperature data obtained with the presented model is in good agreement with microgravity data available at the literature.

Chapter 4 is devoted to the experimental analysis. A design analysis based on the heat transport capacity and on the steady state performance is carried out in order to provide a heat pipe device for ground tests. A precise description of the experimental facility and heat pipe instrumentation is presented. The uncertainty analysis of the measurement systems is discussed to evaluate the accuracy of the experimental data. The experimental procedure, including heat pipe cleaning, assembling, charging and testing is discussed.

The comparison between the experimental data and the theoretical model described in Chapter 3 is presented and discussed in Chapter 5. The experimental data compared well with the theoretical model and provided a good insight of the supercritical startup phenomena.

Finally, Chapter 6 presents the conclusion of the present research and future developments that are still required for the understanding of the supercritical startup phenomena of cryogenic heat pipes.

Keywords: Heat Pipe, Cryogenic Heat Pipe, Supercritical Startup, and Thermal Control.

Resumo

Tubos de calor criogênicos são dispositivos de controle térmico de satélites que são utilizados principalmente para o controle térmico de superfícies ópticas, sistemas de câmeras infravermelhos, detectores de raios-X, e telescópios em ambiente espacial. Atualmente, pesquisas estão sendo realizadas para incluir outras aplicações de tubos de calor criogênicos, como o resfriamento de dispositivos eletrônicos, particularmente em ambientes de microgravidade. Os mais recentes desenvolvimentos teóricos e experimentais sobre a análise da partida supercritica de tubos de calor criogênicos, efetuada no Núcleo de Controle Térmico de Satélites, da Universidade Federal de Santa Catarina em cooperação com a Universidade de Clemson, são apresentados. Este projeto de pesquisa foi financiado pelo Conselho Nacional de Desenvolvimento Científico e Tecnológico – CNPq, Fundação CAPES, e Agência Espacial Brasileira, como parte do Programa Uniespaço. O propósito deste trabalho é descrever as técnicas teóricas e experimentais utilizadas para a análise da partida supercritica de tubos de calor criogênicos sob várias condições operacionais. Embora o texto principal desta tese é escrito em inglês, uma sinopse em português é apresentada ao término de cada capítulo.

O Capítulo 1 apresenta uma introdução sobre tubos de calor criogênicos e sobre o fenômeno da partida supercritica. São apresentados princípios básicos e de operação de tubos de calor criogênicos. Este capítulo também apresenta aplicações atuais e potenciais de tubos de calor criogênicos em ambientes de microgravidade e terrestre, e a motivação e metas para esta pesquisa.

Uma boa compreensão dos fenômenos da partida supercritica de tubos de calor criogênicos é necessária para estimar o desempenho do dispositivo em regime de partida. Uma revisão bibliográfica, incluindo trabalhos sobre experimentos e testes de tubo de calor criogênicos, modelagem e análise da partida supercritica é apresentada no Capítulo 2.

A análise teórica da partida supercrítica de tubos de calor criogênicos é descrita no Capítulo 3. A análise cobre o fenômeno da partida supercrítica, modelagem térmica do tubo de calor, e validação do modelo. A análise da partida supercritica é baseada em diagramas termodinâmicos como, por exemplo, pressão-volume específico. Uma modelagem térmica unidimensional da partida supercrítica de tubos de calor criogênicos sujeitos a cargas térmicas parasitas é apresentada. Uma solução numérica do modelo foi desenvolvida para estimar o gradiente axial de temperaturas em regime transiente, velocidade de molhamento, posição da frente da coluna de líquido, e pressão do fluido de trabalho. A temperatura do fluido de trabalho é considerada igual à temperatura da parede do tubo. A pressão do fluido de trabalho é considerada essencialmente uniforme e é calculada baseada no perfil de temperaturas axial da parede e na carga de fluido de trabalho. As propriedades termodinâmicas do fluido de trabalho e parede de tubo de calor são consideradas como funções da temperatura. Os dados do perfil axial de temperaturas obtidas com o modelo apresentado compararam bem com dados de vôo (microgravidade) disponível na literatura.

Capítulo 4 é dedicado à análise experimental. Uma análise de projeto de tubos de calor criogênicos baseada na capacidade de transferência de calor e na performance do dispositivo em regime permanente é efetuada com o objetivo de dimensionar um tubo para testes laboratoriais. Uma descrição precisa da infraestrutura experimental e instrumentação do tubo de calor é apresentada. Uma análise da incerteza dos sistemas de medidas é descrita para avaliar a precisão dos dados experimentais. O procedimento experimental, incluindo a limpeza do tubo de calor, a montagem, processo de carga e procedimentos de teste são discutidos.

A comparação entre os dados experimentais e o modelo descrito no Capítulo 3 é apresentada e discutida no Capítulo 5. Os dados experimentais compararam bem com o modelo teórico forneceram importantes informações sobre o fenômeno da partida supercritica.

Finalmente, o Capítulo 6 apresenta a conclusão da presente pesquisa e futuros desenvolvimentos ainda necessários para uma melhor compreensão dos fenômenos da partida supercritica de tubos de calor criogênicos.

Palavras chaves: Tubo de calor, Tubo de Calor Criogênico, Partida Supercrítica, e Controle Térmico.

FEDERAL UNIVERSITY OF SANTA CATARINA

**THEORETICAL AND EXPERIMENTAL ANALYSIS OF
SUPERCRITICAL STARTUP OF CRYOGENIC HEAT PIPES**

**THESIS SUBMITTED TO THE
FEDERAL UNIVERSITY OF SANTA CATARINA
FOR OBTAINING THE DEGREE OF DOCTOR IN
MECHANICAL ENGINEERING**

PAULO COUTO

FLORIANÓPOLIS, MARCH 21st, 2003

Chapter 1
Introduction

In 1996, the Satellite Thermal Control Laboratory of the Federal University of Santa Catarina (LABSOLAR/NCTS - UFSC) began the development of a Passive Cryogenic Radiator (Couto, 1999) in the context of the University Program for Space Development (UNIESPAÇO), funded by the Brazilian Space Agency (AEB). Passive Cryogenic Radiators are used to cool down equipments, such as infrared sensors and Charge Coupled Device (CCD) cameras, to the cryogenic temperature levels required for their optimum operation. But, in the most of the satellite designs, the infrared sensor (or the equipment to be cooled) cannot be placed near the cryogenic radiator. Usually, cryogenic heat pipes are used to transfer the heat from these equipments to the cryogenic radiator (Brandt and Schlitt, 1997; Zelenov *et al.*, 1992; Wright, 1980; Wright and Pence, 1973) or any other heat sink (Brennan *et al.*, 1993 and Rosenfeld *et al.*, 1995). In addition, cryogenic heat pipes are used on the thermal control of focal plans of infrared sensors (Voyer *et al.*, 1997), X-ray telescopes (Abrosimov *et al.*, 1992), cooling of superconducting magnets (Ishigohka *et al.*, 1999), among others. The design and analysis of cryogenic heat pipes is now under investigation at the LABSOLAR/NCTS, in order to develop a complete passive cryogenic thermal control device for the payload of the Brazilian satellites described at the Brazilian Policy for Space Activities (*Agência Espacial Brasileira*, 1996).

Heat pipes are highly reliable and efficient heat transfer devices considered for many terrestrial and space applications (Peterson, 1991). This device uses the latent heat of vaporization (condensation and evaporation) of a working fluid to transfer relatively large amounts of energy over a long distance with a small temperature drop. Usually, heat pipes are composed of a sealed container and an inner wick structure, and it is divided into three regions: evaporator section, adiabatic (transport) section, and condenser section. The container of the heat pipe is evacuated and filled with a working fluid. During normal operation, the working fluid remains in a saturation condition, with liquid trapped in the wick structure and vapor in

the core section, named vapor region. The heat flux applied to the evaporator section is conducted through the container wall and wick structure vaporizing the saturated liquid, increasing the local vapor pressure. The vapor resulting from the evaporation process flows through the adiabatic section towards the condenser, where it condenses into the wick, releasing its latent heat of vaporization to the heat sink. The capillary forces developed in the wick structure pumps the working fluid back to the evaporator section. This process continues as long as there is sufficient capillary pressure to drive liquid back to the evaporator (Faghri, 1995). Figure 1.1 shows a schematic of the operational principle of heat pipes.
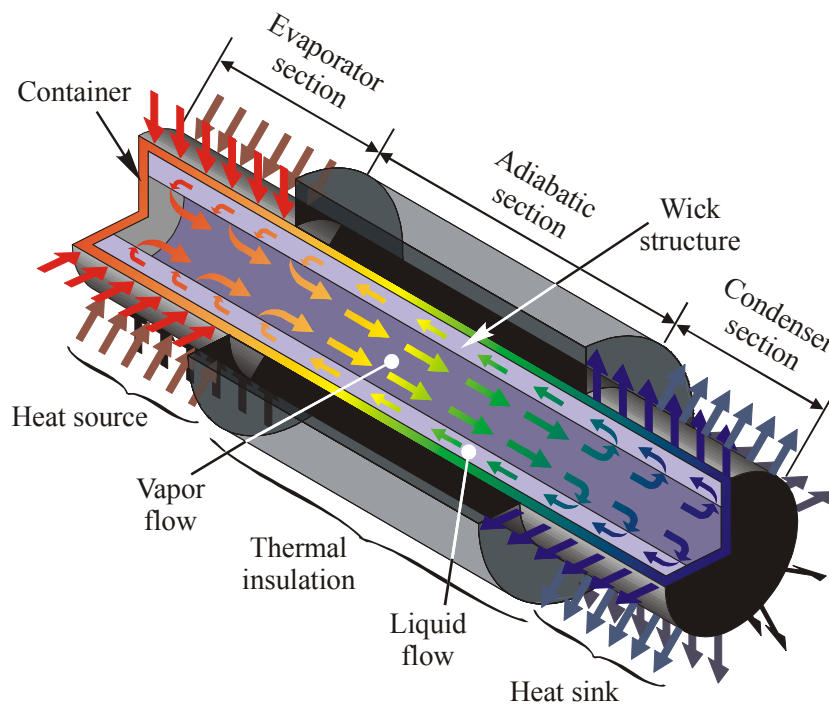
Figure 1.1. Heat pipe operational principle.

1.1 Cryogenic Heat Pipes

Cryogenic technology is advancing rapidly in both space and earth-based applications, and with it comes the need for thermal control devices. Cryogenic heat pipes are one of the many different existing types of devices. Usually they operate at temperatures below 200 K (Faghri, 1995) and their operational temperature range from the triple point temperature to the critical temperature, which is relatively narrow for cryogenic fluids (Barron, 1985). Cryogenic heat pipes are often used for the thermal control of infrared detectors onboard earth observation, astronomy and military satellites (Groll *et al.* 1998). Actually, they have also being used in some terrestrial applications, such as cryosurgeries (Hamilton and Hu, 1993) and superconducting devices (Nakano *et al.* 1996).

Differently from low and medium temperature heat pipes, cryogenic heat pipes start from a supercritical condition. The entire heat pipe must be cooled below its critical point before nominal operation begins. Cryogenic working fluids usually exhibits very low values of surface tension and latent heat of vaporization, resulting in low heat transport capacity heat pipes, which are very sensitive to parasitic heat loads (Couto *et al.* 2002), fluid charge (Röster *et al.*, 1987; Groll *et al.*, 1986) and acceleration fields (Ochterbeck et al, 1995). The parasitic heat loads can change significantly the operational temperature of the cryogenic heat pipe, and may add loads of the order of the maximum transport capability of the heat pipe. In addition, the parasitic heat loads can adversely affect the transient start-up behavior of the system. A little excess of fluid charge may help the startup process as it supplies more liquid to the liquid column, increasing its momentum. In the other hand, an excess of liquid increases the vapor pressure, creating a liquid slug during normal operation that may block part of the condenser, decreasing the heat pipe performance. A deficiency of working fluid is never desirable because it may prevent the heat pipe to prime completely during startup. Acceleration fields, such those provided by orbital attitude adjustments, reboost and docking maneuvers, can cause the redistribution of liquid within the heat pipe, flooding or drying out the evaporator. Acceleration due to gravitational fields (as in ground tests, for example) improves the startup of cryogenic heat pipes as it spreads the liquid slug (developed due to excess of working fluid during the startup) in the wick structure, increasing the momentum of the liquid column.

The most common working fluids used in cryogenic heat pipes are: argon, nitrogen, oxygen, methane, ethane, Freon and helium. These fluids present some problems, such as: low surface tension, low thermal conductivity, low latent heat of vaporization, high viscosity and narrow temperature range (Barron, 1985). Figure 1.2 (adapted from Gilmore, 1994) presents the operating temperature ranges for some cryogenic working fluids. The surface tension and thermal conductivity for some cryogenic fluids are presented in Figure 1.3. In addition, the compatibility of the working fluid and the container must be taken into account to prevent the non-condensable gas formation inside the heat pipe. Non-condensable gas can block part of the condenser, increasing the heat pipe operational temperature. Voyer *et al.* (1997) observed the formation of non-condensable gas in an aluminum/ammonia heat pipe, decreasing in 37 mm the length of the condenser (774 mm). Van Oost and Aalders (1997) observed the formation of non-condensable gas in a stainless steel/methane and stainless steel/ethane heat pipe, affecting 1 % of the heat pipe length. Stainless steel/Nitrogen and aluminum/oxygen presented no generation of non-condensable gases.
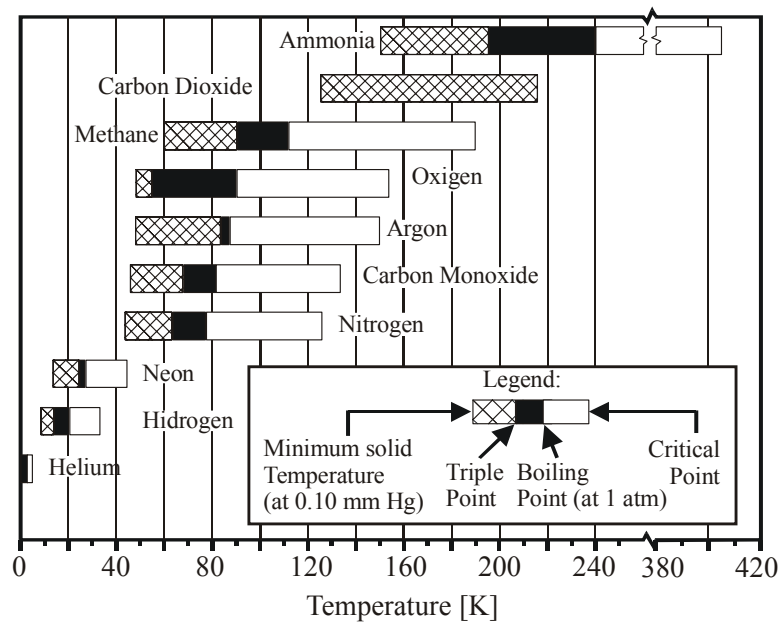
Figure 1.2. Operating temperature ranges for cryogenic fluids (Gilmore, 1994).
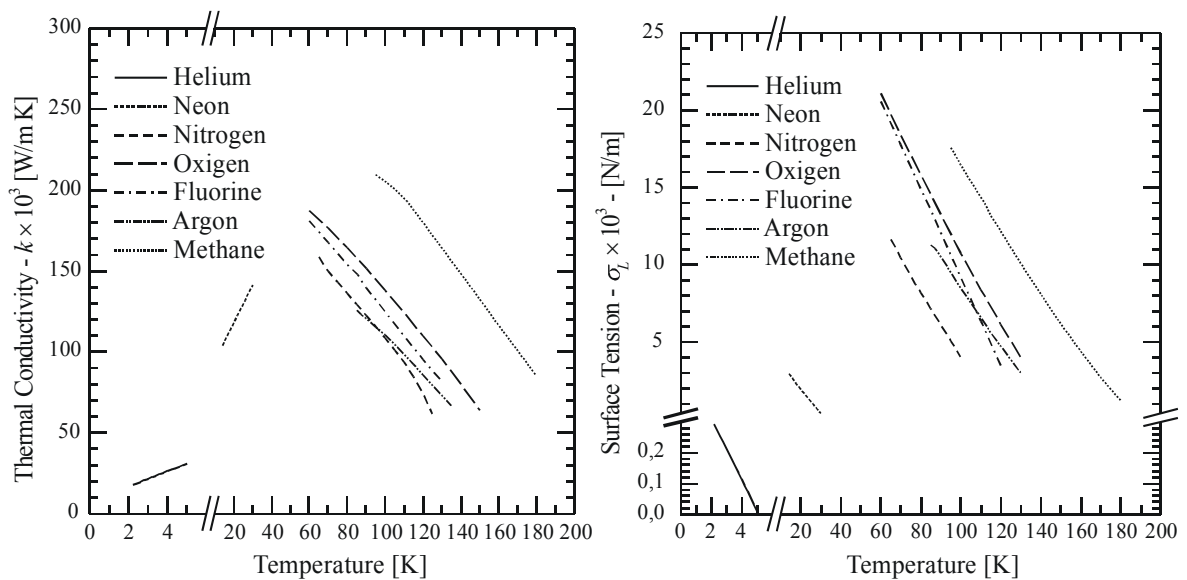
Figure 1.3. Thermal conductivity (left) and surface tension (right) of cryogenic fluids.

1.2   Supercritical Startup of Cryogenic Heat Pipes

The startup of cryogenic heat pipes usually occurs from a supercritical thermodynamic condition (temperature and pressure above the critical point of the working fluid). Therefore, the entire heat pipe must be cooled below the critical point for the condensation process of the working fluid to start in the condenser region (Peterson and Compagna, 1987). A liquid column develops in the wick structure at the condenser section due to the heat sink. As the temperature of the condenser decreases, more vapor condenses and the liquid column advances towards the evaporator end driven by the capillary force developed at the wick, and

opposed by the wall friction. The cooling effect of the liquid vaporization at the liquid column leading edge cools the dry length of the heat pipe, priming the wick structure until steady state operation (Yan and Ochterbeck, 1999).

Although simple, the process presents many details that are not clear. The beginning of the condensation process of the working fluid in the wick structure depends on the thermodynamic state of the fluid, i.e., the temperature and the pressure. It is possible that the supercritical working fluid turns into subcooled liquid before the condensation begins. How the subcooled liquid column would behave? How the gravitational forces affect the supercritical startup? How the parasitic heat loads over the heat pipe wall affect the supercritical startup? What is the limit of parasitic heat loads that the heat pipe can withstand? How does the working fluid charge affect the startup process? In the following chapters of this work, the questions above will be addressed.

1.3   Motivation and Goals

The Brazilian Policy for Space Activities (PNAE), published by the Brazilian Space Agency, is a document that shows an overview of the space activities in Brazil, as well as the proposal of long-term activities, for the period of 1996 at 2005. The programs listed in the PNAE document, especially those involving the development of space technologies, create conditions for the qualification of products and processes with high technological content at the universities and public institutions of R&D, as well as at private companies.

The work described here continues the development of passive thermal control devices, which meet the requirement for cryogenic cooling described in PNAE. Another motivation to this work is the trends of technological development of systems for spacecraft thermal control for the next twenty years (Fisher, 1998). These trends include:

- Costs reduction of short-term future space missions;
- Increase of the concentration of heat dissipation, due to the constant reduction of the size of the space vehicles and to the miniaturization of electronic systems;
- Increase of the needs of systems for refrigeration at cryogenic levels with long-term operational life for interplanetary missions;
- Constant growth of the electric power onboard of satellites. In 1960, the average power was less than 500 Watts; nowadays, satellites with 5 kW are commonly found. Studies already exist for futures satellites with more than 100 kW of power onboard.

To meet these requirements, technological goals are described by Fisher (1998), such as: the increment of the heat transport capacity of the current thermal control systems;

development of reliable devices for cryogenic cooling, such as passive cryogenic radiators and cryogenic heat pipes; development of reliable devices for thermal control, such as folding radiators; and improvement of modeling techniques to help on the development of technological goals. Therefore, the development of cryogenic heat pipes and the study of the process of the supercritical startup of this device, is a contribution to the development of the researches in the area of aerospace thermal control not only in Brazil, but also worldwide.

This work has the main objective to help the development of the technology of cryogenic heat pipes by studying the supercritical startup phenomena, and also the manufacturing, charging and operation processes on the ground, for industrial applications, and on microgravity environment, for space applications.

Other goals are also set for with this work:

1. To develop a mathematical model capable of simulate the transient thermal behavior of cryogenic heat pipes during the supercritical startup process until the steady state operation;

2. To manufacture, to charge and to test heat pipes with nitrogen as working fluid for the Brazilian space program application;

3. To study, simulating the space thermal environment in laboratory, the effects of parasitic heat loads on the transient temperature of cryogenic heat pipes during supercritical startup;

4. To technologically prepare the LABSOLAR/NCTS and its personnel for the development of cryogenic heat pipes.

1.4 Synopsis

Em 1996, o Núcleo de Controle Térmico de Satélites (LABSOLAR/NCTS - UFSC) começou o desenvolvimento de um Radiador Criogênico Passivo (Couto, 1999), no contexto do Programa Uniespaço, financiado pela Agência Espacial Brasileira (AEB). Radiadores Criogênicos Passivos são utilizados para o resfriamento de equipamentos, tais como sensores infravermelhos e câmaras CCD, a níveis criogênicos de temperatura requeridos para sua operação com máxima eficiência. Porém, em muitos casos, o equipamento a ser resfriado (fonte de calor) não pode estar localizado próximo ao radiador criogênico. Geralmente, tubos de calor criogênicos são utilizados para transferir calor do equipamento para o radiador (Brandt and Schlitt, 1997; Zelenov et al., 1992; Wright, 1980; Wright and Pence, 1973). Além disso, tubos de calor criogênicos são usados no controle térmico de planos focais de sensores infravermelhos (Voyer et al., 1997), telescópios de Raios-X (Zelenov et al.

1992), e no resfriando de magnetos supercondutores (Ishigohka et al., 1999). O projeto e desenvolvimento de tubos de calor criogênicos está sob investigação no LABSOLAR/NCTS com o objetivo de desenvolver um dispositivo de controle térmico criogênico totalmente passivo para aplicação nos satélites brasileiros, conforme descreve o Programa Nacional de Atividades Espaciais (Agência Espacial Brasileira, 1996).

Um tubo de calor consiste tipicamente de um invólucro (em geral, um tubo cilíndrico) com as extremidades seladas e com uma estrutura capilar junto à parede interna. Este tubo é evacuado e preenchido com um fluido de trabalho em quantidade suficiente para saturar por completo a estrutura capilar. Uma vez que tubos de calor operam em um ciclo bifásico fechado e que apenas líquido e vapor puro estão presentes dentro do mesmo, o fluido de trabalho permanece em condições de saturação enquanto sua temperatura de funcionamento se mantém entre o ponto triplo e o ponto crítico. Um tubo de calor possui três regiões, a saber: um evaporador, um condensador e uma região adiabática. Quando calor é imposto ao evaporador, o fluido contido na estrutura capilar desta região é aquecido até vaporizar. Com o aumento da pressão de vapor no evaporador, o vapor escoa em direção ao condensador. A remoção de calor nesta região faz com que o fluido condense, liberando calor latente de vaporização. As forças capilares existentes na estrutura capilar bombeiam o fluido ali presente de volta ao evaporador, fechando o ciclo (Faghri, 1995).

Tubos de calor criogênicos operam em temperaturas abaixo de 200 K o que faz este sistema muito sensível a cargas térmicas parasitas provenientes do ambiente circunvizinho (por exemplo, estrutura de satélite). As cargas térmicas parasitas podem alterar significantemente a temperatura operacional do tubo de calor criogênico, e podem acrescentar cargas térmicas ao tubo de calor na ordem da máxima capacidade de transporte de calor. Além de impor cargas térmicas adicionais, as cargas térmicas parasitas podem afetar adversamente a partida deste dispositivo. Adicionalmente, a faixa de temperatura operacional de tubos de calor criogênicos é relativamente estreita. Ao contrário do que ocorre em tubos de calor de baixa e média temperatura, um tubo de calor criogênico tipicamente tem sua partida com o fluido de trabalho em um estado supercritico. O tubo de calor inteiro deve ser resfriado abaixo do ponto crítico do fluido de trabalho antes da operação nominal começar. Para o desenvolvimento e teste de tubos de calor criogênicos, a resposta transiente da temperatura do tubo deve ser bem conhecida.

O trabalho aqui descrito dá continuidade ao desenvolvimento de dispositivos de controle térmico passivo, que atendam às necessidades de resfriamento a níveis criogênicos descritas no PNAE. Outras motivações à realização deste trabalho são as tendências do

desenvolvimento tecnológico de sistemas de controle térmico para os próximos vinte anos (Fisher, 1998). Estas tendências incluem:

- Redução de custos das missões espaciais;

- Aumento da concentração de dissipação térmica, devido à constante redução do tamanho dos veículos espaciais e à miniaturização de sistemas eletrônicos;

- Necessidade crescente de sistemas de refrigeração a níveis criogênicos de vida operacional de longa duração, para missões interplanetárias;

- Constante crescimento da potência elétrica instalada em satélites. Em 1960 a potência média instalada era menor que 500 W. Hoje em dia, são comuns os satélites cuja potência instalada gira em torno dos 5 kW. Já existem estudos para futuros satélites com mais de 100 kW.

Para suprir estas necessidades, metas tecnológicas são descritas por Fischer (1998), tais como: o incremento da capacidade de transporte de calor dos atuais sistemas; desenvolvimento de dispositivos de resfriamento criogênicos confiáveis como radiadores criogênicos e tubos de calor criogênicos; desenvolvimento de dispositivos de controle de temperatura confiáveis, como radiadores dobráveis; e aprimoração das técnicas de modelagem para auxiliar no desenvolvimento de metas tecnológicas. Desta forma, o desenvolvimento de tubos de calor criogênicos e o estudo do processo de partida se constituem em uma contribuição ao desenvolvimento das pesquisas na área do controle térmico aeroespacial não somente no Brasil, mas também no cenário mundial.

Desta forma, este trabalho tem como objetivo básico desenvolver a tecnologia de produção, carga e operação de tubos de calor criogênicos em ambientes de gravidade (para aplicações industriais) e microgravidade (para aplicações espaciais).

Outros objetivos também são almejados com este trabalho:

1. Produzir tubos de calor com nitrogênio líquido como fluido de trabalho para aplicação dentro do programa espacial brasileiro;

2. Desenvolver um modelo matemático capaz de prever o comportamento térmico durante o período da partida supercrítica até o regime permanente de tubos de calor criogênicos;

3. Estudar, simulando as condições térmicas espaciais em laboratório, os efeitos de cargas térmicas parasitas sobre a temperatura de funcionamento do tubo de calor criogênico durante a partida supercrítica dos mesmos;

4. Capacitar tecnologicamente o LABSOLAR/NCTS para o desenvolvimento de tubos de calor criogênicos.

<div align="right">

Chapter 2
Literature Review

</div>

2.1   Introduction

A literature review about cryogenic heat pipes is presented in this chapter. Papers regarding testing and general modeling of cryogenic and low-temperature heat pipes are presented, but emphasis is given to the supercritical startup subject. The review about modeling and testing will provide valuable information for the theoretical and experimental analysis to be discussed in subsequent chapters.

2.2   Supercritical Startup of Cryogenic Heat Pipes

The first publication about cryogenic heat pipes is dated of 1966 when W. L. Haskins demonstrated the technical feasibility of cryogenic heat pipes. Since then, the research about cryogenic heat pipes has increased. The earliest publications dealt about general theory of heat transport capacity, heat transfer limitations and geometry optimization (Joy, 1970; Chi and Cygnarowicz, 1970). Subsequent papers described steady state experiments and applications of cryogenic heat pipes (Wright and Pence, 1973; Alario *et al.*, 1978; Wright, 1980; among many others). These papers will be analyzed later in this chapter. Later, Colwell (1977), Brennan *et al.* (1993), Rosenfeld *et al.* (1995), and Yan and Ochterbeck (1999) have discussed the start-up process of cryogenic heat pipes.

The first publication about the startup of cryogenic heat pipes appeared in 1977 when Gene T. Colwell presented a numerical analysis of the transient behavior of a nitrogen/ stainless steel cryogenic heat pipe with circumferential screen wick structure and composite central slab. The three-dimensional model assumed constant properties, but did not account for the fluid dynamics of the working fluid. Although provisions for simulating a supercritical

startup were included, the author only presented results for the startup of the heat pipe with an initial temperature already below the critical temperature of the working fluid.

A microgravity experiment for two different aluminum/oxygen axially grooved heat pipes (TRW heat pipe and Hughes Aircraft Company heat pipe) was conducted by Brennan *et al.* (1993). The experiment was flown aboard the STS-53 space shuttle mission in December 1992. Reliable startups in flight of the two heat pipes were performed, but the startup process in microgravity was slower than that obtained in ground tests. The authors concluded that in a microgravity environment the condensation of the working fluid develops a liquid slug in the condenser region. In ground tests the excess of liquid spreads in the wick structure due to the effects of the gravitational forces facilitating the startup. In this case, the liquid typically forms a puddle due to the very low surface tension of cryogenic fluids. The TRW heat pipe started successfully after 6 hours at a temperature of 70 K, while the HAC heat pipe started after 6.5 hours at a temperature of 115 K. Although no theoretical modeling of the supercritical startup process was presented, this work provides a good insight on the startup phenomena, such as the formation of a liquid slug in microgravity environment, and experimental comparison between microgravity and ground tests data.

Rosenfeld *et al.* (1995) presented a study of the supercritical startup of a titanium/nitrogen heat pipe. The test was performed during mission STS-62 (March 1994). This heat pipe reached a non-operational steady state thermal condition during microgravity tests. Only 30 % of the heat pipe length cooled below the nitrogen critical point temperature, but the vapor pressure was still above the critical pressure (the vapor pressure was estimated based on the experimental temperature data). However, Rosenfeld *et al.* (1995) observed that in ground tests, the titanium/nitrogen heat pipe underwent startup successfully. The authors concluded that, with the addition of parasitic heat loads, the thermal conduction of the titanium/nitrogen heat pipe was insufficient to allow for the internal pressure to decrease below the critical pressure of nitrogen when in microgravity. The successful startup during ground tests was due to enhanced thermal transport of the gravity-assisted convection/liquid collection effects. These tests highlighted the significance of the parasitic heat loads, as the heat pipe start-up failure would not occur in microgravity if the heat leaks had been significantly reduced. Rosenfeld *et al.* (1995) also first presented the successive thermodynamic states of a cryogenic heat pipe during startup from a supercritical initial condition. From the point of view of these authors "*if the heat pipe could not be cooled sufficiently by radiation or conduction to allow the internal pressure to reach the critical pressure, then a non-operational steady state will be achieved*".

Yan and Ochterbeck (1999) presented a one-dimensional transient thermal model for the supercritical startup of cryogenic heat pipes, which can be summarized into two stages:

1st Stage: In the first stage, the heat pipe is cooled by pure heat conduction, and the vapor temperature at the condenser and pressure is greater than the critical temperature and pressure ($T_c > T_{crit}$, or $P > P_{crit}$). The cooling effect resulting from the condenser heat rejection is not immediately propagated through the heat pipe, but it is confined to a region extending from the condenser to some penetration depth d. Beyond d the temperature gradient is zero. When penetration depth equals the heat pipe length, the cooling effect of the condenser has propagated over the entire heat pipe. Then the temperature of the entire heat pipe decreases.

2nd Stage: In the second stage, the vapor temperature and pressure are lower than the critical temperature and pressure, and the heat conducted to the advancing liquid front cools the heat pipe ($T_c < T_{crit}$, and $P < P_{crit}$). When the condenser temperature is lower than the critical temperature and the internal pressure is lower than the critical point, the vapor begins to condense in the condenser section. The advancing liquid layer is subjected to a capillary driving force that is induced by surface tension and opposed by the wall shear stress, and it advances with an average velocity that will vary with respect to the length of the liquid layer. If the liquid layer is less than the condenser length, the rewetting process is restricted to the condenser. The heat transfer in the remaining sections of the heat pipe is still pure heat conduction. When the liquid front reaches the interface between the condenser and the adiabatic section, two possible cases exists:

- *1st case:* If the liquid average velocity in the condenser is not enough to provide cooling to the dry region, the liquid front will stagnate and will not advance immediately. Thus, the wall temperature in the dry region remains independent of the rewetting.

- *2nd case*: With increasing time, the liquid average velocity in the condenser increases, because the liquid temperature continues to decrease with time, which results in the surface tension increasing, and thus, increasing the capillary driving force. Additionally, the heat flux from the adiabatic section to the condenser decreases, and the latent heat of vaporization increases. Thus, the liquid front eventually will advance again, until the heat pipe reaches its operational steady state.

This model compared favorably with the microgravity experimental data presented by Brennan *et al.* (1993), but it did not include effects of the parasitic heat load over the heat pipe working fluid neither considered the working fluid mass distribution inside the heat pipe. The mass distribution is an important parameter to determine the formation (or not) of a liquid slug during the supercritical startup and to determine the thermodynamic state of the working fluid inside the heat pipe.

2.3 Modeling and Testing Literature Survey

The basic modeling and testing literature were reviewed in this section. The survey provides interesting information and details about modeling and testing of cryogenic heat pipes.

Chi and Cygnarowicz (1970) present a qualitative investigation of the performance of cryogenic heat pipes using different working fluids. A new methodology for design and performance calculation was proposed and the results compared well with Haskins' experiment (1966). The proposed methodology accounted for the temperature variation of the working fluid thermophysical properties.

A study on the optimum design of heat pipes is discussed by Joy (1970). Equations for the optimum wick geometry and maximum heat transport capacity were derived for oxygen and nitrogen heat pipes operating at temperatures from 77 K to 90 K in several gravitational fields, based on the internal diameter of the container. This optimization procedure enabled designers to rapidly examine a number of configurations, in order to determine the one that enables the maximum heat transfer through a given distance, a given fluid and gravitational field. This work, together with Chi and Cygnarowicz (1970), present a good approach for the design of cryogenic heat pipes based on the working fluid properties.

In 1973, Wright and Pence first described the use of cryogenic heat pipes attached to passive cryogenic radiators. The device was able to transport a maximum of 12 Watts from an experimental IR detector at temperatures from 125 K up to 140 K and it used methane as working fluid. The heat transported by the methane heat pipe was spread over the 1.3 m^2 radiator panel by using two "C" shape Freon heat pipes.

An axially re-entrant grooved hydrogen cryogenic heat pipe was described by Alario *et al.* (1978). This research, conducted at NASA-Lewis Research Center, was an effort to make axially grooved heat pipes less tilt sensitive. The container of the heat pipe was made of 6063-T6 aluminum with 20 extruded axial grooves. Each groove had a "key hole" profile with a nominal 0.8 mm diameter liquid flow channel and a 0.2 mm wide open flow channel that connected the grooves to the 9.28 mm diameter vapor core. Although experimental data were not shown, theoretical calculations showed that the re-entrant groove technology could improve in more than 10% the heat transport capacity of axially grooved heat pipes. Also, it was shown that, for cryogenic applications, the re-entrant groove has the additional advantage of requiring less fluid charge, and therefore, resulting in a much smaller storage pressure.

Wright (1980) presented the development of a double-stage passive cryogenic radiator attached to oxygen/aluminum cryogenic heat pipes. Two heat pipes transported heat from the

IR image detector to the radiator 8.1 m² panel. The maximum heat transport capacity of this device was 5 Watts at 70 K.

Groll *et al.* (1986) and Röster *et al.* (1987) performed an experimental and theoretical study on the fluid charge and performance of a methane/stainless steel cryogenic diode heat pipe. It was shown that, starting from a fill charge of 1.2 g the heat transport capacity increases almost linearly with the fluid charge until an asymptotic value is reached for fill charges greater than 2 g. The design mass was 1.7 g. A deficiency of fluid charge decreased the performance of the heat pipe, sometimes leading to a dry-out condition. The methodology to determine the excess of working fluid presented by these authors can be easily adapted to cryogenic heat pipes.

Edelstein and Kosson (1991) presented steady state experimental data for a re-entrant grooved heat pipe similar to that shown by Alario *et al.* (1978). Two configurations were tested: methane/aluminum for cryogenic temperatures and ammonia/aluminum for room temperatures. The maximum heat transport capacity of the methane/aluminum heat pipe was 165 W m at a temperature of 115 K, which was an order of magnitude higher than the state-of-the-art of cryogenic heat pipe technology at that time. The ammonia/aluminum heat pipe operated at 283 K with a maximum heat transport capacity of 735 W m.

Abrosimov *et al.*, Barantsevich and Gutkin, and Zelenov *et al.* described in 1992 the use of cryogenic heat pipes for cooling of electronic equipment in the Russian space program. No theoretical modeling was presented by these authors, and the experimental data presented are poor, but these papers shows the application of cryogenic heat pipes for the cooling of electronic equipments at microgravity environment.

Voyer *et al.* (1997) described the application of cryogenic heat pipes in the European astronomy satellite INTEGRAL. Two aluminum/ammonia axially grooved heat pipes were used to transport a maximum heat load of 20 Watts to an intermediate radiator stage at 210 K. Tests have shown the reliability of the ammonia heat pipe to work close to its freezing point (down to 197 K) and its ability to thaw within a few minutes using the right procedure.

A long-life testing program performed by SABCA (Belgium) under an ESA contract is summarized by Van Oost and Aalders (1997). The long-life test was performed from January 1981 to November 1994 for methane and ethane stainless steel heat pipes, and from November 1985 to November 1994 for oxygen and nitrogen stainless steel heat pipes. Two different geometries were tested, as follows: heat pipe type A − $\varnothing_{out}$: 6.4 mm; $\varnothing_{in}$: 5.33 mm; heat pipe type B − $\varnothing_{out}$: 3.2 mm; $\varnothing_{in}$: 2.36 mm. Both geometries had a length of 1000 mm. The summary of the heat transport capacity of each heat pipe tested is shown in Table 3.1. Some conclusions were summarized by the authors: the heat transport capacity and the

maximum tilt capacity of all the heat pipes were not affected by the long-life test program; the evaporator heat transfer coefficient (gradient between the evaporator and the condenser inlet) remained constant during test; neither corrosion nor incompatibility between the container material and the working fluid were observed for the oxygen and nitrogen stainless steel heat pipes, which were TIG-welded (their condenser remained isothermal along the ageing period); a small amount of non-condensable gas were generated at the methane and ethane stainless steel heat pipes (which were hard-brazed) affecting 1% of the heat pipe length. Although no modeling is presented by these authors, the paper provides interesting information about the performance of different configurations of cryogenic heat pipes.

Table 2.1. Summary table of cryogenic heat pipe performance.

Heat Pipe Type[1]	Temperature Range [K]	Fluid	Year of Manufacturing	Start of Ageing	Q_{max}/Temp.	Tilt$_{max}$/Temp.
A	100 / 170	Methane	1980	1981	2.6 W / 129 K	16.5 mm / 137 K
B	100 / 170	Methane	1980	1981	0.55 W / 138 K	26 mm / 133 K
A	123 / 293	Ethane	1980	1981	3.5 W / 193 K	32 mm / 150 K
B	123 / 293	Ethane	1980	1981	1.2 W / 193 K	27 mm / 181 K
A	53 / 118	Nitrogen	1985	1985	2.2 W / 85 K	5.6 mm / 102 K
B	53 / 118	Nitrogen	1985	1985	0.44 W / 85 K	8 mm / 101 K
A	63 / 148	Oxygen	1985	1985	3.2 W / 85 K	8 mm / 100 K
B	63 / 148	Oxygen	1985	1985	0.42 W / 101 K	8 mm / 94 K

2.4 Transient Analysis Literature Review

For the cryogenic heat pipe transient thermal analysis, some modeling techniques available on the literature were examined (Faghri, 1995; Yan and Ochterbeck, 1999; Tournier and El-Genk, 1994(a) and 1994(b); Colwell and Chang, 1983 and 1985; and Bowman, 1991). Faghri (1995) presents a variety of models, from lumped to two-dimensional, which accounts for a sudden change on the heat input during normal operation of the heat pipe.

Yan and Ochterbeck (1999) used an approximated method (integral method) to solve their one-dimensional supercritical startup model (already mentioned in sec. 2.2). The method provided a simple solution that compared well with experimental data (Brennan *et al.*, 1993).

A two-dimensional transient model for a fully thawed heat pipe is presented by Tournier and El-Genk [1994(a) and 1994(b)]. This model determines the axial temperature profiles of the working fluid and heat pipe wall, axial vapor and liquid pressure profiles, and the effective radius of curvature of the liquid meniscus at the liquid-vapor interface. The

---

[1] Type A – Material: Stainless Steel; $\varnothing_{out}$: 6.4 mm; $\varnothing_{in}$: 5.33 mm; Length: 1000 mm; Type B – Material: Stainless Steel; $\varnothing_{out}$: 3.2 mm; $\varnothing_{in}$: 2.36 mm; Length: 1000 mm.

authors considered a metallic screen wick structure, and the liquid flow in the wick structure is modeled using the Darcy Law model (Nield and Bejan, 1992). The model was numerically solved, and provided a good insight on the liquid flow modeling in porous media. Theoretical results showed good agreement with experimental data provided by the authors.

A study on the transient thermal behavior of a low temperature heat pipe is discussed by Colwell and Chang (1983 and 1985). The authors used a numerical formulation of the problem considering a finite difference method and a heat balance on the tube wall and metal screen wick. Again, the liquid flow in the wick structure is modeled using the Darcy flow model (Nield and Bejan, 1992). Although previsions for a supercritical startup were included, predictions were shown for an initial temperature equal or below the critical temperature and were not compared to experimental data. Colwell and Chang (1985) stated that the "*transient normal operation can be predicted accurately using transient heat conduction equations applied to the shell* (container) *and to the combination fluid-capillary structure with appropriate initial and boundary conditions. Under adverse conditions* (i.e., supercritical startup)*, account must be taken of internal fluid dynamics, and predictions become much more difficult*".

A comparison among numerical methods for the transient modeling of heat pipes is summarized by Bowman (1991). Bowman stated that "*time-accurate results could be obtained even if the heat pipe's wall model and the heat pipe's vapor model use different time steps to march through time*". This leads to a reduction in computer time requirements by as much as a factor of 500. Implicit methods were tested and shown to be 10 times faster than the explicit methods. Theoretical results compared well with experimental data.

Zuo and Faghri (1998) presented an analysis of the physics behind the heat pipe operation using a network of thermal resistances and a working fluid cycle. The transient behavior was described by first-order linear ordinary differential equations, and a temperature-entropy diagram was used to show the working fluid thermodynamic cycle. This is a simple model to determine the temperature of each component of the heat pipe and the comparison with experimental data of a copper-water heat pipe was good. A new dimensionless number was presented for the first time. It relates the geometry of the heat pipe (dimension group of parameters - Φ) with the thermophysical properties of the heat pipe wall and working fluid (thermophysical properties group of parameters - Θ). It was shown that, for the heat pipe proper operation Φ must be greater than Θ.

The priming process is a very important phenomenon in the supercritical startup of cryogenic heat pipes. Starting from a supercritical condition, the working fluid condenses only after the condenser region of the heat pipe reaches its critical temperature and pressure. The condensed liquid in the wick structure has to prime the entire heat pipe before normal

operation begins. Ochterbeck *et al.* (1995) presented a rewetting model for heat pipes undergoing externally induced accelerations. The analysis is based on a momentum balance of the saturated liquid column, which is subjected to a capillary driving force and opposed by the wall shear stress provided by the wick structure. The proposed model investigated the rewetting process of a heat pipe after an external acceleration had caused a redistribution of the working fluid. Although this methodology was developed for an existing saturated liquid column, it can be easily applied to the priming process of a heat pipe undergoing a supercritical startup, as it was performed later by Yan and Ochterbeck (1999).

The characterization of the wick structure of the heat pipe is another important parameter to be investigated. The characterization of axially grooved heat pipes can be found in Peterson (1991) and Faghri (1995). The heat transfer characteristics in metal screen wick heat pipes are discussed by Imura *et al.* (1988 and 1994). Correlations for the heat transfer coefficient and maximum heat transfer rate due to capillary limitation for a water/stainless steel heat pipe were proposed and benchmarked against experimental data. Expressions for the permeability, porosity and effective pore radius were also derived.

2.5 Summary and Conclusions

A literature review on cryogenic heat pipes was performed in this section. Several papers discussing the supercritical startup phenomena, testing, transient modeling, and correlated subjects were presented for heat pipes and cryogenic heat pipes. The objective was to gather as many information as possible about cryogenic heat pipe. Some conclusions can be summarized:

1. Cryogenic heat pipes are very sensitive to parasitic heat loads, gravity field accelerations, and fluid mass charge. The fluid mass and the prediction of parasitic heat loads must be taken into account during the design of cryogenic heat pipe devices.

2. The compatibility between oxygen and aluminum, oxygen and stainless steel, nitrogen and stainless steel, hydrogen and aluminum was observed in the literature with no formation of non-condensable gases.

3. The characterization of the wick structure is a very important parameter for the design of cryogenic heat pipes. The wick structure must be able to provide enough capillary pressure to prime the heat pipe during the supercritical startup process.

4. The temperature variation of the cryogenic working fluid thermophysical properties affects the performance of heat pipes and must be taken into account for the transient modeling of the supercritical startup phenomena.

2.6 Synopsis

A primeira publicação sobre tubos de calor criogênicos data de 1966 quando W. L. Haskins (1966) demonstrou a viabilidade técnica do funcionamento de tubos de calor criogênicos. As primeiras publicações tratam sobre a teoria geral da capacidade e limitações da transferência de calor, assim como da otimização da geometria de tubos de calor criogênicos (Joy, 1970; Chi e Cygnarowicz, 1970). Trabalhos posteriores tratam de experimentos em regime permanente e de aplicações de tubos de calor criogênicos (Wright, 1980; Wright e Pence, 1973; Alario et al., 1978; entre muitos outros). Previamente, Colwell (1977), Brennan et al. (1993), Rosenfeld et al. (1995), e Yan e Ochterbeck (1999) discutiram o processo de partida de tubos de calor criogênicos.

Um dos trabalhos mais relevantes na área da partida supercrítica de tubos de calor criogênicos foi publicado em 1999 por Yan e Ochterbeck (1999), que apresentaram um modelo analítico unidimensional transiente para modelar o fenômeno da partida em tubos de calor criogênicos ranhurados axialmente. Segundo estes autores, este fenômeno pode ser resumido em duas etapas:

1a. etapa: Primeiramente, o tubo de calor é resfriado por condução pura através da parede do tubo. A temperatura e pressão do vapor no condensador são maiores do que a temperatura e pressão críticas. O efeito do resfriamento no condensador não se propaga por todo o tubo de calor, mas somente até uma região que se estende do condensador até uma certa profundidade de penetração. Além desta profundidade, o gradiente de temperaturas é zero. Quando esta profundidade de penetração é igual ao comprimento de todo o tubo de calor, o efeito do resfriamento se propagou por todo o tubo e a temperatura do dispositivo diminui como um todo.

2a. etapa: Com o efeito do resfriamento do condensador propagado por todo o tubo, a temperatura e a pressão do vapor diminuem até um valor abaixo da temperatura e pressão criticas. Quando isto ocorre, o vapor se condensa na região do condensador formando uma película de líquido na estrutura capilar. Esta película de líquido está sujeita a forças capilares induzidas pela tensão superficial do fluido e oposta às tensões de cisalhamento no fluido, avançando na direção do evaporador com uma velocidade que varia com o comprimento desta película. Se o comprimento da película de líquido é menor que o comprimento do condensador, o processo de molhamento da estrutura capilar pelo fluido condensado é restrito somente a esta seção. O processo de transferência de calor nas demais seções do tubo de calor é puramente condutivo. Quando o comprimento da película de líquido atinge o comprimento do condensador, dois casos podem ocorrer:

1o. caso: Se a velocidade média com que a película de líquido avança na direção do condensador não for suficiente para promover o resfriamento da região seca (região adiabática e evaporador do tubo de calor), a película de líquido ficará estagnada e não avançará de imediato. Desta forma a temperatura na região seca permanece independente do processo de molhamento.

2o. caso: Com o passar do tempo, a velocidade da película de líquido no condensador aumenta, pois a temperatura do condensador continua diminuindo, aumentando assim a tensão superficial, e assim, aumentando as forças capilares. Adicionalmente, o fluxo de calor axial da região adiabática para o condensador diminui, e o calor latente de vaporização aumenta. Assim, o comprimento da camada de líquido começará a avançar até o tubo de calor atingir seu regime permanente operacional.

Os dados obtidos com este modelo comparam favoravelmente com os dados experimentais apresentados por Brennan et al. (1993), mas o modelo não incorporou os efeitos hidrostáticos, que auxiliam o processo de partida em ambientes de 1-g, nem os efeitos de cargas térmicas parasitas.

Para uma modelagem coerente da partida supercrítica de tubos de calor criogênicos, foram revisados trabalhos que discutem a modelagem básica e testes de tubos de calor disponível na literatura. A pesquisa forneceu informações precisas e detalhadas sobre modelagem e testes de tubos de calor criogênicos. O objetivo de reunir o maior número de informações possível sobre tubo de calor criogênico foi alcançado e algumas conclusões podem ser resumidas:

1. Tubos de calor criogênicos são muito sensíveis a cargas térmicas parasitas, campos gravitacionais, e carga de fluido de trabalho. A massa de fluido de trabalho e uma estimativa precisa das cargas térmicas parasitas são parâmetros importantes para o projeto de tubo de calor criogênicos.

2. A compatibilidade entre oxigênio e alumínio, oxigênio e aço inox, nitrogênio e aço inox, hidrogênio e alumínio, foi observada na literatura, ou seja, não houve formação de gases não-condensáveis.

3. A estrutura capilar é um parâmetro muito importante para o projeto de tubos de calor criogênicos. A estrutura capilar deve ser selecionada de forma a proporcionar suficiente pressão capilar para o processo de molhamento do tubo de calor durante o processo de partida supercrítica.

4. A variação das propriedades termofísicas do fluido de trabalho com a temperatura pode afetar o desempenho do tubo de calor e deve ser levada em consideração durante o processo de modelagem dos fenômenos da partida supercrítica.

3.1   Introduction

In this section a theoretical analysis of the supercritical startup of axially grooved and porous sintered metal wick cryogenic heat pipe is performed. The analysis is done by the use of pressure-specific volume diagrams to help on the determination of the heat pipe thermodynamic state at any point in time during the startup. Based on this analysis, a thermal model of the cryogenic device is presented. The model accounts for the vapor pressure of the working fluid, condensation of the working fluid in the wick structure, and fluid mass distribution inside the heat pipe. A list of all the parameters used for the solution of the model is summarized in the Appendix A. On the sequence, some theoretical results obtained with the model are compared to experimental data available in the literature (Brennan *et al.* 1993 and Rosenfeld *et al.* 1995). At the end, some conclusions about the model are presented.

3.2   Supercritical Startup Analysis

The supercritical startup of axially grooved and porous sintered metal wick cryogenic heat pipes is considered. The initial temperature of the heat pipe, T_0, is homogeneous and is above the critical temperature. The boundary condition at the condenser region is a specified time-variable temperature $[T_c = f(t)]$. This boundary condition is consistent with most microgravity experiments in the literature (Cowell, 1977; Brennan *et al.*, 1993; Rosenfeld *et al.*, 1995), which use cryocoolers to provide the required heat rejection at the condenser region. The remaining length of the heat pipe (adiabatic and evaporator regions) is considered to be under the effect of a radiative parasitic heat load. This parasitic heat load is provided by the radiative heat transfer between the heat pipe wall and the spacecraft structure, and heat loads from the space environment (*e.g.*, direct sun irradiation, earth infrared emission and albedo, etc.). Figure 3.1 shows the schematic of the physical model, as well as the boundary conditions and the coordinate system.

$$q = \sigma \varepsilon A F_{HP,\infty}(T_\infty^4 - T^4)$$

$T_c = f(t)$

Condenser | Transport section | Evaporator

$x = -L_c$ $x = 0$ $x = L_e$ $x = L$
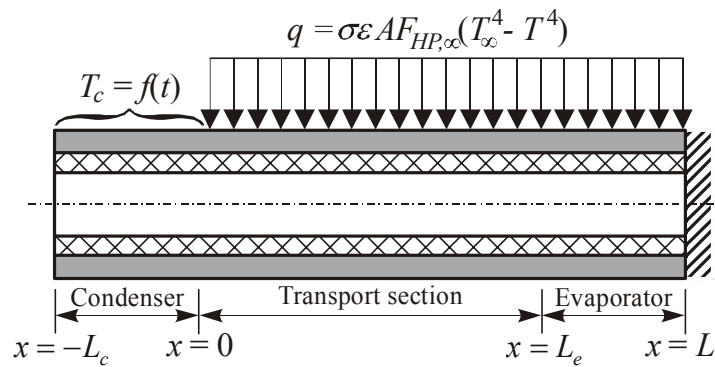
Figure 3.1. Physical model and coordinate system.

As the heat pipe's initial condition is a homogeneous temperature above the critical temperature, the working fluid is in a supercritical thermodynamic condition. Therefore, with the working fluid mass and the void volume of the heat pipe known, it is possible to determine the specific volume of the working fluid and, therefore, the initial vapor pressure. When the startup process begins, a temperature gradient develops at $x = 0$ (see Figure 3.1) because the cooling effect resulting from the condenser heat rejection is not propagated throughout the entire heat pipe. Considering the pressure of the working fluid essentially uniform, the axial temperature gradient induces a distribution of working fluid mass inside the heat pipe. As temperature and density are inversely related for a given pressure, the greater the temperature gradient between $x = 0$ and $x = L$, the lower the density and so, the greater is the working fluid mass pushed into the condenser region ($-L_c < x < 0$). Also, the working fluid pressure decreases as the startup process proceeds because the temperature of the entire heat pipe is decreasing.

Depending on the initial condition of the heat pipe, the working fluid at the condenser region may achieve a subcooled condition first than a saturated condition. The current analysis considers two cases for the initial condition: the initial specific volume of the heat pipe is much larger than the critical specific volume of the working fluid ($v_{HP} \gg v_{crit}$), or the specific volume is less or near the critical specific volume ($v_{HP} < v_{crit}$ or $v_{HP} \sim v_{crit}$). These cases are discussed now.

3.2.1 Case 1 – $v_{HP} \gg v_{crit}$

The first case can be understood by observing the pressure-specific volume diagram shown in Figure 3.2. At the beginning of the process the heat pipe is considered to be isothermal at T_0, where the initial condition of the heat pipe is represented by point 1 in the supercritical region. As the start-up proceeds, the thermodynamic state of the heat pipe is

represented by a horizontal line of uniform pressure. This line lowers as the pressure of the vapor decreases due to the heat rejection at the condenser region. In Figure 3.2, point 2a represents the specific volume at the condenser end, and point 2b represents the specific volume at the evaporator end (which are at different temperatures due to the temperature gradient existing at $x = 0$). It is important to observe, at the thermodynamic state 2, that the vapor pressure is lower than the critical pressure, but the temperature of the condenser remains above the critical temperature. As the temperature of the condenser continues to decrease, the condenser will enter the superheated region when the temperature of the condenser decreases below the critical temperature, or $T_c < T_{crit}$. The condensation process will start when the temperature of the condenser equals the saturation temperature (point 3b) at the vapor pressure at point 3b $[T_c = T_{sat}(P_v) \equiv P_v = P_{sat}(T_c)]$. In this moment, liquid condenses at the wick structure (point 3a), and saturated vapor fills the vapor space at the condenser region (point 3b). The remaining length of the heat pipe remains dry in a superheated condition (line 3b − 3c). As the temperature of the condenser continues to decrease (line 4a − 4b − 4c), more liquid condenses in the wick structure, increasing the momentum of the liquid column, which eventually advances towards the evaporator. The process continues until the heat pipe is completely primed, and the thermodynamic state at the wick structure and vapor space is given by points 5a and 5b, respectively.
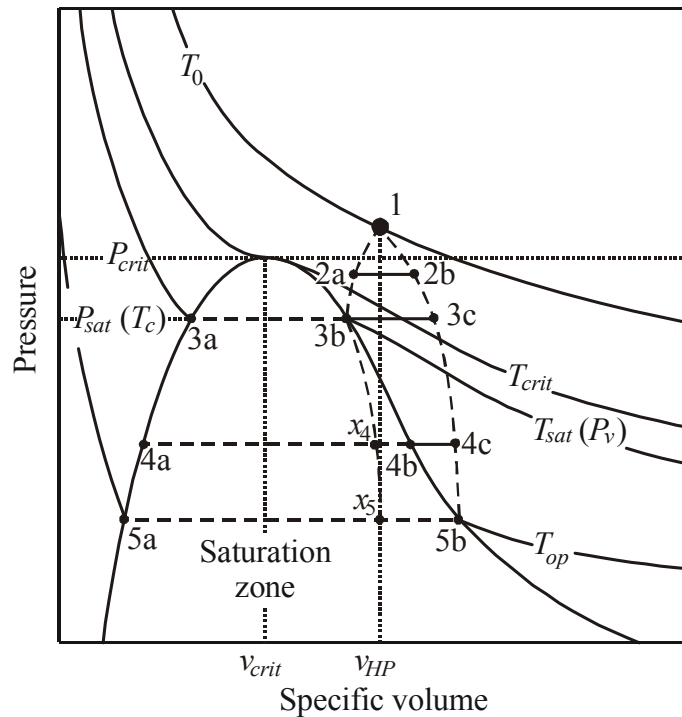
Figure 3.2. Pressure-specific volume diagram for $v_{HP} \gg v_{crit}$.

3.2.2 Case 2 – $v_{HP} < v_{crit}$ or $v_{HP} \sim v_{crit}$

The second case can be understood by observing the pressure-specific volume diagram shown in Figure 3.3 and the thermodynamic states schematics shown in Figure 3.4. At the beginning of the process the initial condition of the heat pipe is represented by point 1. In this case, as the startup continues, the condenser will reach the critical temperature before the vapor pressure decreases below the critical pressure, at point 2a. At this point, the vapor inside the condenser region changes from supercritical fluid to subcooled liquid because its temperature is below the critical temperature, but the vapor pressure is still greater than the critical pressure ($T_c < T_{crit}$ and $P_v > P_{crit}$). On the absence of gravitational forces, the subcooled liquid fills the wick structure and the vapor space in the condenser region forming a subcooled liquid slug. As the temperature of the condenser decreases, this slug extends into the transport section until the vapor pressure equals the critical pressure at point 3c. At point 3b, the leading edge of the subcooled slug will be at a critical condition once the local temperature and pressure are equal to the critical temperature and pressure ($T\big|_{x=L_{slug}} = T_{crit}$ and $P_v = P_{crit}$). From this point on, the length of the subcooled liquid slug decreases until the condenser temperature reaches the saturation pressure at that point in time [$T_c = T_{sat}(P_v)$] at point 4a. At this point, the condenser region is filled with saturated working fluid: saturated liquid at the wick structure (point 4a) and saturated vapor at the vapor space (point 4b). The remaining length of the heat pipe remains dry, in a superheated condition (point 4c). As the temperature of the condenser continues to decrease (line 5a – 5b – 5c), more liquid condenses,
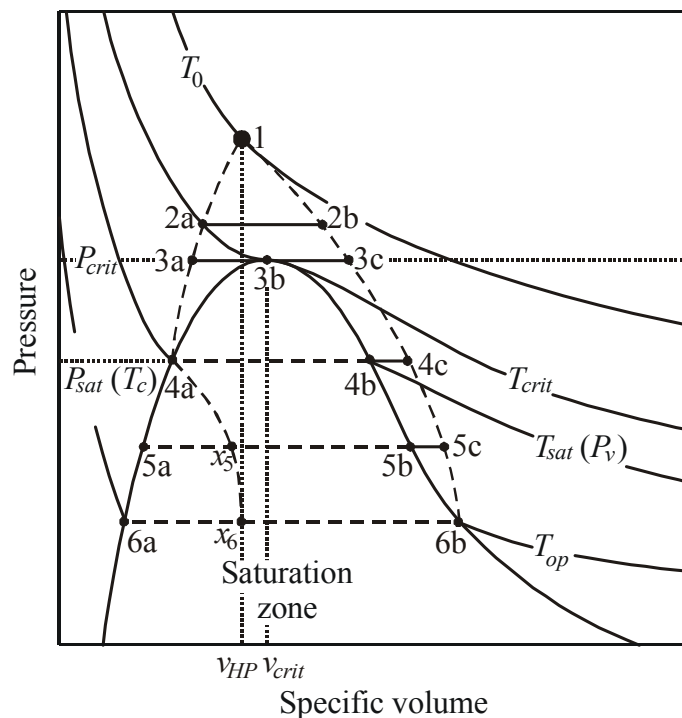
Figure 3.3. Pressure-specific volume diagram for $v_{HP} < v_{crit}$.

(Thermodynamic state: 1 - supercritical)

Wick structure   Vapor region

1

Condenser | Transport section | Evaporator

(State: 2 - subcooled/supercritical)

2a•   •2b

(State: 3- subcooled/critical interface/supercritical)

3a•   3b•   •3c

(State: 4 - saturated/superheated)

•4a
•4b   •4c

(State: 5 - saturated/superheated)

•5a
•5b   •5c

(State: 6 - saturated)

•6a
•6b
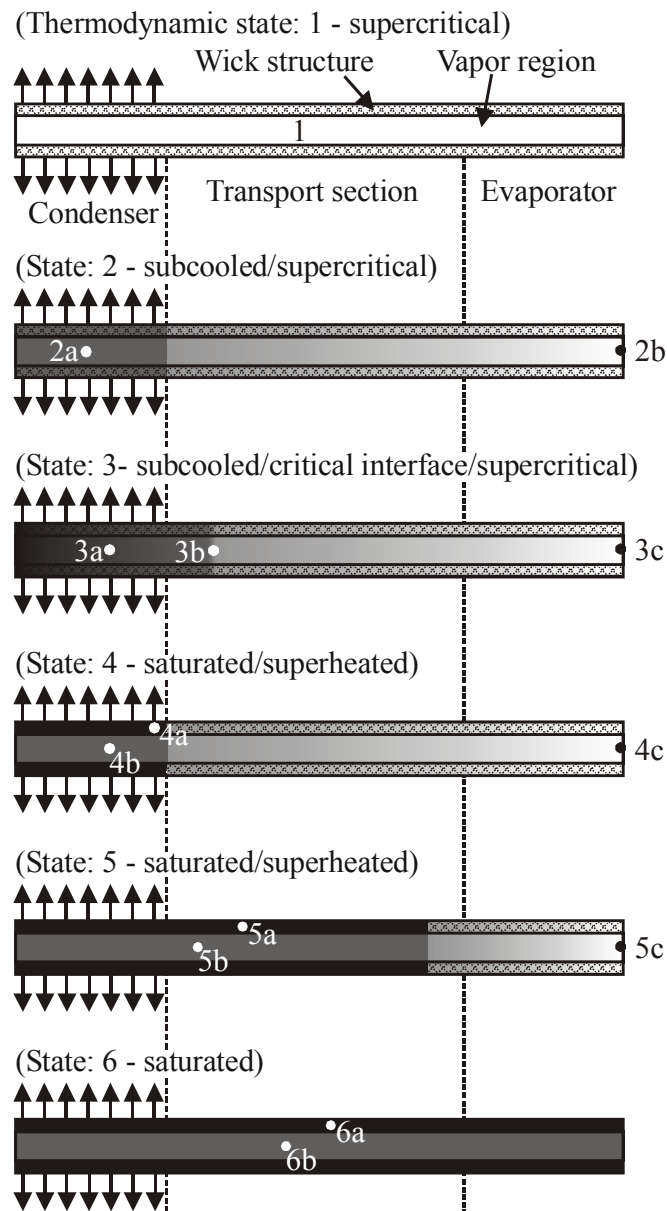
Figure 3.4. Thermodynamic state schematics for $v_{HP} < v_{crit}$.

increasing the momentum of the liquid column, which eventually advances towards the evaporator. The process continues until the heat pipe is completely primed and the thermodynamic state at the wick structure and vapor region is given by points 6a and 6b, respectively.

3.3 Thermal Model

The thermal model of the supercritical startup of cryogenic heat pipes consists of the following models: conductive for the heat pipe wall, liquid column, and a vapor pressure, all solved for two stages. In the 1st stage, the heat pipe contains only supercritical vapor and the primary mechanism of heat transfer is conduction. In this case, the conductive model is used to determine the axial temperature profile. When the condensation of working fluid occurs in

the condenser region (2nd stage), the conductive model and the liquid column model are solved together to determine the axial temperature profile and the liquid column length. The vapor pressure model is iteratively used to determine the working fluid pressure. The vapor pressure and temperature at the condenser region are used as parameters to determine the beginning of the condensation process. Following, all the models are presented in separate subsections.

3.3.1 Heat Transfer Model: 1st Stage

Initially, the heat pipe contains only supercritical vapor and the temperature at the condenser is specified. According to Figure 3.1, as the condenser temperature is considered to be uniform, the origin of the coordinate system used for the modeling of the supercritical start-up of the cryogenic heat pipes is located at the interface between the condenser and the transport sections. The heat conduction at the dry region of the heat pipe wall and wick structure is one-dimensional, and the thermal conduction through the working fluid is negligible when compared to that through the heat pipe wall. The one-dimensional heat conduction equation for the physical model presented in Figure 3.1 is given by:

$$\frac{\partial[(\rho c)_{eff} T]}{\partial t} = \frac{\partial}{\partial x}\left(k_s \frac{\partial T}{\partial x}\right) + \frac{\sigma \varepsilon A F_{HP,\infty}(T_\infty^4 - T^4)}{V_s}; \text{ for } 0 < x < L \text{ and } t > 0 \qquad (3.1)$$

where $(\rho c)_{eff}$ is the effective heat capacity of the heat pipe, k_s is the conductivity of the container material, A is the external area of the heat pipe container from $x = 0$ to $x = L$, ε is its emissivity, $F_{HP,\infty}$ is the view factor between the tube and the surrounding environment, T_∞ is the temperature of the environment, and V_s is the volume of the container wall, T is the axial temperature distribution [$T(x,t)$], and σ is the Stefan-Boltzmann constant. The second term on the right hand side of Eq. (3.1) accounts for the radiative parasitic heat load impinging on the heat pipe external wall. To account for the heat capacity of the working fluid, Yan and Ochterbeck (1999) added to the heat capacity of the solid wall a constant coefficient that accounts for the total change of the internal energy from the initial state at T_0 to the final state at T_f for the heat pipe wall and the working fluid. This coefficient was defined as:

$$\beta = (\Delta E_s + \Delta E_f)/\Delta E_s \qquad (3.2)$$

and the effective volumetric heat capacity was defined as:

$$C_{eff} = (\rho c)_{eff} = (1 + \beta)\rho_s c_s \tag{3.3}$$

where ΔE_s and ΔE_f are the total internal energy change from the initial state to the final state for the heat pipe wall and the working fluid respectively, ρ_s is the wall material density, and c_s is its specific heat . The internal energy for the working fluid can be easily obtained from thermodynamic tables. The internal energy for the heat pipe wall can be obtained from the following relation:

$$\Delta E_s = V_s \int_{T_0}^{T_f} \rho_s c_s dT \tag{3.4}$$

To evaluate the integral of Eq. (3.4) the variation of the density and the specific heat of the solid wall as a function of temperature are required. They can be obtained from thermophysical properties tables available in the literature.

The initial condition for Eq. (3.1) is assumed as a constant temperature T_0 for the entire heat pipe length. The boundary conditions at the interface between the condenser and the transport section is a time-variable temperature given by the cryocooler, $T_c = f(t)$, while the evaporator end is considered to be insulated:

$$T = T_0; \text{ for } t = 0 \text{ and } 0 \leq x \leq L \tag{3.5}$$

$$T = T_c(t); \text{ for } x = 0 \text{ and } t > 0 \tag{3.6}$$

$$\frac{\partial T}{\partial x} = 0; \text{ for } x = L \text{ and } t > 0 \tag{3.7}$$

3.3.2 Heat Transfer Model: 2nd Stage

When the vapor pressure inside the heat pipe equals the saturation pressure at a given condenser temperature $[P_v = P_{sat}(T_c)]$ at that point in time, vapor begins to condense at the wick structure, and a liquid column develops inside it (the vapor pressure model will be discussed later). Saturated liquid flows within the liquid column with an average velocity U. Once the wick structure is filled with saturated liquid, the liquid column will advance in the direction of the evaporator end with a rewetting velocity U_r. At the leading edge of the liquid column, liquid is vaporized because the dry region of the heat pipe is at a higher temperature. Also, the parasitic heat load will vaporize some liquid along the column. If the summation of

the parasitic heat load and the heat supplied by the dry region is greater than that heat needed to vaporize the entire advancing liquid column, the rewetting process will stagnate. The total length of the liquid column is s, and its temperature is considered to be uniform and equal to the temperature of the heat pipe wall. At the condenser, this temperature is equal to the cryocooler temperature. Figure 3.5 shows the physical model for the supercritical startup considering the rewetting process of the liquid column.
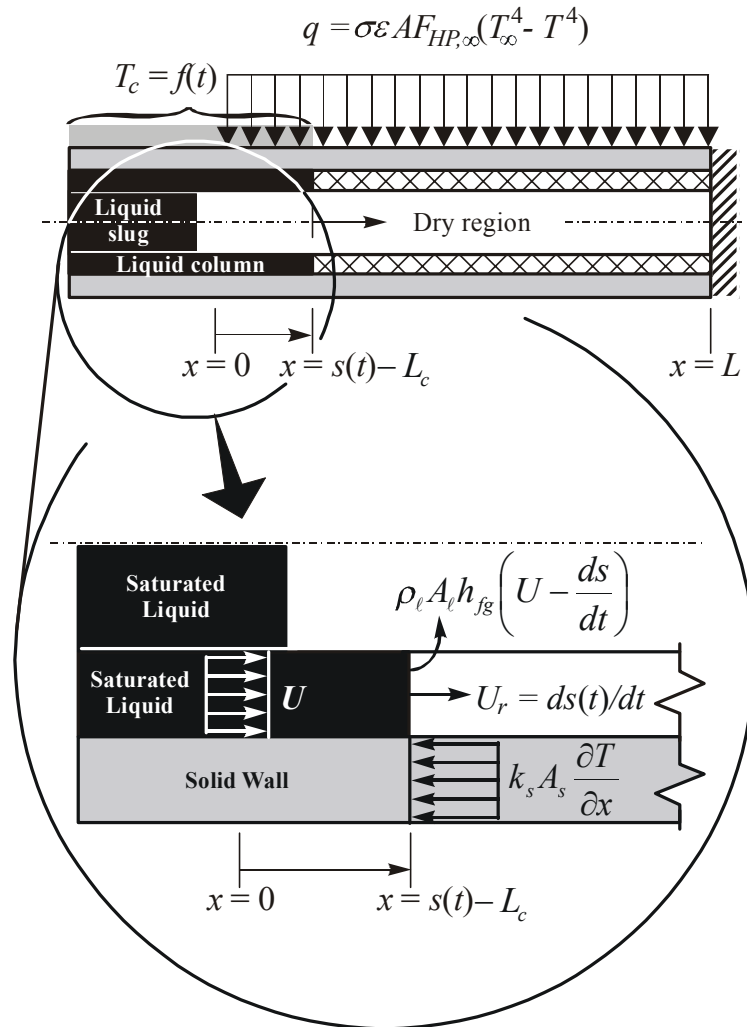
Figure 3.5. Physical model and coordinate system.

The one-dimensional heat transfer equation for the dry region of the physical model presented in Figure 3.5 [$s(t) - L_c < x < L$] is Eq. (3.1). Now, as the liquid column eventually moves towards the evaporator end, the boundary condition for this stage is considered to be a moving boundary condition at the position $x = s(t) - L_c$ where L_c is the condenser length:

$$T = T_c(t) \; ; \; \text{for } x = s(t) - L_c \text{ and } t > 0 \tag{3.8}$$

The position of the liquid column s can be obtained as a function of t by a heat balance at the leading edge of the liquid column, as follows:

$$\left(k_s A_s \frac{\partial T}{\partial x} \right)_{x=s-L_c} = \left[\rho_\ell A_\ell h_{fg} \left(U - \frac{ds}{dt} \right) \right]_{x=s-L_c} \tag{3.9}$$

where ρ_ℓ is the density of the saturated liquid, A_ℓ is the groove cross sectional area, h_{fg} is the latent heat of vaporization of the working fluid, and ds/dt is the velocity that the liquid column advances, *i.e.*, the rewetting velocity U_r. The initial condition is given as $s = L_c$ at the time that the condensation process of the working fluid begins in the wick structure.

3.3.3 Liquid Column Model

The liquid column is modeled according to the methodology presented by Ochterbeck *et al.* (1995). In this case, two rewetting processes are considered: the rewetting process of a rectangular groove (Brennan *et al.*, 1993), and the rewetting process of a porous sintered metal wick (Rosenfeld *et al.*, 1995). A momentum balance is performed at the liquid column, and the total liquid column is taken as the control volume. The advancing liquid column is subjected to a capillary driving force induced by the surface tension, and is opposed by the wall shear stress:

$$F_{cap} - F_{fric} = \frac{d(m_\ell U)}{dt} \tag{3.10}$$

where m is the mass of the liquid column, and U is the average velocity of the liquid inside the column.

3.3.3.1 Model for Axial Grooves

For axial grooves, the capillary driving force and the wall shear stress are given by the following expressions (Peterson, 1994):

$$F_{cap} = \frac{2\sigma h w}{r_{eff}} \tag{3.11}$$

$$F_{fric} = \tau_w s(2h + w) \tag{3.12}$$

where σ is the surface tension of the working fluid, h is the groove thickness, w is the groove width, r_{eff} is the pore effective radius, τ_w is the wall shear stress, and s is the length of the

liquid column. For an axial groove the effective pore radius is taken to be the main dimension perpendicular to the liquid column motion, *i.e.*, the groove height (Ochterbeck et al, 1995):

$$r_{eff} = h \tag{3.13}$$

Assuming that the liquid flow is laminar and Newtonian, the wall shear stress for an axial groove is given by (Faghri, 1995):

$$\tau_w = \frac{\rho_\ell U^2 f}{2} \tag{3.14}$$

where ρ_ℓ is the density of the saturated liquid, U is the average velocity of the advancing liquid film, and f is the friction factor, given by:

$$f = \frac{16}{\mathrm{Re}_{D_h}} \tag{3.15}$$

The Reynolds number based on the hydraulic diameter is given by:

$$\mathrm{Re}_{D_h} = \frac{\rho_\ell U D_h}{\mu_\ell} \tag{3.16}$$

where μ_ℓ is the saturated liquid viscosity and D_h is the hydraulic diameter, defined as (Faghri, 1995):

$$D_h = \frac{4hw}{2h + w} \tag{3.17}$$

Substituting Eqs. (3.11) through (3.17) into Eq. (3.10) yields the following expression:

$$2\sigma w - 2\mu_\ell \frac{(2h + w)^2}{hw} sU = \rho_\ell hw \frac{d(sU)}{dt} \tag{3.18}$$

Note that the saturated liquid mass, m_ℓ, can be written in terms of the saturated liquid density, ρ_ℓ, times the liquid column volume.

According to the physical model shown in Figure 3.5, the initial condition associated with Eq. (3.18) is:

$$s = 0 \text{ at } t = 0 \tag{3.19}$$

Eq. (3.18) is solve for sU, providing:

$$sU = \frac{\sigma h}{2\mu_\ell}\left(\frac{w}{2h+w}\right)^2\left\{1 - \exp\left[-2\frac{\mu_\ell}{\rho_\ell}\left(\frac{2h+w}{hw}\right)^2 t\right]\right\} \tag{3.20}$$

Analyzing Eq. (3.20), the rewetting time (time when the rewetting process of the heat pipe's dry region begins) can be determined by setting $s = L_c$, and solving the resulting equation for t. Previous calculations showed that this time is large enough to vanish the exponential term on Eq. (3.20), resulting in a simpler equation relating U and s:

$$U = \frac{\sigma h}{2\mu_\ell s}\left(\frac{w}{2h+w}\right)^2 \tag{3.21}$$

The average liquid velocity U obtained from Eq. (3.21) refers to an unheated groove. The parasitic heat load applied to the heat pipe wall will cause some working fluid to evaporate from the liquid column. Therefore, a mass balance in the liquid column is performed between $x = 0$ and $x = s(t) - L_c$ to obtain the corrected value for the velocity U at the column leading edge:

$$\frac{dm_\ell}{dt} = \dot{m}\Big|_{x=0} - \dot{m}_{evap} \tag{3.22}$$

or:

$$\rho_\ell A_\ell \frac{ds}{dt} = \rho_\ell U\Big|_{x=0} A_\ell - \frac{q_p'' A_{evap}}{h_{fg}} \tag{3.23}$$

where A_{evap} is the area where evaporation occurs along the liquid column length. The ds/dt term in Eq. (3.23) is the corrected average velocity of the liquid column, while U (in the first term on the right hand side) is the average velocity as given by Eq. (3.21). The evaporation mass flux in Eq. (3.22) is a function of the parasitic heat load, and it provides a relation between the velocity U and the parasitic heat load q_p that affects the liquid column:

$$U = \frac{\sigma h}{2\mu_\ell L_c}\left(\frac{w}{2h+w}\right)^2 - \frac{q_p''[2\pi r_v(s-L_c)]}{\rho_\ell A_\ell h_{fg}} \tag{3.24}$$

It is clear that if there is no parasitic heat load, Eq. (3.24) reduces to Eq. (3.21). Equation (3.24) is valid for heated axial rectangular grooves.

3.3.3.2   Model for Porous Sintered Metal Wicks

For porous sintered metal wick structures, the capillary driving force and the wall shear stress are given by the following expressions (Faghri, 1995):

$$F_{cap} = \frac{2\sigma\varphi A_w}{r_{eff}}$$ (3.25)

$$F_{fric} = \tau_w \frac{4\varphi A_w s}{D_h}$$ (3.26)

where φ is the porosity and A_w is the cross sectional area of the wick structure. The effective pore radius is given by the following expression (Faghri, 1995):

$$r_{eff} = \frac{d}{2(1-\varphi)}$$ (3.27)

where d is the metal fiber diameter.

Assuming that the liquid flow is laminar and Newtonian, the wall shear stress is identical to Eq. (3.14). The friction factor for a porous wick structure is written in terms of the Reynolds number based on the permeability K (Bejan, 1995):

$$f = \frac{1}{\mathrm{Re}_K}$$ (3.28)

$$\mathrm{Re}_K = \frac{\rho_\ell U K^{1/2}}{\mu_\ell}$$ (3.29)

The hydraulic diameter for porous sintered metal wicks is given by (Faghri, 1995):

$$D_h = \frac{d\varphi}{1-\varphi}$$ (3.30)

For porous sintered metal wick structures, the porosity and the permeability are usually obtained experimentally.

Substituting Eqs. (3.25) through (3.30) into Eq. (3.10) yields the following expression:

$$\frac{4\sigma\varphi}{\rho_\ell D_h} - \frac{2}{D_h K^{1/2}} \frac{\mu_\ell}{\rho_\ell} sU = \frac{d(sU)}{dt}$$ (3.31)

which can be solved using the initial condition given by Eq. (3.19) to obtain:

$$sU = \frac{2\sigma\varphi K^{1/2}}{\mu_\ell}\left[1 - \exp\left(-2\frac{\mu_\ell}{\rho_\ell D_h K^{1/2}}t\right)\right] \tag{3.32}$$

for the sintered metal wick structure. Again, if the rewetting time is sufficiently large, the exponentials on Eq. (3.32) vanishes, yielding:

$$U = \frac{2\sigma\varphi K^{1/2}}{\mu_\ell s} \tag{3.33}$$

Correcting the velocity of the liquid column in the porous sintered metal wick structure to account for the effects of the parasitic heat load in the same fashion as used for the axial grooves, the final expression that relates the average velocity of the liquid column and the liquid column position is:

$$U = \frac{2\sigma\varphi K^{1/2}}{\mu_\ell s} - \frac{q_p''[2\pi r_v(s - L_c)]}{\rho_\ell A_\ell h_{fg}} \tag{3.34}$$

Again, if there is no parasitic heat load, Eq. (3.34) reduces to Eq. (3.33). Equation (3.34) is valid for a heated porous sintered metal wick structure.

3.3.4 Vapor Pressure Model

The vapor pressure can be obtained by using the following thermodynamic relation:

$$P = Z\rho_f R_g T \tag{3.35}$$

where P is the pressure, Z is the compressibility factor, ρ_f is the density of the fluid, R_g is the gas constant and T is the wall temperature. As the vapor pressure is considered essentially constant, and as the temperature of the heat pipe varies axially, the specific volume must vary axially so that the conservation of the working fluid mass in the heat pipe is satisfied. Thus, the process to determine the vapor pressure is iterative. First, the heat pipe length is divided into J finite volumes, and a vapor pressure is guessed for each time step. Equation (3.35) is then solved for each one of the finite volumes to determine the density of each volume, including the condenser. Then, the mass of fluid in each volume is obtained from:

$$m_j = V_j \rho_j \tag{3.36}$$

The total mass is given by the summation of the mass of each volume:

$$m_f = \sum_{j=0}^{J} m_j \tag{3.37}$$

If the mass obtained from Eq. (3.37) is different than the real fluid mass of the heat pipe (design parameter), another pressure is guessed until the mass conservation inside the heat pipe is reached. Figure 3.6 shows the flow chart for the vapor pressure model. When the temperature of the condenser is below the critical temperature, the pressure of the heat pipe is compared to the saturation pressure at the condenser temperature, $P_{sat}(T_c)$. If the pressure equals the saturation pressure at that condenser temperature, then the condensation process begins, i.e.:

$$P_v = P_{sat}(T_c) \tag{3.38}$$
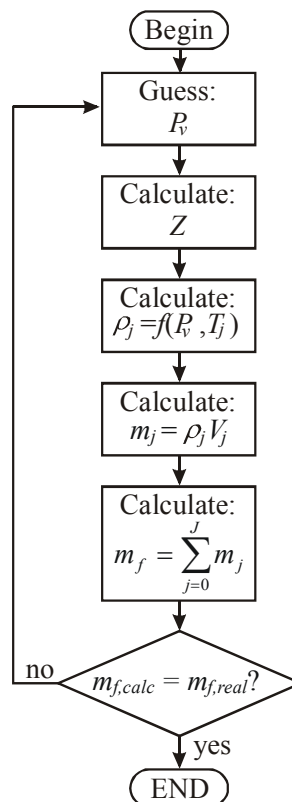
for the beginning of the condensation process.

Figure 3.6. Vapor pressure model flow chart.

3.3.5 Thermophysical Properties

For an accurate solution, the thermophysical properties of the working fluid must be accurately evaluated during the startup process as a function of the wall temperature and vapor pressure. The thermophysical properties required for the model solution are: superheated and supercritical density of the vapor, compressibility factor, density of the saturated liquid and vapor, latent heat of vaporization and viscosity of the saturated liquid and vapor. The methodology presented by Jacobsen *et al.* (1997) is used to obtain the thermophysical properties of the working fluid. This methodology is based on a fundamental equation, function of the dimensionless Helmzoltz energy parameter. Data for oxygen are presented by Schmidt and Wagner (1985), Stewart *et al.* (1991), and Jacobsen *et al.* (1997). Data for nitrogen are presented by Jacobsen *et al.* (1986) and Jacobsen *et al.* (1997).

The thermophysical properties for the heat pipe solid wall container were least square fitted using experimental data available at the literature. Details on the calculation of the thermophysical properties of the working fluid and solid wall can be found in Appendix B

3.3.6 Model Solution

As Eq. (3.1) is non-linear in temperature due to the parasitic heat load term, a numerical solution based on the finite volume method described by Patankar (1981) was used. The heat pipe length was divided into J volumes, and Eq. (3.1) was integrated inside each volume to provide implicit equations for the temperature. The general form of the equation is given by:

$$T_j^0 = A_{j-1}T_{j-1} + A_j T_j + A_{j+1}T_{j+1} + B_j \tag{3.39}$$

where A_j , A_{j-1} , A_{j+1} and B_j are constant coefficients, T_j^0 is the temperature in the last time step, T_j , T_{j-1} and T_{j+1} are the unknown temperatures. A Taylor Series was used to linearize the source term of Eq. (3.1). Details about the discretization of Eq. (3.1) are available in Appendix C.

Equation (3.39) allows the problem to be written in a matrix form as follows:

$$[T^0] = [A][T] + [B] \tag{3.40}$$

where the matrix **[T]** is unknown. The solution is found from:

$$[T] = [A]^{-1}\{[T^0]+[B]\} \tag{3.41}$$

As Equation (3.1) includes the thermophysical properties of the heat pipe container (density, conductivity and specific heat), the solution is iterative. First, the temperature of the condenser (boundary condition) is calculated for a given time t. The thermophysical properties are then evaluated based on the last temperature profile available. A new temperature profile is obtained from the solution of Eq. (3.1). The process is repeated until convergence is achieved. Figure 3.7 shows the flow chart for the temperature calculation.
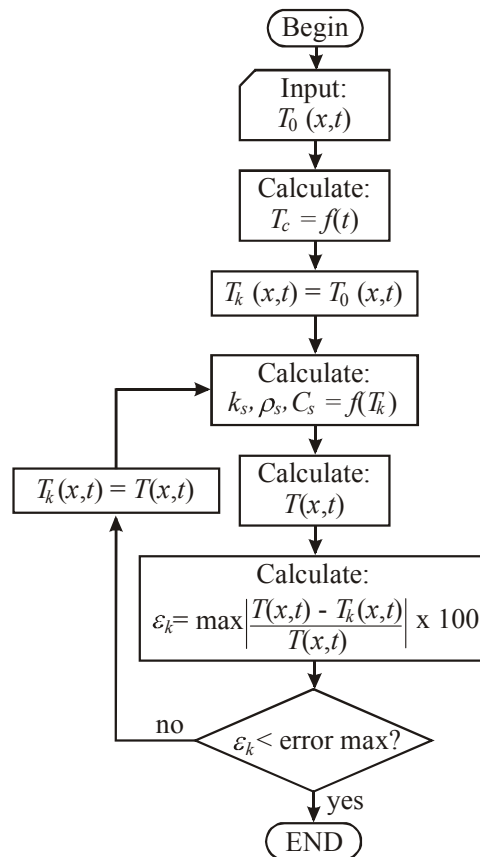
Figure 3.7. Temperature (Eq. 4.1) solution flow chart.

Figure 3.8 shows the complete solution flow chart for the supercritical startup model. The inputs for the model are:

- Initial temperature of the heat pipe,
- Heat pipe geometry,
- Container material,
- Type of working fluid, and
- Time variation of the condenser temperature (boundary condition).

The solution begins with the data input. Then the initial density (ρ_0) and pressure (P_0) of the heat pipe are calculated. A time step is performed and the condenser temperature (T_c) and thermophysical properties of the solid wall are evaluated based on the last temperature profile available.

For the 1st stage of the start-up process, the Eq. (3.41) is solved (Figure 3.7) to obtain the axial temperature profile [$T(x, t)$]. Then, the vapor pressure (P_v) is obtained from the vapor pressure model (Figure 3.6). The process is repeated for successive time steps until the condition for the beginning of the condensation process is achieved [Eq. (3.38), $P_v = P_{sat}(T_c)$].

For the 2nd stage solution, Eq. (3.41) using the last temperature profile available as initial condition. The axial temperature profile calculation is iterative because it depends on the liquid column position, which depends on the temperature gradient at the liquid column edge. First, the temperature of the condenser (T_c) is obtained and the average velocity of the condensed liquid column (U) is calculated based on the last liquid column position (s) available. The new liquid column position (s) is calculated based on the last average liquid column velocity (U) and temperature gradient ($\partial T/\partial x|_{x=s}$) available. Based on the liquid column position, the new axial temperature profile is obtained Eq. (3.41). The convergence between two successive iterations is checked for each finite volume, and the maximum deviation (ε_k) is considered. The following relation is used to evaluate the deviation:

$$\varepsilon_k = \max\left|\frac{T_{k,j} - T_j}{T_j}\right| \times 100 \qquad (3.42)$$

where $T_{k,j}$ and T_j are the temperatures for each j volume in the last and actual iteration respectively. The convergence is achieved when the maximum deviation is less then 0.01, which corresponds to less than 0.005 K of error on the axial temperature. Once an accurate temperature profile is available, the vapor pressure (P_v) is calculated (Figure 3.6).

Two criteria are used for the end of the model:

1. If the liquid column reaches the evaporator end, the heat pipe will be isothermalized and its temperature will be given by the cryocooler heat sink capacity.

2. An non-operational steady state[2] is reached when the temperature variation between two successive time steps is less than 1 K/h, according to the following relation:

$$\varepsilon_t = \max\left|\frac{T_j - T_{j,0}}{\Delta t}\right| \times 3600 \qquad (3.43)$$

where T_j and $T_{j,0}$ are the temperatures for each volume in the actual and last time step respectively , and Δt is in seconds.

---

[2] A non-operational steady state is reached when the liquid column stagnates before the evaporator end ($s < L_{tot}$). The liquid column stagnation can occur due to several reasons, such as excessive parasitic heat load and deficiency of working fluid mass. The stagnation of the liquid column will be discussed later.

Figure 3.8. Solution flow chart.

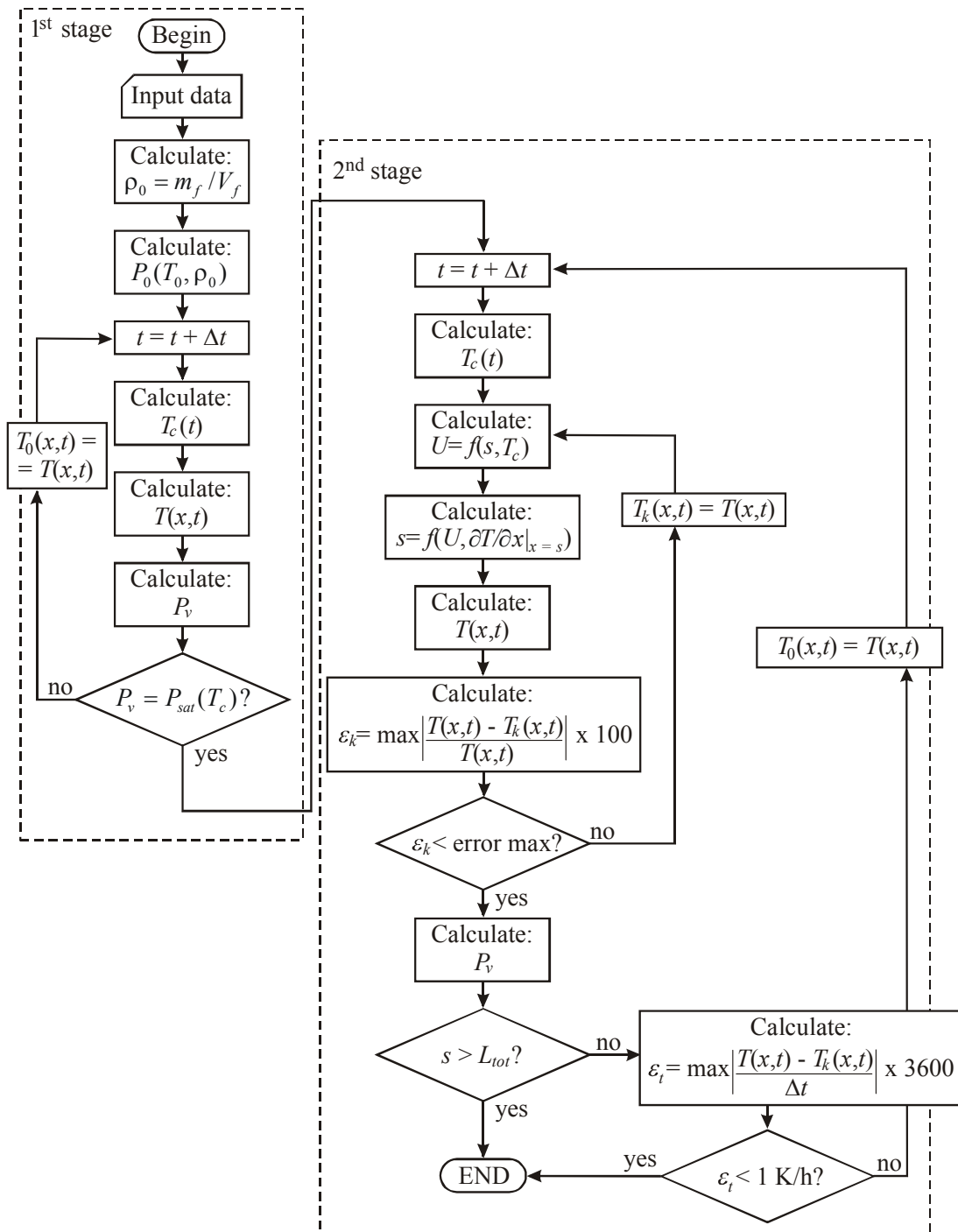## 3.4 Model Validation

For the validation of the model, the experimental data of two axially grooved aluminum/oxygen cryogenic heat pipes – TRW heat pipe and HAC heat pipe (Brennan *et al.* 1993), and a sintered metal wick titanium/nitrogen cryogenic heat pipe – NHP (Rosenfeld *et al.* 1995) were used. The TRW and HAC heat pipe parameters are shown in Table 3.1, and those of the NHP, in Table 3.2.

Table 3.1. TRW and HAC Heat Pipes' Design Summary (Brennan *et al.* 1993)

Design Parameter	TRW	HAC
Tube material:	Aluminum Alloy, 2024-T6	
Tube dimensions:		
Outer diameter	11.2 mm	15.91 mm
Vapor diameter	7.37 mm	8.64 mm
Wall thickness	1.02 mm	2.54 mm
Lengths:		
Evaporator	0.15 m	0.15 m
Condenser	0.15 m	0.15 m
Transport section	1.02 m	1.07 m
Oxygen charge	10.3 g	33.7 g
Number of Grooves	17	27
Groove width	0.445 mm	0.658 mm
Fin Fip Radius	0.102 mm	0.16 mm
Wetted Perimeter (1 Groove)	2.09 mm	3.25 mm
Total Groove Area	6.07 mm^2	23.2 mm^2

Table 3.2. NHP Design Summary (Rosenfeld *et al.* 1995)

Design Parameter	NHP
Tube material:	Titanium Alloy, Ti-6Al-4V
Tube dimensions:	
Outer diameter	15.0 mm
Wall thickness	1.026 mm
Lengths:	
Evaporator	0.127 m
Condenser	0.178 m
Transport section	0.613 m
Nitrogen charge	24.1 g
Number of metal cables	6
Cable material	Fibrous copper
Cable diameter	3.20 mm
Porosity [3]	0.520 to 0.895 [4]
Permeability $\times 10^{10}$ [3]	0.009 to 12.4 m^2 [4]

     To implement the model for these cases, the $\varepsilon F_{HP,\infty}$ term to be used for the estimation of the parasitic heat load in Eq. (3.1) must be determined. Brennan *et al.* (1993) estimated the parasitic heat load impinging the TRW heat pipe as ranging from 1.1 W to 1.9 W, when the heat pipe was isothermalized around 60 K. The parasitic heat load estimated for the HAC heat pipe was 1.14 W at 119 K. No information regarding parasitic heat loads on the NHP were presented by Rosenfeld *et al.* (1995).

---

[3] Not available in Rosenfeld *et al.* (1995).

[4] Typical values from the literature (Faghri, 1995).

The term $\varepsilon F_{HP,\infty}$ can be estimated by using the relation:

$$q_p = \sigma \varepsilon F_{HP,\infty} A_e (T_\infty^4 - T_{HP}^4) \tag{3.44}$$

where q_p is the parasitic heat load, A_e is the external area of the heat pipes, T_∞ is the surrounding temperature, and T_{HP} is the temperature in which the parasitic heat load were estimated.

The following assumptions are considered for the calculation of the $\varepsilon F_{HP,\infty}$ term:

1. The heat pipes are isothermalized at $T_{HP} = 60$ K for the TRW, = 119 K for the HAC, and = 75 K for the NHP[5];

2. The surrounding temperature T_∞ is constant with time and it is equal to the initial temperature of the heat pipe $T_0 = 280$ K for the TRW, 285 K for the HAC and NHP;

3. The term $\varepsilon F_{HP,\infty}$ is considered to be constant with temperature.

For the TRW heat pipe, the $\varepsilon F_{HP,\infty}$ was obtained for the two extreme parasitic heat loads estimated by Brennan *et al.* (1993). An average value of 1.5 W was also considered. For the HAC heat pipe, the parasitic heat load of 1.14 W was used. Table 3.3 presents the estimated values. An average value of the TRW and HAC parasitic heat load ($q_p = 1.48$ Watt) was used to calculate a $\varepsilon F_{HP,\infty}$ term of 0.114 for the NHP within 285 K and 75 K.

Table 3.3. Estimated values for $\varepsilon F_{HP,\infty}$.

q_p	Heat Pipe	$\varepsilon F_{HP,\infty}$
1.10 Watt	TRW	0.077
1.50 Watt	TRW	0.104
1.90 Watt	TRW	0.134
1.48 Watt	NHP	0.114
1.14 Watt	HAC	0.056

3.4.1 Results for the TRW Heat Pipe

Figure 3.9 shows the comparison between the theoretical model and the experimental flight data for the TRW aluminum/oxygen cryogenic heat pipe start-up. The temperature at the condenser (boundary condition) was obtained by fitting a 3rd order exponential decay function to the experimental data of the cryocooler. The overall agreement between the model

---

[5] The NHP was designed to be isothermalized around 75 K but did not reached an operational steady state according to Rosenfeld *et al.* (1995 – see section Chapter 2, pp. 11).

and the experimental data is good. However, the model underestimates the temperatures at the evaporator end. Some possible reasons for this deviation are listed below:

1. Inadequate estimation of the parasitic heat load. Brennan *et al.* (1993) had not specified whether the parasitic heat load was radiative or (and) conductive;

2. The capillary radius of the liquid column was considered only for the calculation of the capillary driving force on Eq. (3.10), but not considered for the calculation of the mass of liquid. If the curvature of the free surface was taken into account, the area of the liquid would be smaller, and consequently, the mass of the liquid column would decrease.
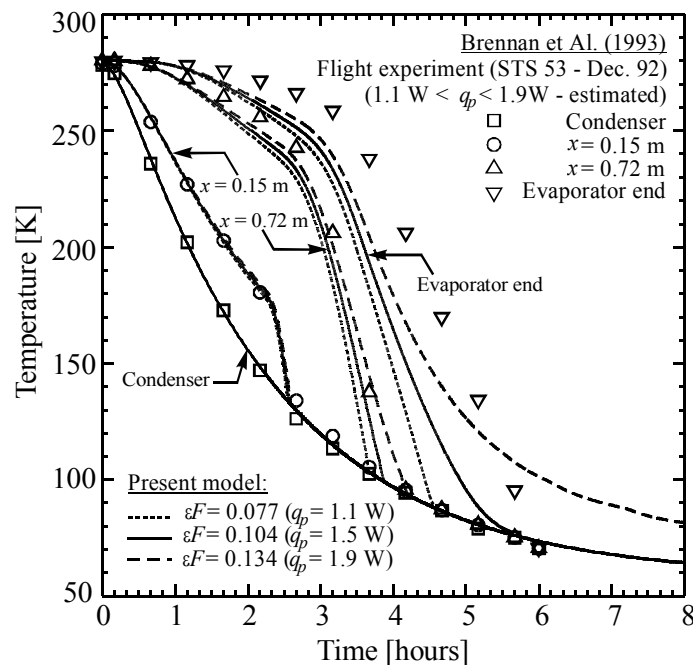

Figure 3.9. Comparison between the theoretical model and the TRW experimental data.

Figure 3.10 shows the pressure-specific volume diagram for the supercritical start-up of the TRW cryogenic heat pipe. The specific volume is shown at the interface between the condenser and transport section ($x = 0$) and for the evaporator end ($x = L$). The circles at the lines represent the thermodynamic state of the heat pipe for each parasitic heat load considered for the calculation. The condensation process will begin at $T_c = 153.6$ K, from the saturated liquid line. It means that for a short period of time (for less than 2 min), the condensed liquid in the condenser region will be in a sub-cooled condition. After the condensation process begins, the quality at the condenser remains closer to zero until the liquid column starts to move towards the evaporator end. This is because more liquid is being condensed as the temperature of the condenser decreases.
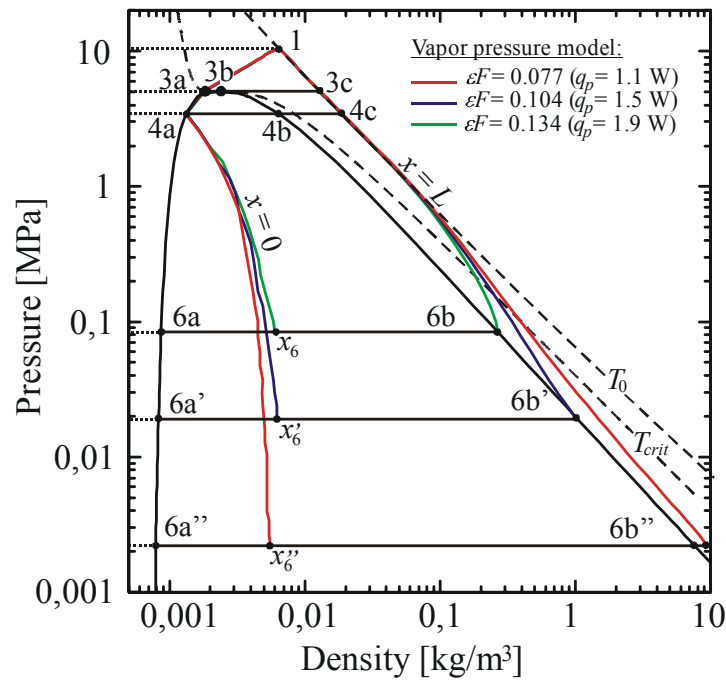
Figure 3.10. Pressure-specific volume diagram (TRW heat pipe).

The liquid fill rate as a function of the temperature of the condenser is shown in Figure 3.11. The liquid fill is defined as the ratio between the condensed liquid mass m_ℓ and the mass that the wick structure can hold m_w:

$$N = \frac{m_\ell}{m_w} = \frac{(1-x)A_c s / v_c}{A_w s / v_\ell} \tag{3.45}$$

where x is the quality of the saturated fluid in the wetted region, A_c is the cross sectional area of the condenser (liquid + vapor), s is the position of the liquid column for a given time, A_w is the cross sectional area of the grooves, and v_c and v_ℓ are the specific volumes of the saturated fluid in the wetted region and saturated liquid, respectively. If $N = 1$, the mass of liquid is enough to fill the grooves with no excess liquid. For $N > 1$ there is excess liquid. It can be observed that there is a large excess of liquid when the start-up process begins. This is because the oxygen enters the saturation zone from a sub-cooled condition. Therefore, the condenser is flooded with saturated liquid. The fill rate starts to decrease as the liquid column advances, and as the liquid specific volume decreases with continued decrease in temperature.

Figure 3.12 shows the position of the liquid column (s) inside the axial grooves as a function of time. Also the position of the liquid slug is shown. This slug was observed by Brennan $et\ al.$ (1993) and it only occurs in microgravity environment. On the ground, the capillary forces cannot support a slug across the vapor region, and excess of liquid is spread as a puddle. This effect facilitated the priming of a heat pipe in ground tests. As shown in
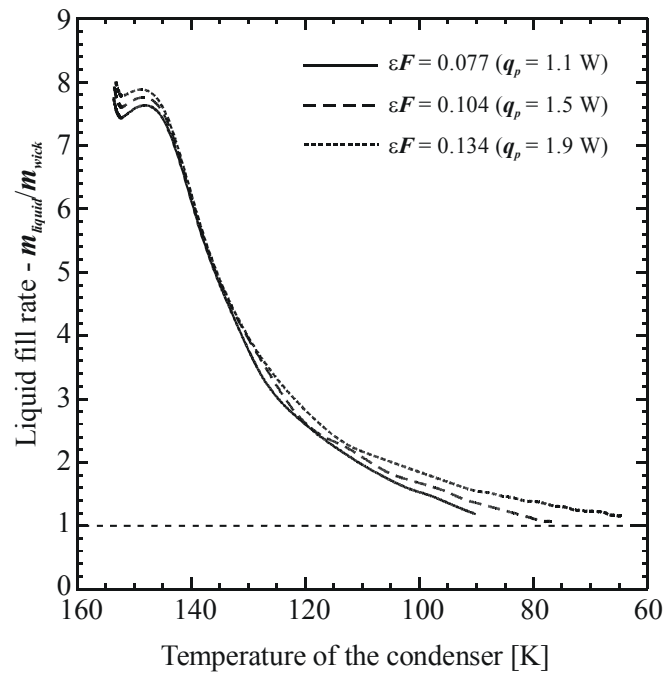
Figure 3.11. Liquid fill rate (TRW heat pipe).

Figure 3.12, when the start-up process begins, the liquid column remains stagnated at the interface between the condenser and the transport region for a few minutes (12.5 min.). This is because the liquid velocity in the liquid column is not sufficient to provide the cooling to the dry region of the heat pipe. As the temperature of the condenser decreases, the surface tension of the working fluid increases, thus, increasing the capillary driving force, causing the liquid velocity to increase. So, the liquid column will eventually advance towards the evaporator end. For a lower parasitic heat load (1.1 W), the start-up process was faster, because less fluid was evaporated from the liquid column. For a higher parasitic heat load (1.9 W), the analytical model shows that the heat pipe would not prime completely, with the liquid column stagnating at about 0.21 m from the evaporator end.

The position of the slug was determined from the data shown in Figure 3.11, for $N > 1$. The position of the liquid slug increases with time until it reaches a maximum at about 0.40 m from the condenser end, and then it decreases. For the lowest parasitic heat load (1.1 W) the position of the slug when the heat pipe primed is at 0.20 m from the condenser end. This because the mass of 10.3 g of oxygen on the TRW heat pipe was designed to fill the wick structure with saturated liquid and no excess at 60 K, but the heat pipe was completely primed at 90 K. The data presented in Figure 3.11 shows that there is an excess of liquid of 1.8 g at 90 K, while the mass of liquid inside the wick structure is 8.1 g. The remaining 0.4 g is the mass of saturated vapor. For the average parasitic heat load of 1.5 W, the heat pipe primed at about 75 K, and the slug was at 0.14 m from the condenser end. It is important to say that if the temperature of the heat pipe continues to decrease until 60 K, there will be no liquid

excess, and therefore, no slug. For the highest parasitic heat load, the liquid slug was stagnated at 0.15 m, as the heat pipe did not primed completely.
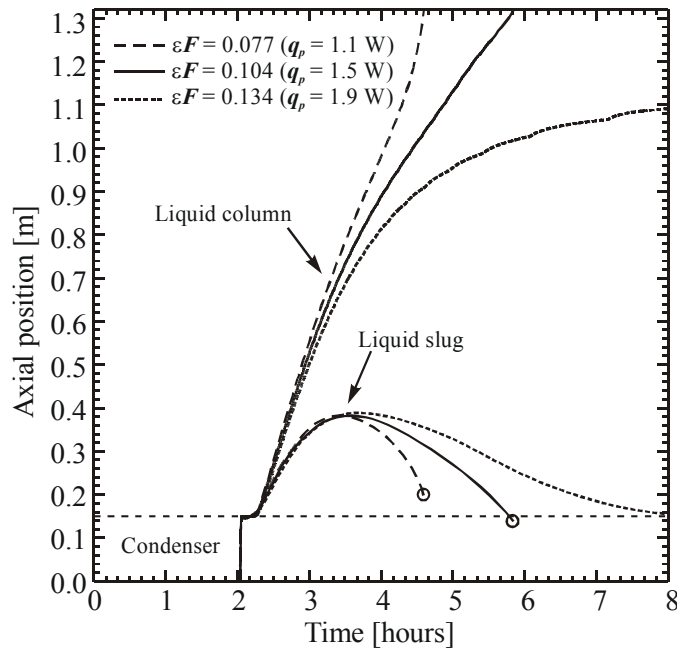

Figure 3.12. Predicted liquid slug and liquid front position (TRW heat pipe).

3.4.2 Results for the HAC Heat Pipe

Figure 3.13 shows the comparison between the theoretical model and the experimental data for the HAC (Hughes Aircraft Co.) aluminum/oxygen cryogenic heat pipe start-up. The temperature at the condenser (boundary condition) was obtained by fitting a 3rd order exponential decay function to the experimental data of the cryocooler. The comparison is considerably good for the heat conduction model (1st stage of the startup process). The condensation of the working fluid started at a temperature far below the oxygen critical temperature (154.6 K), around 128 K. This is because the vapor pressure only drops below the critical pressure when the condenser temperature drops below 128 K. This phenomenon is better observed by analyzing Figure 3.14, which presents a pressure-specific volume diagram for the supercritical startup of the oxygen/aluminum HAC heat pipe.

The supercritical startup process of the HAC heat pipe starts at 285 K, at a pressure around 20 MPa (point 1 in Figure 3.14 – the number of the points in this figure agree with those in Figure 3.3). As the condenser cools down, the vapor pressure decreases. When the condenser cools to a temperature equal to the oxygen critical temperature (T_{crit} = 154.6 K) at point 2a, the pressure of the working fluid inside the heat pipe is still greater than the oxygen critical pressure (P_2 = 8953 kPa > P_{crit} = 5043 kPa). As the condenser continues to cool down, a subcooled liquid slug is formed in the condenser region of the heat pipe. When the pressure
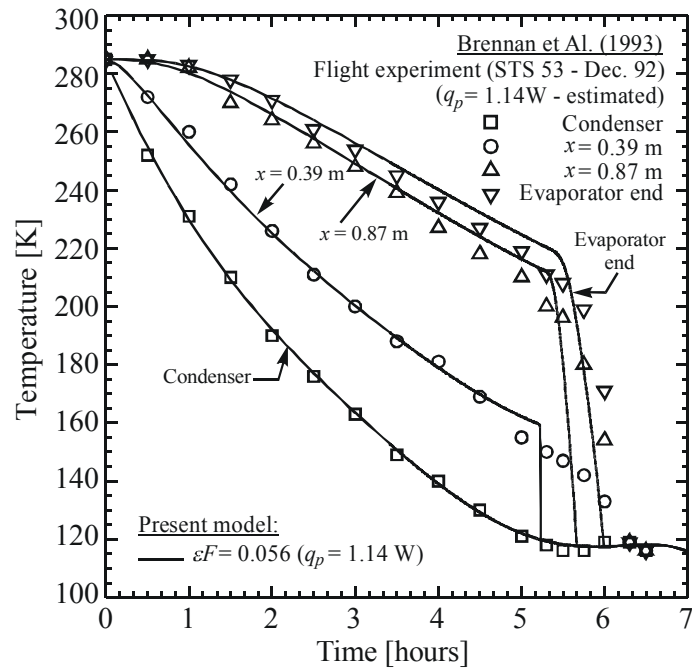
Figure 3.13. Comparison between the theoretical model and the HAC experimental data.
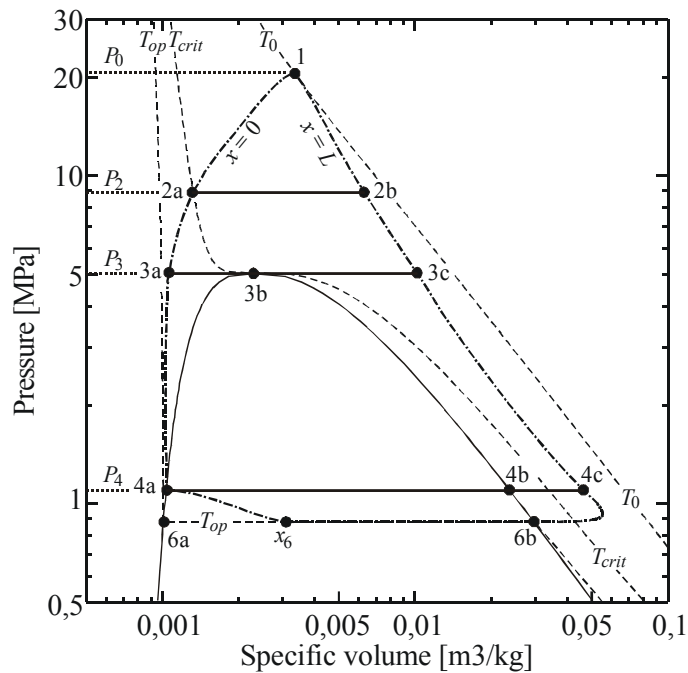

Figure 3.14. Pressure-specific volume diagram (HAC heat pipe).

of the working fluid equals the oxygen critical pressure, the temperature at the condenser end is 128 K (point 3a). At this point in time, the subcooled liquid slug extended for 0.17 m in the adiabatic section of the HAC heat pipe (point 3b). As the startup process continues, the sub-cooled liquid slug recedes until the condenser is completely filled with saturated working fluid at a temperature of 122 K. At this point, the working fluid pressure equals the saturation pressure at 122 K, and the rewetting process starts. The thermodynamic condition of the saturated liquid in the wick structure is given by point 4a and the saturated vapor in the vapor

region, by point 4b. The remaining length of the heat pipe (line 4b – 4c) is at a superheated condition. According to Figure 3.13 the theoretical rewetting process described in section 3.3.3 is faster than the experimental process presented by Brennan *et al.* (1993). This is because at 120 K the capillary force developed at the grooves of the HAC heat pipe are large enough to accelerate the saturated liquid column towards the evaporator end. Figure 3.15 shows a comparison of the driving forces (capillary and frictional) developed at the grooves of the HAC and the TRW heat pipes, obtained from Eqs. (3.11) and (3.12). As the liquid column starts to advance, more vapor is condensed, decreasing the specific volume of the superheated vapor at the evaporator end as shown by the line that connect points 4c and 6b in Figure 3.14. The heat pipe reached an operational steady state at 117.5 K after 6 hours of the beginning of the startup process. Figure 3.16 shows the comparison of theoretical and experimental axial temperature profiles for different times. The overall comparison is good and the trends of the model agree with the physics of the process.
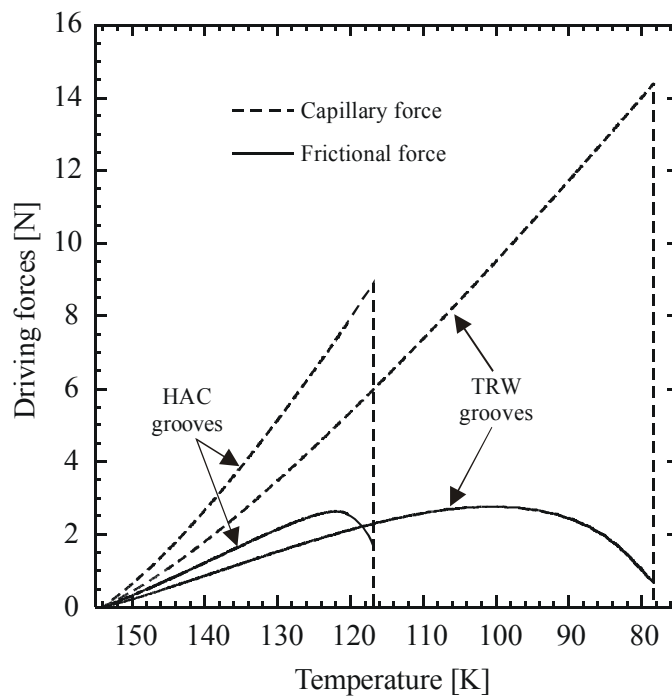

Figure 3.15. Comparison of HAC and TRW driving forces.

The liquid fill rate, obtained from Eq. (3.45), of the HAC heat pipe is shown in Figure 3.17. It can be observed that there is an excess of liquid of almost 350% at the beginning of the condensation process. As the liquid column starts to move, the liquid fill rate decreases, achieving a value next to the unit ($N = 1$) in steady state. From the liquid fill rate data, it is possible to determine the length of the liquid slug observed by Brennan *et al.* (1993). Figure 3.18 shows the liquid slug and liquid column position as a function of the startup time.
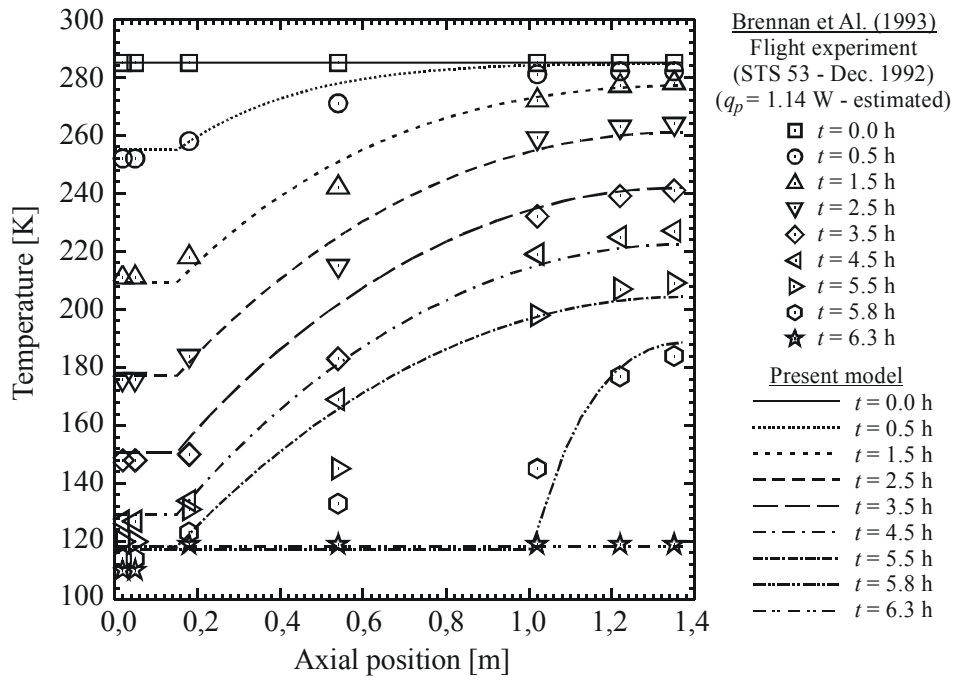
Figure 3.16. Temperature vs. axial position at different times (HAC heat pipe).
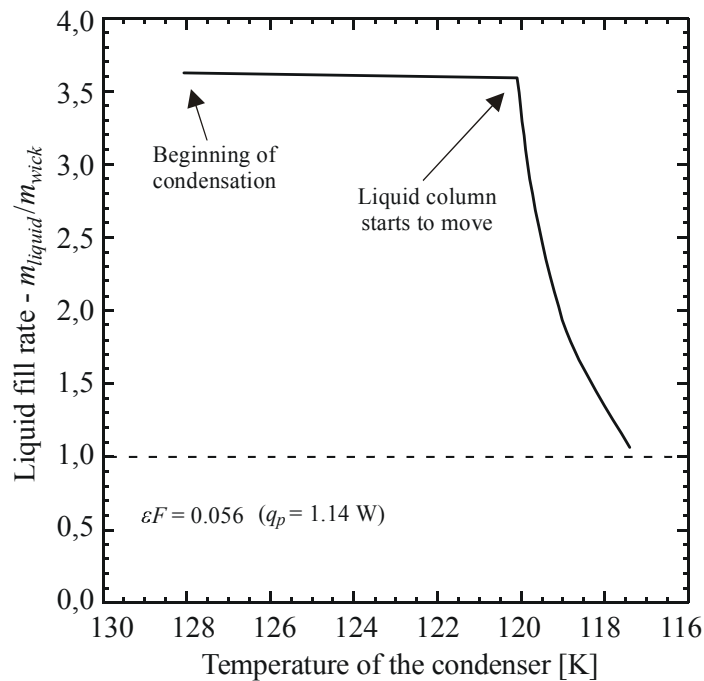
Figure 3.17. Liquid fill rate (HAC heat pipe).

3.4.3 Results for the NHP Heat Pipe

The titanium/nitrogen heat pipe (NHP) tested by Rosenfeld *et al.* (1995) did not reached an operational steady state, with just 32% of the total heat pipe length cooling below the critical temperature of nitrogen (126.2 K). Although little information regarding the parasitic heat load and the wick structure of this heat pipe is available at Rosenfeld *et al.* (1995),

Figure 3.18. Predicted liquid slug and liquid front position (HAC heat pipe).
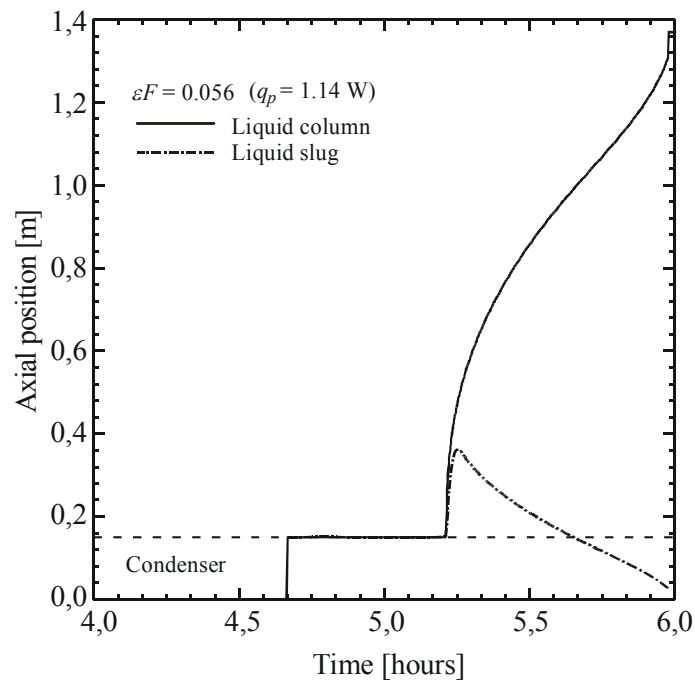
the experimental data for this unsuccessful startup can be used for comparison with the presented model, and some conclusions can be drawn regarding the titanium/nitrogen heat pipe. The wick structure of the NHP was composed by six porous copper cables with a circular section of 3.2 mm of diameter held against the internal diameter of the titanium alloy (Ti-6 Al-4V ELI) pipe by a full-length centered spring. No values for the porosity and permeability were presented by the authors, but typical values can be found in the literature (Faghri, 1995): $0.520 \leq \varphi \leq 0.895$ (porosity); $0.009 \text{ m}^2 \leq K \leq 12.4 \text{ m}^2 \ (\times 10^{-10})$. According to Eq. (3.34) which gives an average velocity of the saturated liquid in a porous wick structure, the combination of φ and K that produces the largest velocity are $\varphi = 0.895$ and $K = 12.4 \times 10^{-10} \text{ m}^2$. Also, the largest porosity provides more void volume in the wick structure to be filled with liquid, and therefore, it provides a lower vapor pressure during startup if compared to a lower porosity. So, two theoretical cases were considered for comparison with the experimental data - **case 1**: $\varphi = 0.895$ and $K = 12.4 \times 10^{-10} \text{ m}^2$; and **case 2:** $\varphi = 0.520$ and $K = 0.009 \times 10^{-10} \text{ m}^2$.

Figure 3.19 present the comparison between the experimental data of Rosenfeld *et al.* (1995) and the theoretical model. The temperature at the condenser (boundary condition) was obtained by fitting a 3rd order exponential decay function to the experimental data of the cryocooler. The comparison is good and the model predicted the unsuccessful startup of the titanium/nitrogen heat pipe. This failure is due to the fact that the vapor pressure never reached the critical pressure of the nitrogen in none of the cases, even though the temperature of the condenser was far below the critical temperature of the nitrogen even after 8 hours of

testing. The pressure-specific volume diagram for the NHP is shown in Figure 3.20 for both cases. It can be observed that, for the largest porosity (case 1), the vapor pressure at steady state reached 6.1 MPa while for the lower porosity the pressure at steady state was 13.3 MPa (more than twice larger!). However, in both cases, the steady state pressure was still higher than the critical pressure of the nitrogen (3.4 MPa), and therefore, no condensation of the working fluid occurred during the startup because a saturation thermodynamic condition was never reached in the titanium/nitrogen heat pipe. The shaded zone in Figure 3.20 represent any steady state possible for the combination of porosity and permeability within the typical ranges for porous metal wick structures.
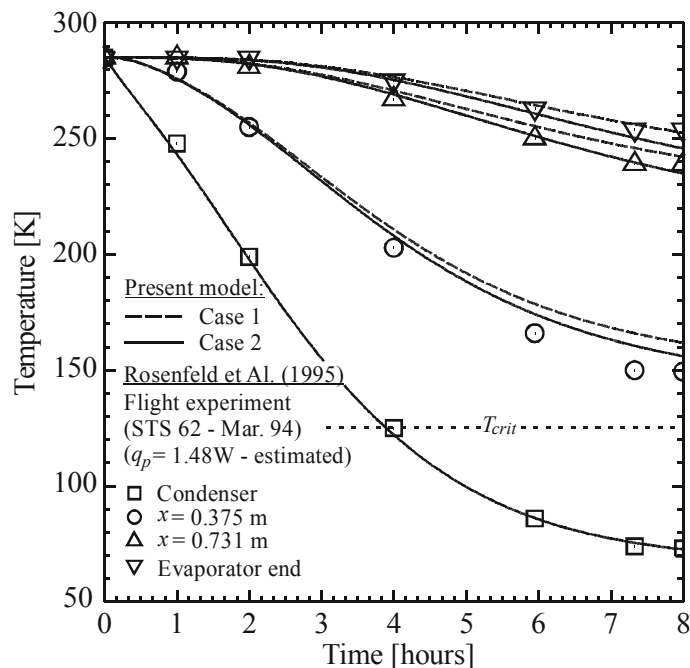

Figure 3.19. Comparison between the theoretical model and the NHP experimental data.

Figure 3.21 shows the comparison between the theoretical axial temperature profile for case 1 and the experimental data presented by Rosenfeld *et al.* (1995). Some overestimation of temperatures are observed, and this can be due to little information about the thermophysical properties of the titanium alloy used in the NHP. Typical values for pure titanium were used for the calculations. Nevertheless, the overall comparison is good.

Concluding, the non-operational steady state reached by the titanium/nitrogen heat pipe was due to a combination of the effects of the parasitic heat loads, low conductance of the titanium wall, and mass of working fluid. The designed working fluid mass of 24.1g provided a high initial pressure, and the low conductance of the heat pipe wall, added to the parasitic heat load, did not provided enough cooling for the vapor pressure to decrease below the critical pressure of the nitrogen.
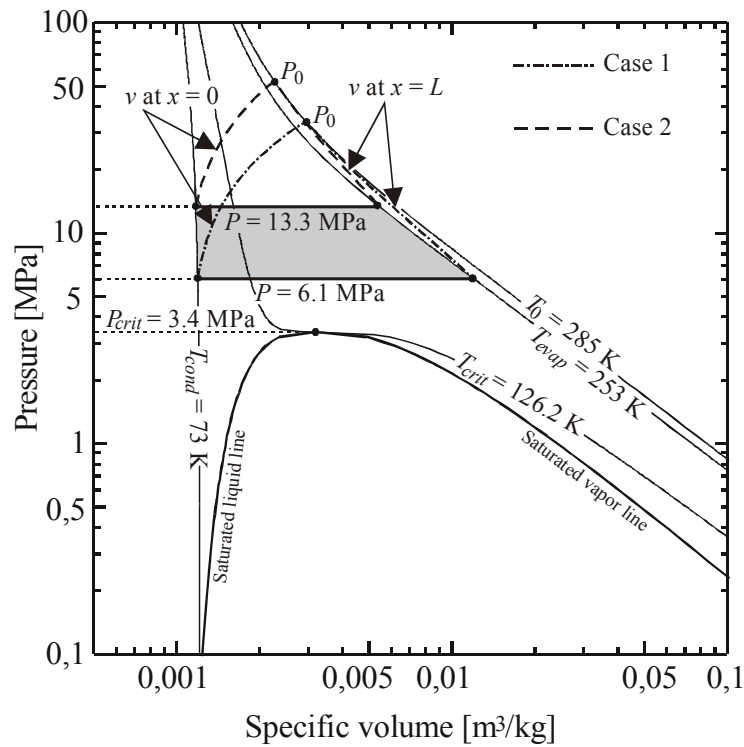
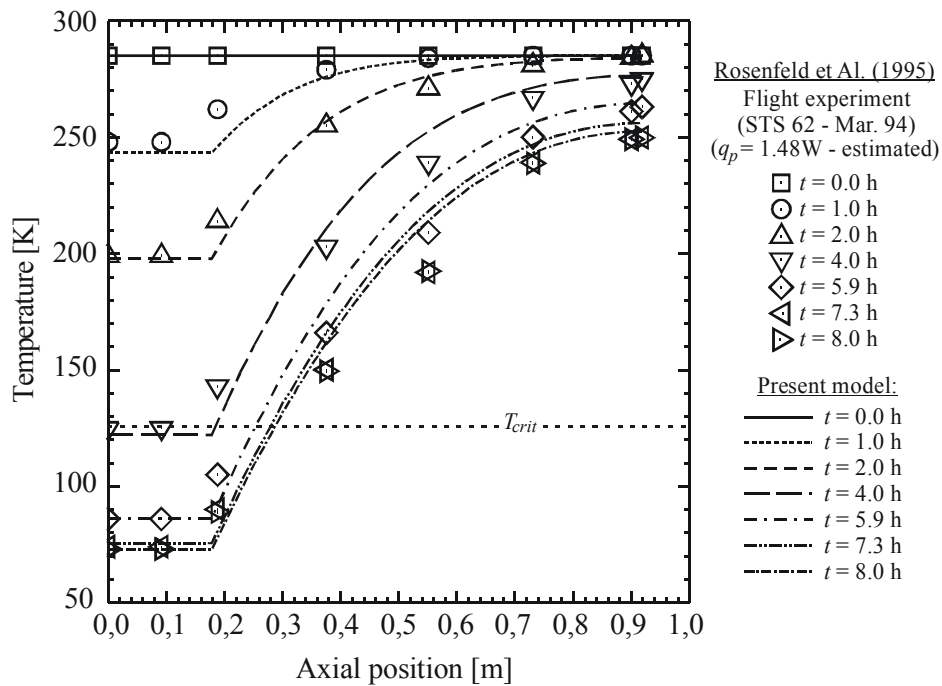Figure 3.20. Pressure-specific volume diagram (NHP heat pipe).

Figure 3.21. Temperature vs. axial position at different times (NHP heat pipe – case 1).

3.5 Summary and Conclusions

A theoretical analysis of the supercritical startup of cryogenic heat pipes was performed in this chapter. It was shown that the working fluid inside the heat pipe can reach a

subcooled thermodynamic state before condensation begins, depending on the initial thermo-dynamic state, defined by the working fluid mass and the initial temperature of the heat pipe.

A new model for the supercritical startup of cryogenic heat pipes was presented. The one-dimensional model included new features such as the vapor pressure of the working fluid, which is used as a criterion for the beginning of the condensation process. The vapor pressure model accounts for the thermodynamic properties of the working fluid, which were determined by the use of a fundamental equation of state based on the free Helmholtz energy (Jacobsen *et al.* 1997). The saturated liquid column formed in the condenser region was modeled by a momentum balance. The effect of parasitic heat loads over the heat pipe external wall was included in the liquid column model. These features contributed for a better insight of the supercritical startup of cryogenic heat pipes.

The theoretical model was compared with three sets of flight (microgravity) experimental data available in the literature. According to the assumptions made to estimate the parasitic heat loads and other geometrical parameters, the model was in good agreement with the experimental data for microgravity.

A theoretical analysis of the supercritical startup limitations of a cryogenic heat pipe with parasitic heat loads was presented by Couto et al. (2002) and the results are reproduced in Appendix D. This analysis was based on the TRW heat pipe geometry, for different levels of parasitic heat loads, different external diameters, and different wick geometries.

3.6 Synopsis

Uma análise teórica da partida supercrítica de tubos de calor criogênicos foi efetuada neste capítulo. A análise mostrou que o fluido de trabalho dentro do tubo de calor pode atingir um estado termodinâmico de sub-resfriamento antes da condensação começar, dependendo do estado termodinâmico inicial, definido pela massa do fluido de trabalho e pela temperatura inicial do tubo de calor.

Um novo modelo para a partida supercrítica de tubos de calor criogênicos foi apresentado. O modelo unidimensional leva em consideração a pressão de vapor do fluido de trabalho, a qual é usada como um critério para determinar o início do processo de condensação. A modelagem da pressão de vapor considera as propriedades termodinâmicas do fluido de trabalho como função da temperatura, que são determinadas através do uso de uma equação fundamental de estado baseado na energia livre de Helmholtz (Jacobsen et al. 1997). A coluna de líquido saturado, formada na região do condensador foi modelada através de um balanço da quantidade de movimento. O efeito de cargas de térmicas parasitas

na parede externa do tubo de calor foi incluído na modelagem da coluna de líquido. Foi mostrado que as cargas térmicas parasitas evaporam líquido ao longo do comprimento da coluna de líquido saturado, reduzindo sua quantidade de movimento.

O modelo teórico foi comparado com três conjuntos de dados experimentais obtidos em condições de microgravidade, disponíveis na literatura. De acordo com as hipóteses consideradas para o cálculo das cargas térmicas parasitas e outros parâmetros geométricos, o modelo apresentou boa concordância com os dados experimentais para microgravidade, e a comparação proveu uma boa compreensão do fenômeno da partida supercrítica de tubos de calor criogênicos.

<div align="right">

Chapter 4
Experimental Analysis

</div>

4.1 Introduction

The experimental analysis of the supercritical startup of a nitrogen/stainless steel heat pipe is presented in this section. The experimental analysis consists of designing, manufacturing, assembling, charging and testing the cryogenic heat pipe during a supercritical startup process in a vacuum chamber. The experiments were carried out at the LABSOLAR/NCTS – EMC/UFSC – Brazil, during the year of 2002. The experimental data is compared with the theoretical model presented in Chapter 4. Based on the comparison, a pressure-specific volume diagram for some experiments is presented to provide more information regarding the supercritical startup process. The experimental results and comparisons are summarized in a conclusion at the end of this chapter.

4.2 Heat Pipe Design Analysis

Candidate working fluids for a cryogenic heat pipe are oxygen, nitrogen, methane and ethane, among others. Figure 4.1 shows the liquid transport factor N_l for these working fluids, given by (Joy, 1970 and Chi and Cygnarowicz, 1970):

$$N_\ell = \sigma h_{fg} \sqrt{\frac{\rho_\ell \rho_v}{\mu_\ell \mu_v}} \tag{4.1}$$

where σ is the liquid surface tension, h_{fg} is the latent heat of vaporization, ρ_ℓ and ρ_v are the liquid and vapor densities, and μ_ℓ and μ_v are the liquid and vapor viscosities. Data for ammonia and water are also presented for comparison purposes. Argon was not considered because of its high triple point temperature (84 K). Neon, hydrogen and helium were not considered because their critical temperatures are very low (44 K, 33 K and 5 K respectively). From this

figure, it is clear that ethane exhibits the lowest liquid transport factor below 170 K. Below 150 K, methane seems to have the largest liquid transport factor. However, nitrogen will be considered for the design analysis because of its availability and safety[6]. Therefore, for the experimental analysis, a **metal screen wick nitrogen/stainless steel heat pipe** is considered. Stainless steel was selected because of its availability, compatibility with nitrogen, and compatibility with the stainless steel metal screen already available at the laboratory.
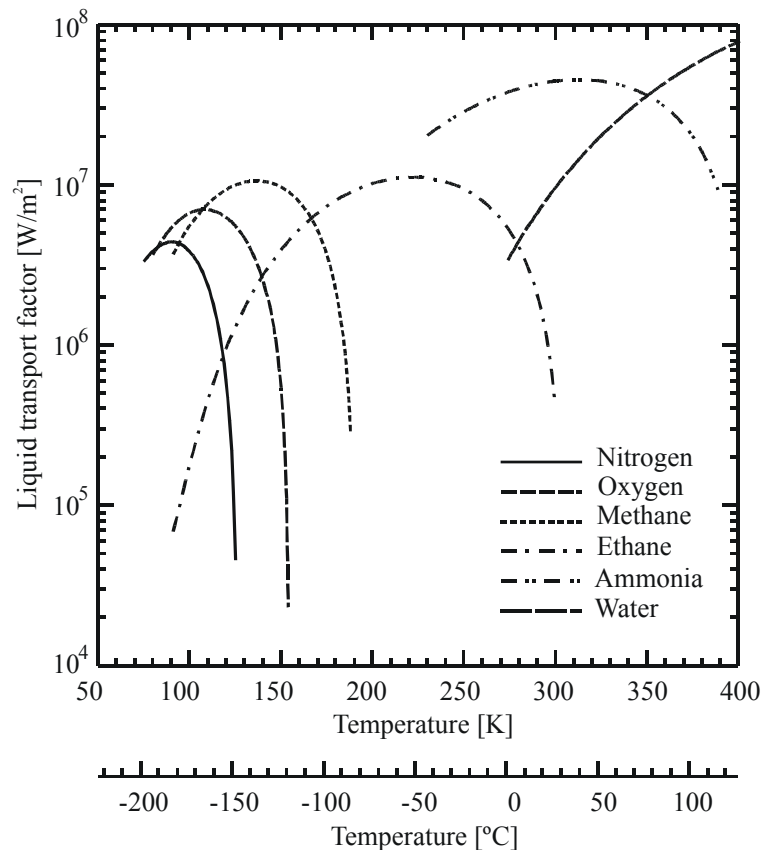

Figure 4.1. Liquid transport capacity for selected cryogenic working fluids.

The cryogenic heat pipe design consists of determining the steady state characteristics (heat transport capacity and heat transfer limitations) as a function of the operating temperature. The objective is to determine the best configuration (diameter, number of screen layers and Mesh number) for a cryogenic heat pipe operating with maximum heat transport capacity.

---

[6] The principal hazards in the handling of cryogenic fluids are those associated with the response of the human body and the surroundings to these fluids and their vapors, and those associated with reactions between these fluids and the surroundings. Nitrogen is colorless, odorless, inert, and looks non-noxious, but the leakage of nitrogen containers decreases the oxygen content of the atmosphere. Oxygen gas, in the other hand, produces exhilarating effects when breathed, and lung damage can occur when oxygen concentration in air exceeds 60%. Prolonged exposure to an atmosphere of pure oxygen may cause bronchitis, pneumonia or lung collapse. However, the greatest threat of highly concentrated oxygen lies in the increased flammability and explosiveness of the materials immersed in oxygen-rich atmospheres (Timmerhaus and Flynn, 1978).

4.2.1 Heat Transport Analysis

The proper operation of a heat pipe requires the net capillary difference between the wet and dry points[7] to be greater than the summation of all the pressure losses occurring throughout the liquid and vapor paths (Peterson, 1991). The pressure losses are due to inertial and viscous effects occurring in the vapor and liquid phases, phase transition effects occurring in the evaporator and condenser sections, and axial hydrostatic effects due to gravitational effects. Therefore, the fluid-flow pressure drop equation for a heat pipe operating at a maximum heat input in the presence of gravity can be written as follows:

$$\Delta P_{c,max} \geq \Delta P_v + \Delta P_\ell + \Delta P_{ph,e} + \Delta P_{ph,c} + \Delta P_{hyd|} \tag{4.2}$$

where $\Delta P_{c,max}$ is the maximum capillary pressure developed at the wick structure, ΔP_v is the vapor pressure drop, ΔP_ℓ is the liquid pressure drop, $\Delta P_{ph,e}$ and $\Delta P_{ph,c}$ are the pressure drops due to phase change at the evaporator and condenser, respectively, and ΔP_{hyd} is the pressure drop due to body forces

Neglecting the effects of phase change in the evaporator and condenser sections, Eq. (4.2) can be rewritten, according to Peterson (1991) in the following form:

$$\frac{2\sigma}{r_{eff}} \geq \frac{(f\,\text{Re}_v)\mu_v}{2\pi R_v^4 \rho_v h_{fg}} Q_e L_{eff} + \frac{\mu_\ell}{K\pi(R_w^2 - R_v^2)\rho_\ell h_{fg}} Q_e L_{eff} + \rho_\ell g L_{tot} sin\phi \tag{4.3}$$

where r_{eff} is the effective capillary radius, f is the friction factor, Re_v is the axial Reynolds number for the vapor phase, R_v is the vapor radius, R_w is the wick radius (or internal radius of the heat pipe container), Q_e is the heat load, K is the permeability of the wick structure, L_{eff} is the effective length of the heat pipe, L_{tot} is the total length of the heat pipe, g is the gravitational acceleration, and ϕ is the tilt angle of the heat pipe with respect to horizontal. Assuming that the wet point is at the interface of the condenser and adiabatic section (Peterson, 1991) and that the vapor flow is laminar and incompressible in a circular heat pipe (Faghri, 1995), Eq. (4.3) can be written in terms of the maximum heat load $(QL)_{max}$:

$$(QL)_{max} = \frac{2\sigma/r_{eff} - \rho_\ell g L_t \,sen\,\phi}{F_\ell + F_v} \tag{4.4}$$

---

[7] Wet point: point at which the vapor and liquid pressures are approximately equal or, the meniscus radius of curvature is at a maximum. Dry point: the point at which the meniscus has a minimum radius of curvature.

where F_ℓ and F_v are the liquid and vapor friction factors:

$$F_v = \frac{(f\,\mathrm{Re}_v)\mu_v}{2R_v^2 A_v \rho_v h_{fg}}\;;\quad F_\ell = \frac{(f\,\mathrm{Re}_{\ell,h})\mu_\ell}{2R_{\ell,h}^2 A_\ell \rho_\ell h_{fg}} = \frac{\mu_\ell}{KA_\ell \rho_\ell h_{fg}} \tag{4.5}$$

Equation (4.4) is a function of the thermophysical properties of the working fluid and of the geometrical parameters of the heat pipe. Using the expressions derived by Faghri (1995) for the effective capillary radius and for the porosity for screen wick heat pipes (presented in Table 4.1), it is possible to obtain graphically the variation of the maximum heat transport factor with respect to the geometric parameters for different wick structures.

Table 4.1. Expressions for the effective capillary radius and permeability [8].

Wick structure	Effective capillary radius - r_{eff}	Permeability[9] - K	Hydraulic diameter - D_h	Porosity - φ
Multiple wire mesh screen	$\dfrac{W+D}{2}$	$\dfrac{D^2\varphi^3}{122(1-\varphi)^2}$	$\dfrac{D\varphi}{1-\varphi}$	$1-\dfrac{n_w\delta_1(1-\varphi_1)}{\delta_w}$

The heat transport factor defined as the left hand side of Eq. (4.4) as a function of temperature for different metal screen wick geometries is shown in Figure 4.2. Wick structures composed of stainless steel screen Mesh 160 (graph A) and Mesh 254 (graph B) are considered, and the geometric parameters for these screens are shown in Table 4.2. This figure shows data for heat pipes made of tubes with three different external diameters: 3/4" (19.05 mm), 1/2" (12,7 mm) and 3/8" (9.53 mm) and wall thickness of 1.3 mm (these dimensions are usually found in commercial stainless steel, aluminum and copper tubes). The thickness of one layer and n layers of metal screen were experimentally measured using a calibrated 0-25 µm micrometer. Porosity was obtained from the expression presented by Imura *et al.* (1988) and is shown in Table 4.1.

---

[8] W = wire spacing, D = wire diameter, N = mesh number, n_w = number of metal screen layers, δ_1 = thickness of one layer, δ_w = thickness of n_w layers, φ_1 = porosity of one layer.

[9] Carman-Kotemy expression.

Table 4.2. Metal screen wick geometry.

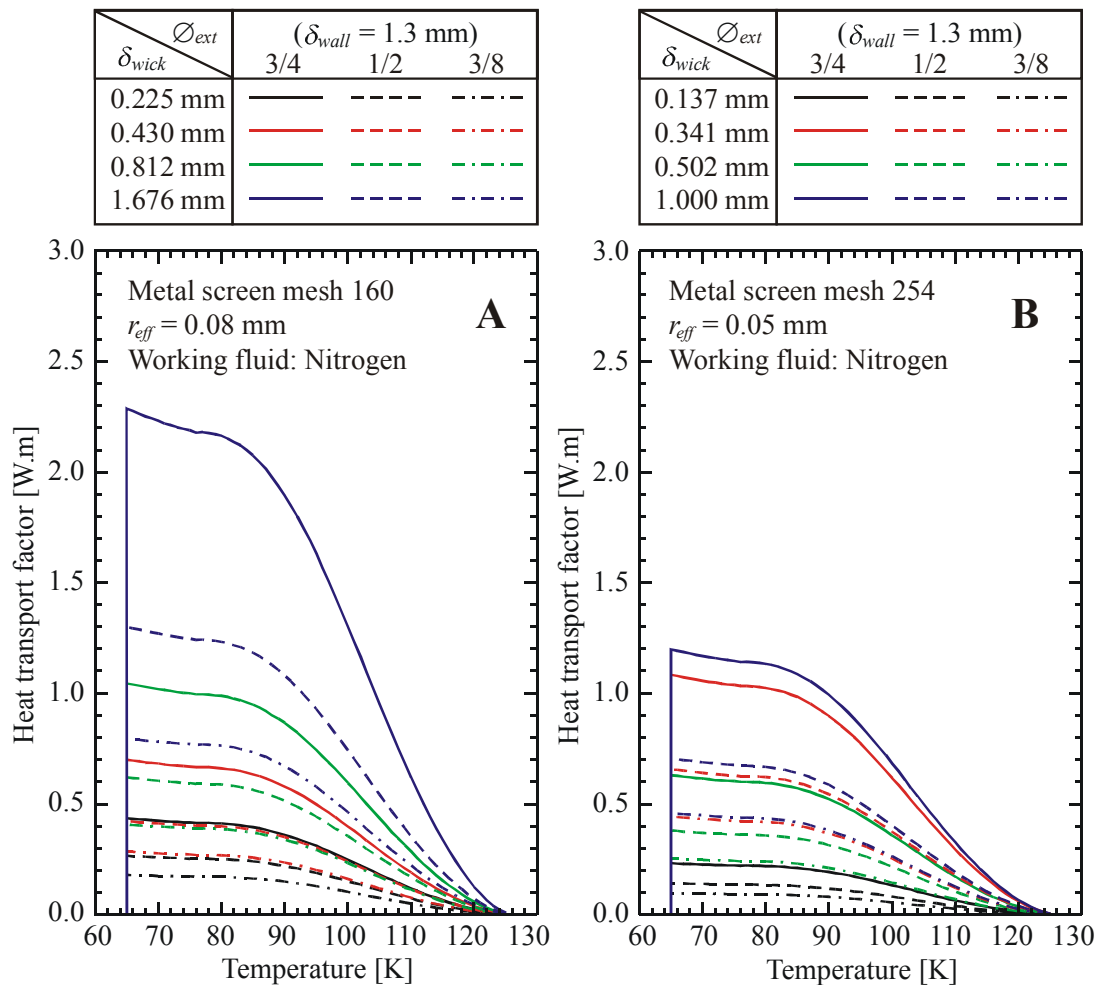| Mesh	No. of Layers	Material	Wire spacing	Wire diameter	Thickness	Porosity	Permeability	Effective capillary radius
160	1	AISI 316 Stainless steel	0.090 mm	0.070 mm	0.225 mm	0.671	2.67×10^{-10} m^2	0.08 mm
	2				0.430 mm	0.656	2.27×10^{-10} m^2	
	4				0.812 mm	0.635	1.84×10^{-10} m^2	
	8				1.676 mm	0.647	2.07×10^{-10} m^2	
254	1	AISI 304 Stainless steel	0.060 mm	0.040 mm	0.137 mm	0.734	1.18×10^{-10} m^2	0.05 mm
	2				0.341 mm	0.786	2.24×10^{-10} m^2	
	4				0.502 mm	0.710	0.89×10^{-10} m^2	
	8				1.000 mm	0.708	0.88×10^{-10} m^2	

Figure 4.2. Heat transport factor for different metal screen wick geometry.

From Figure 4.2 it can be inferred that a heat pipe with a larger external diameter, $\varnothing_{ext}$, will provide a higher heat transport factor for a given wick structure thickness, δ_w. This is because a larger diameter provides a larger vapor space, decreasing the vapor friction factor. Although the capillary pressure provided by the screen Mesh 254 is larger than that provided by the screen Mesh 160, the later presented better results for the heat transfer factor because of its larger permeability, which decreases the liquid friction [see Eq. (4.5)]. The capillary

pressure provided by screen Meshes 160 and 254 is shown in Figure 4.3. The liquid friction factor is shown in Figure 4.4. It was also observed that, for screen Mesh 254, a wick structure composed of 2 layers presents better results for the heat transport factor than a wick composed of 4 layers. This is due to the combination of the permeability, K, and the wick cross sectional area, A_w. Even if the structure with 4 layers has a larger cross sectional area (which would create a larger wick shear stress), the product KA_w is larger for the 2 layers wick structure.
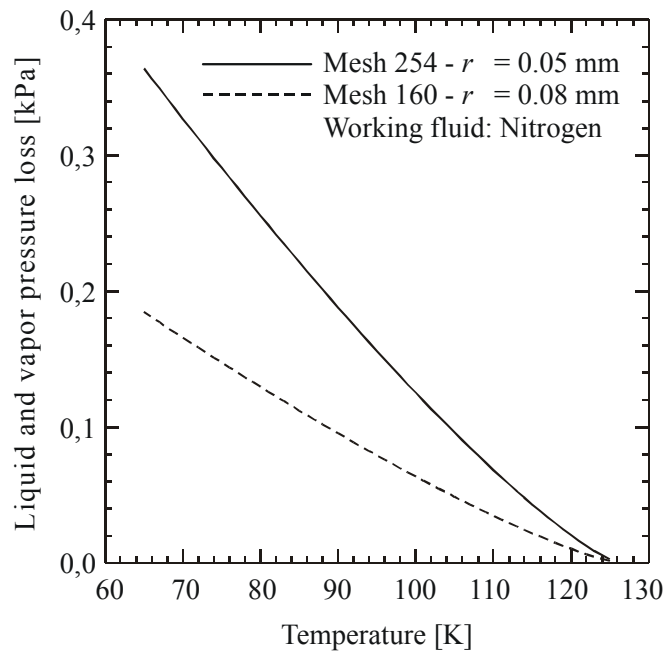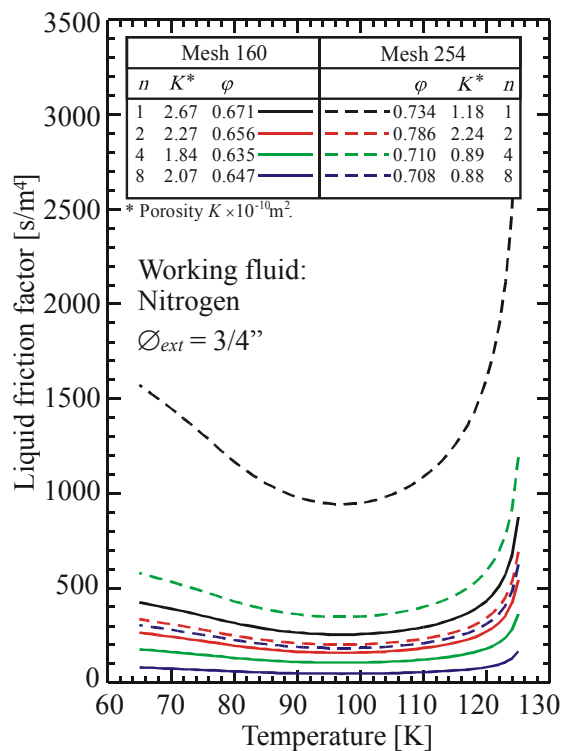

Figure 4.3. Capillary pressure.

Figure 4.4. Liquid friction factor (tube: $\varnothing_{ext} = 3/4$”).

4.2.2 Steady State Performance Analysis

Cryogenic working fluids present small values of thermal conductivity (see Figure 1.3) and transport factor (see Figure 4.2). Therefore, cryogenic heat pipes usually have small heat transport capability, which can cause large axial temperature drop along depending on the heat load transported.

For modeling the steady state performance of a cryogenic heat pipe, the network thermal model proposed by Faghri (1995) is used. In this model, the heat pipe is divided into nine components each one with a specific thermal resistance. The temperature at eight locations is calculated based on these resistances. This model provides a simple way to calculate temperatures and heat fluxes in the heat pipe under steady state conditions. A schematic of the network thermal model is shown in Figure 4.5.
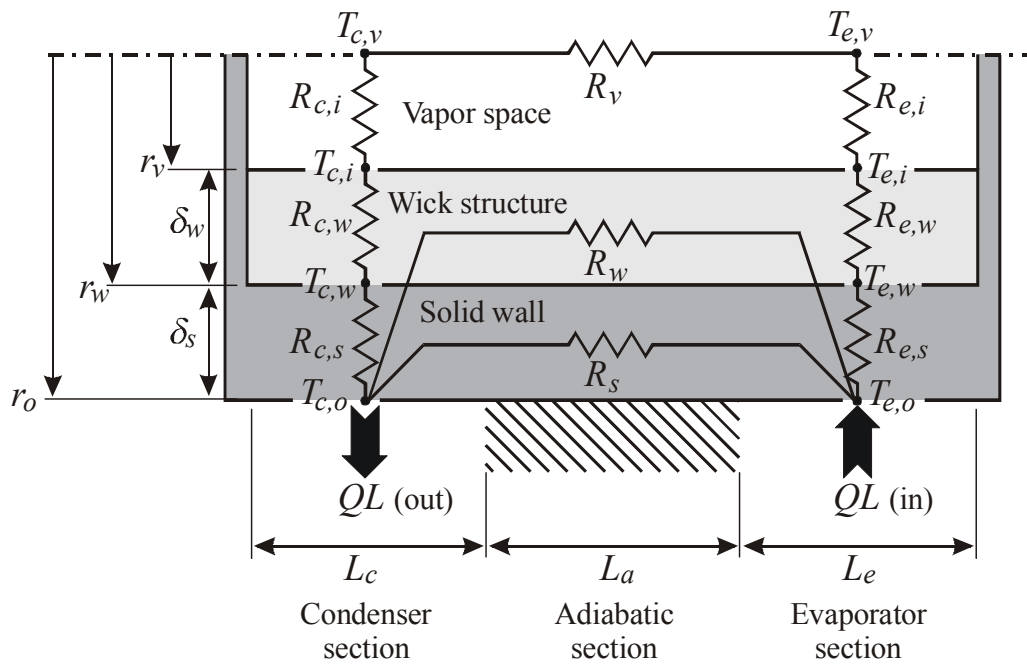

Figure 4.5. Network thermal model (Faghri, 1995).

At steady state, the entire heat load imposed at the evaporator (Q_e) must be transported to and rejected at the condenser. The temperature in each component of the heat pipe can be determined from the Fourier law:

$$Q_e = -kA_{\perp} \frac{dT}{dn} \tag{4.6}$$

where $A_\perp$ is the heat conduction cross sectional area. According to Peterson (1991), the axial heat conduction within the wick structure and solid wall is negligible in steady state, when compared to the other branches to the circuit. On the other hand, the interfacial resistances can also be neglected (condensation and evaporation resistances).

In Eq. (4.2) it is stated that the vapor pressure drop is always smaller than the capillary pressure. For simplicity, let's assume that the vapor pressure is equal to the capillary pressure:

$$\Delta p_v = \Delta p_c = \frac{2\sigma}{r_{eff}} \tag{4.7}$$

The corresponding vapor temperature drop can be obtained by substituting Eq. (4.7) into the Clausius-Clapeyron equation (Van Wylen and Sonntag, 1973). The result is given by:

$$\Delta T_v = \frac{RT_v^2}{P_v h_{fg}} \frac{2\sigma}{r_{eff}} \tag{4.8}$$

The magnitude of ΔT_v for cryogenic working fluids is usually small because of the small values of T_v and σ and large values of P_v and h_{fg}. For example: for saturated nitrogen at atmospheric pressure with r_{eff} being 50µm, ΔT_v is only 0.03 K, being negligible for most applications. Therefore, the thermal network showed in Figure 4.5 is resumed to four resistances in series, as shown in Figure 4.6.

For the solid wall at the evaporator section, Eq. (4.6) can be solved by direct integration in the radial direction assuming that $T = T_{e,o}$ at $r = r_o$ and $T = T_{e,w}$ at $r = r_w$:

$$T_{e,o} - T_{e,w} = \frac{Q_e}{2\pi k_s L_e} \ln\left(\frac{r_o}{r_w}\right) \tag{4.9}$$

Similarly, for the wick structure at the evaporator section, Eq. (4.6) can be solved by direct integration assuming that $T = T_{e,w}$ at $r = r_w$ and $T = T_v$ at $r = r_v$, resulting in:

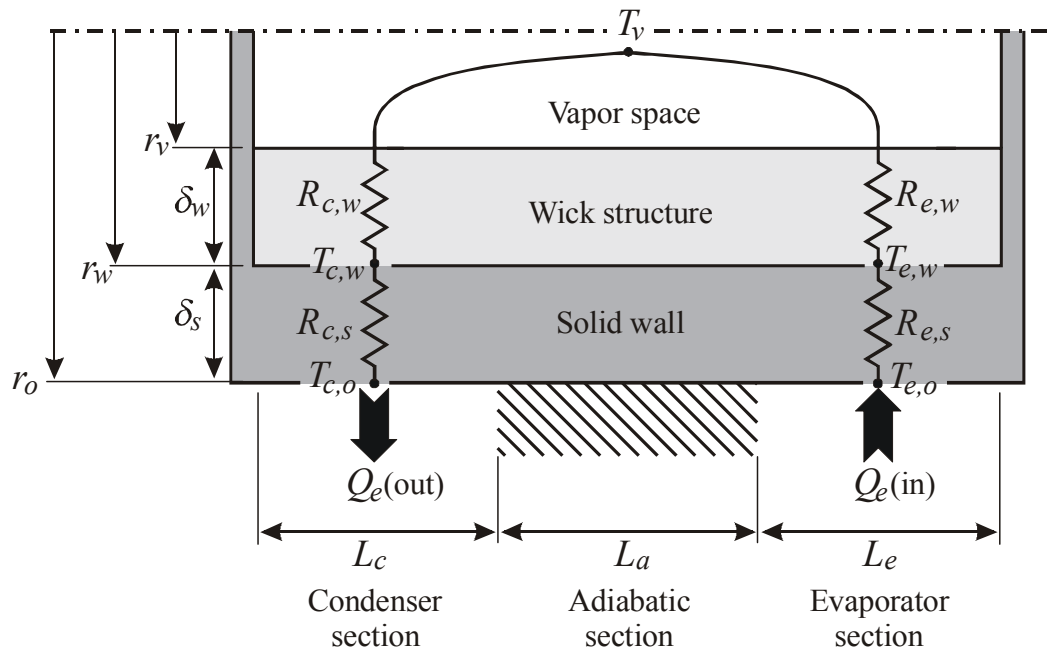$$T_{e,w} - T_v = \frac{Q_e}{2\pi k_{eff} L_e} \ln\left(\frac{r_w}{r_v}\right) \tag{4.10}$$

Figure 4.6. Simplified network thermal model.

For the wick structure at the condenser section, Eq. (4.6) can be solved by direct integration assuming that $T = T_{c,w}$ at $r = r_w$ and $T = T_v$ at $r = r_v$:

$$T_v - T_{c,w} = \frac{Q_e}{2\pi k_{eff} L_c} \ln\left(\frac{r_w}{r_v}\right) \tag{4.11}$$

Again, for the solid wall at the condenser section, Eq. (4.6) can be integrated assuming that $T = T_{c,o}$ at $r = r_o$ and $T = T_{c,w}$ at $r = r_w$, resulting in:

$$T_{c,w} - T_{c,o} = \frac{Q_e}{2\pi k_s L_c} \ln\left(\frac{r_o}{r_w}\right) \tag{4.12}$$

The effective conductivity in Eqs. (4.10) and (4.11), for a screen wick structure, is given by the following expression (presented by Faghri, 1995, and derived by Rayleigh, 1892):

$$k_{eff} = \frac{k_\ell[(k_\ell + k_s) - (1 - \varphi)(k_\ell - k_s)]}{(k_\ell + k_s) + (1 - \varphi)(k_\ell - k_s)} \tag{4.13}$$

This expression can be rewritten in a non-dimensional form as follows:

$$\frac{k_{eff}}{k_\ell} = \frac{1 - (1-\varphi)K_{\ell,s}}{1 + (1-\varphi)K_{\ell,s}} \tag{4.14}$$

where $K_{\ell,s}$ is a non-dimensional relation between the conductivity of the wick material and the liquid in the wick structure, given by:

$$K_{\ell,s} = \frac{k_s - k_\ell}{k_s + k_\ell} = \frac{1 - k_\ell/k_s}{1 + k_\ell/k_s} \tag{4.15}$$

Generally, for cryogenic working fluids and for materials used in cryogenic heat pipes, the order of magnitude of the k_ℓ/k_s ratio ranges from 10^{-5} to 10^{-3}, which in turn produces a $K_{\ell,s}$ parameter on the order of 10^0. For nitrogen and stainless steel, the $K_{\ell,s}$ parameter ranges from 0.9992 (at 65 K) to 0.9999 (at 126 K), while for oxygen and aluminum, it ranges from 0.9908 (at 65 K) to 0.9991 (at 154 K). Therefore, the effective conductivity (Eq. 4.13) is a function mainly of the geometry of the wick structure (porosity φ) and of the liquid conductivity (k_ℓ), as it can be observed in Figure 4.7. The non-dimensional effective conductivity k_{eff}/k_ℓ is very sensitive to the porosity variation. In the other hand, the non-dimensional effective conductivity does not vary much with the $K_{\ell,s}$ parameter, being negligible for large porosities ($\varphi >$ 0.8). Also, the magnitude of the effective conductivity (k_{eff}) approaches the magnitude of the liquid conductivity ($k_{eff}/k_\ell \rightarrow 1$) as the porosity tends to one. This is because the porosity is defined as the ratio of the pore volume to the total volume of the wick structure. Therefore, a large porosity implies in a wick structure where the total volume of the wick approaches the liquid volume. Nitrogen and stainless steel at 65 K are taken as an example: the conductivity of the saturated liquid nitrogen is 0.156 W/mK and the conductivity of the stainless steel is 403 W/mK. For a porosity of 0.6 the effective thermal conductivity, k_{eff}, is 0.364 W/mK, while for a porosity of 0.95, it is 0.173 W/mK.

Equations (4.9) through (4.12) allows the calculation of the heat pipe temperature drop ($\Delta T = T_{e,o} - T_{c,o}$) as a function of the condenser temperature, wick structure, wall geometry, and heat load. Figure 4.8 shows the comparison of the thermal network model and the steady state experimental data for an axially grooved aluminum/oxygen heat pipe tested by Edelstein and Kosson (1992). Expressions for the effective conductivity for axial grooves are presented by Peterson (1991) and Faghri (1995). The agreement between the thermal network model and the experimental data is good.
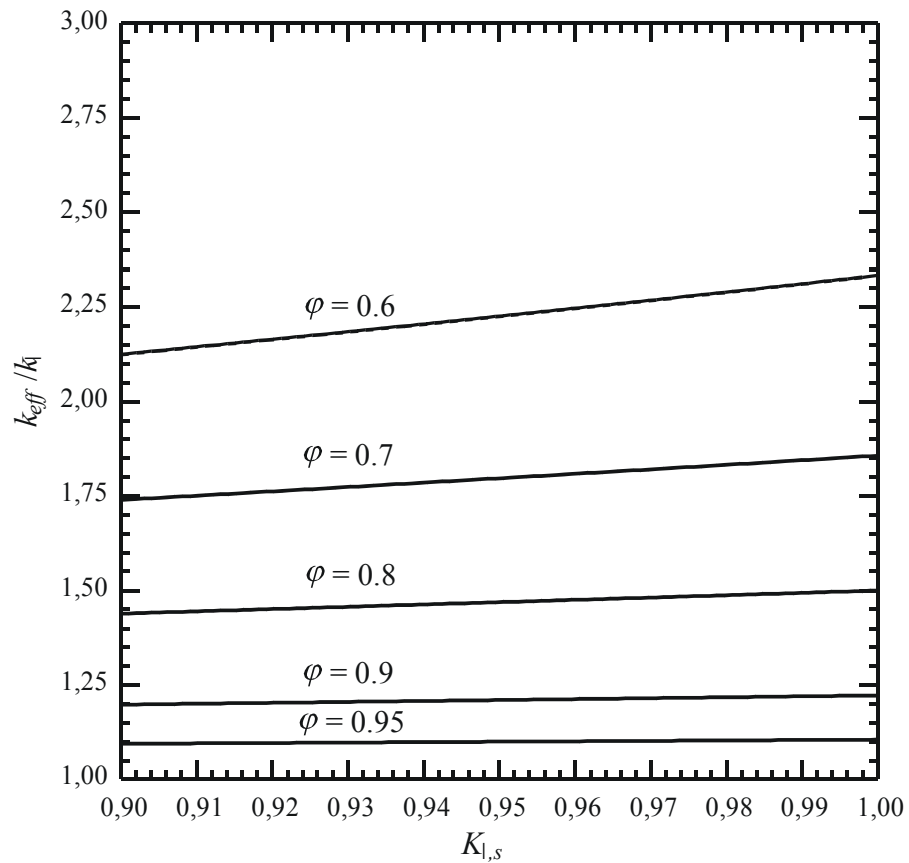
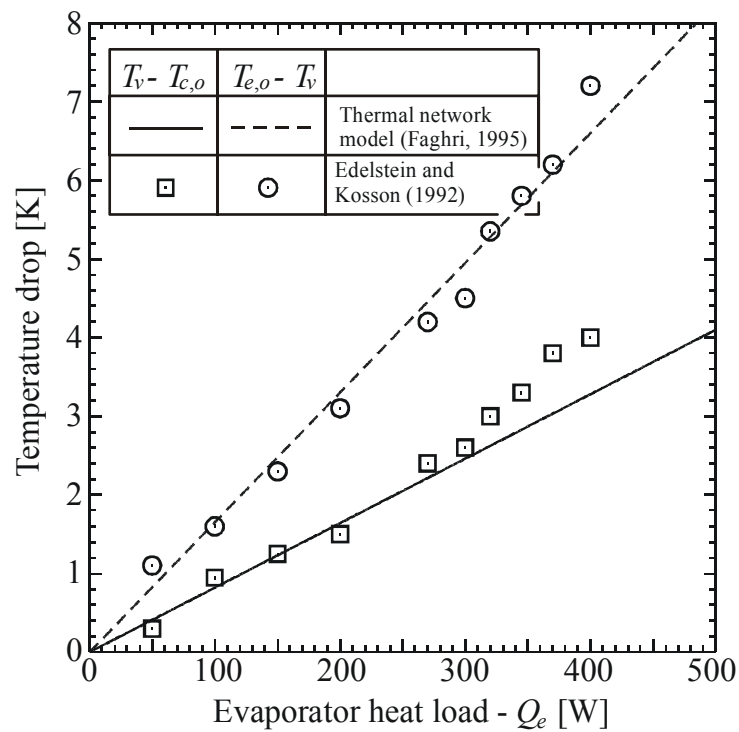Figure 4.7. Effective conductivity sensitivity analysis.

Figure 4.8. Comparison between the thermal network model and experimental data for oxygen/aluminum cryogenic heat pipe[10].

---

[10] Experimental data from literature: Edelstein and Kosson (1992).

The thermal network model is used now for an estimation of the temperature drop in a stainless steel nitrogen heat pipe as a function of the condenser temperature for different wick structures and wall geometries, which are shown in Figures 4.9 through 4.12. Lines of constant heat load are also shown, as well as the maximum heat load line, obtained from Eq. (4.4). For these figures, the length of the condenser was considered equal to the length of the evaporator. Graphs "A" refer to a condenser length of 0.1 m while graphs "B" refers to a condenser length of 0.2 m. The adiabatic section length was 0.8 m for all figures. Each figure shows the temperature drop for two different wick structure thickness, δ_w. The data on Figures 4.9 and 4.10 account for a metal screen Mesh 160 while Figures 4.11 and 4.12 account for a metal screen Mesh 254.

From Figure 4.9, a nitrogen/stainless steel cryogenic heat pipe with a external diameter of ¾" and a wick structure composed of 4 layers of screen Mesh 160 (δ_w = 0.812 mm) operating at 100 K with a heat load of 0.4 W would have a temperature drop of 0.3 K. The same device with a thicker wick structure (8 layers of screen Mesh 160 - δ_w = 1.676 mm) would have a temperature drop of 0.7 K. This is because a thicker wick structure produces a larger thermal resistance. In the other hand, a thicker wick structure increases the liquid flow area, which reduces the liquid friction factor [see Eq. (4.5)], thus providing a larger maximum heat transport capacity: 0.6 W.m for 4 layers of screen Mesh 160, and 1.3 W.m for 8 layers of screen Mesh 160. Also, a longer condenser and evaporator lengths reduce the temperature drop (graphs A and B in Figure 4.9). This is because longer condenser and evaporator lengths increase the heat transfer cross sectional area, reducing the heat load concentration (W/m^2).

By comparing Figures (4.9) and (4.10) it can be observed that a ½" diameter heat pipe produces the same temperature drop as the ¾" diameter heat pipe, but at a lower heat load level. Also, the maximum heat transport capacity decreases as the external diameter decreases (see Figure 4.2).

In general, the heat pipes with a wick structure composed of metal screen mesh 254 (Figures 4.11 and 4.12) presents a lower temperature drop when compared to those with screen mesh 160. This is because the screen mesh 254 provides a thinner wick structure than the screen mesh 160, reducing the thermal resistance of the wick structure. In the other hand, the lower permeability of the screen Mesh 254 (when compared to the screen Mesh 160) decreases greatly the maximum heat transport capacity (see Figures 4.2, 4.3 and 4.4).

From this analysis, a heat pipe with a ¾" external diameter, wick structure composed of 8 layers of stainless steel screen Mesh 160 and a long condenser and evaporator length is recommended for ground testing.
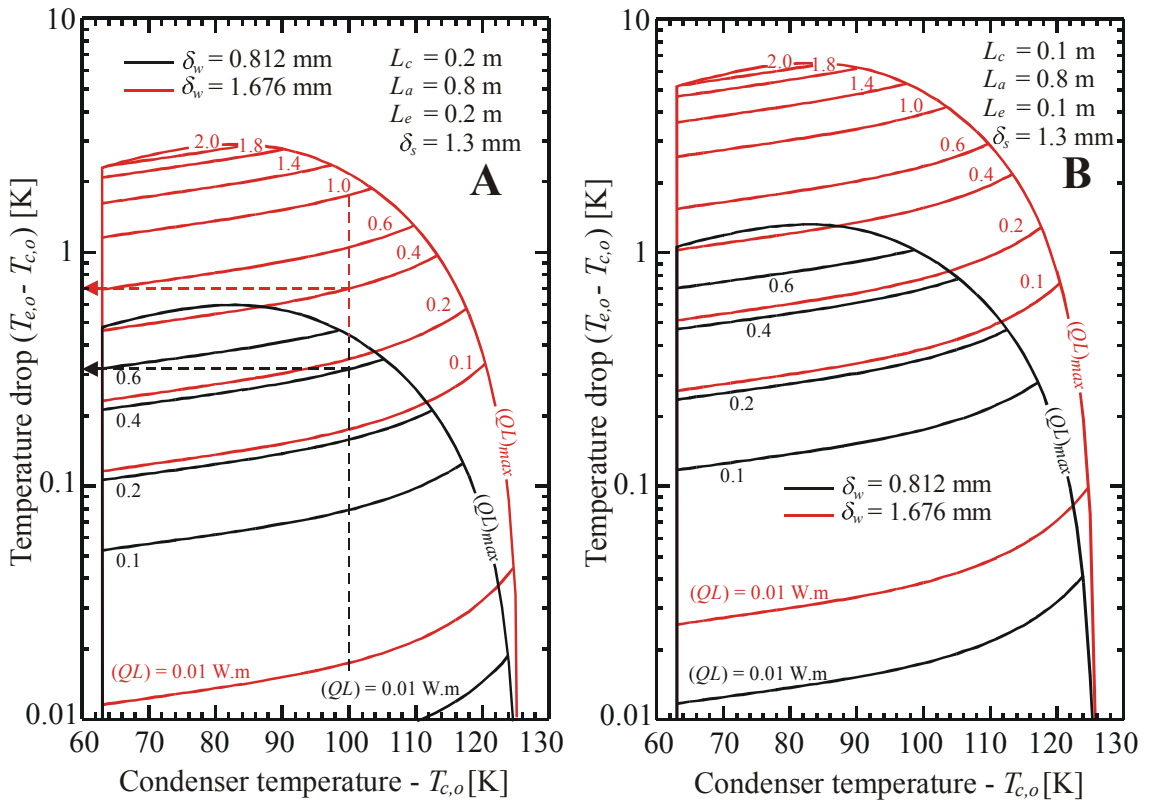
Figure 4.9. Temperature drop as a function of the condenser temperature and heat load.

(Mesh 160, $\varnothing_{ext}$ = ¾", wall material: AISI 304 stainless steel, wick
material: AISI 316 stainless steel, working fluid: nitrogen)
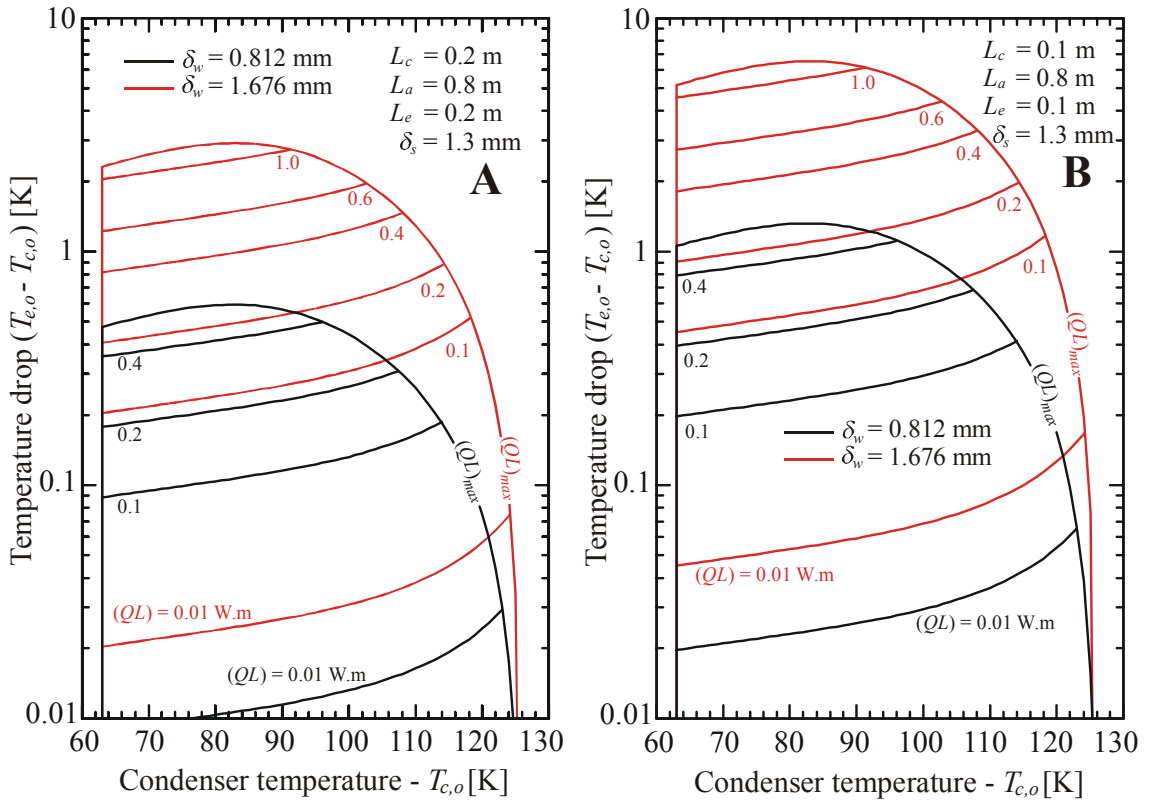

Figure 4.10. Temperature drop as a function of the condenser temperature and heat load.

(Mesh 160, $\varnothing_{ext}$ = ½", wall material: AISI 304 stainless steel, wick
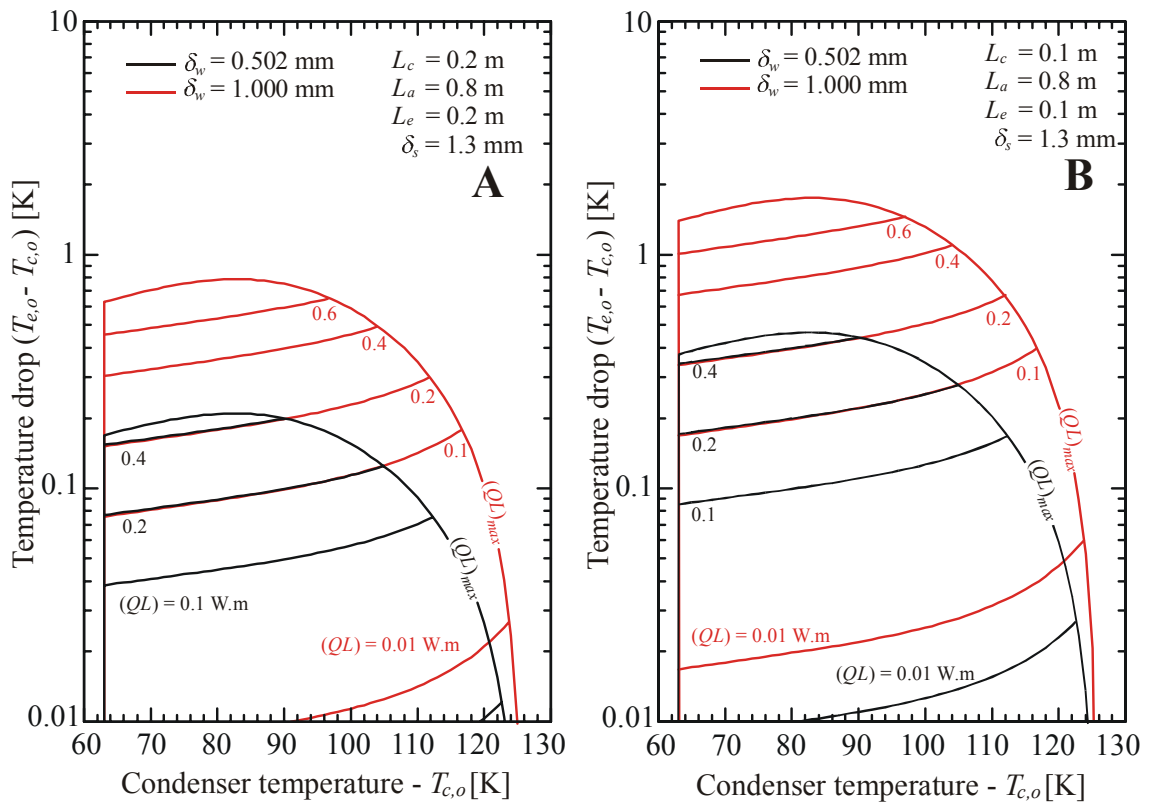material: AISI 316 stainless steel, working fluid: nitrogen)

Figure 4.11. Temperature drop as a function of the condenser temperature and heat load.

(Mesh 254, $\varnothing_{ext}$ = ¾", wall material: AISI 304 stainless steel, wick
material: AISI 316 stainless steel, working fluid: nitrogen)
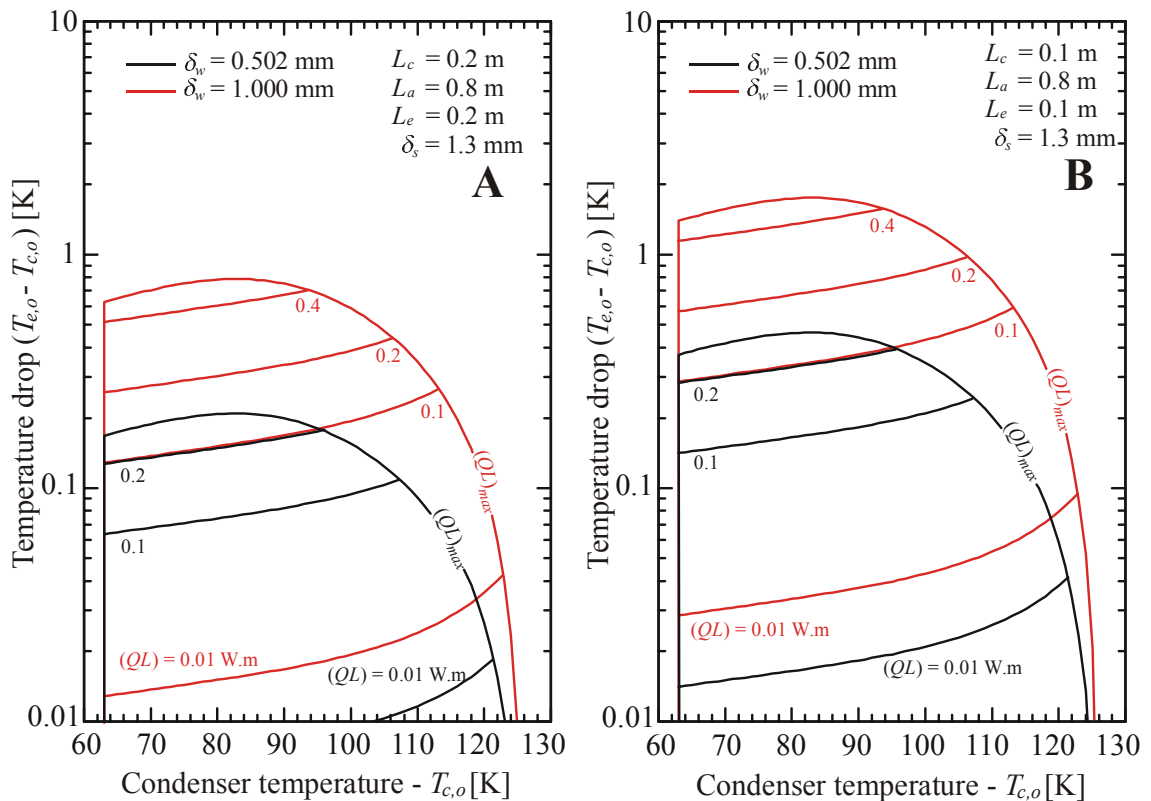

Figure 4.12. Temperature drop as a function of the condenser temperature and heat load.

(Mesh 254, $\varnothing_{ext}$ = ½", wall material: AISI 304 stainless steel, wick
material: AISI 316 stainless steel, working fluid: nitrogen)

4.2.3 Design Summary

The heat transport analysis and the steady state performance analysis provided some criteria for the definition of the geometry of the nitrogen/stainless steel heat pipe for ground tests, which are summarized in Table 4.3. The up arrow indicates an increase in ΔT or $(QL)_{max}$ while the down arrow indicates a decrease.

Table 4.3. Changes in ΔT and $(QL)_{max}$.

Increase in:	Temperature drop ΔT	Maximum heat transport capacity $(QL)_{max}$
Wick thickness, δ_w (↑)	↑	↑
External diameter, $\varnothing_{ext}$ (↑)	↓	↑
Condenser length, L_c (↑)	↓	-
Mesh number (↑)	↓	↓

Table 4.4 shows the design parameter selected for the nitrogen/stainless steel cryogenic heat pipe according to the criteria shown in Table 4.3, and according to the geometry of the tubes and metal screen available.

Table 4.4. Nitrogen/stainless steel cryogenic heat pipe design summary.

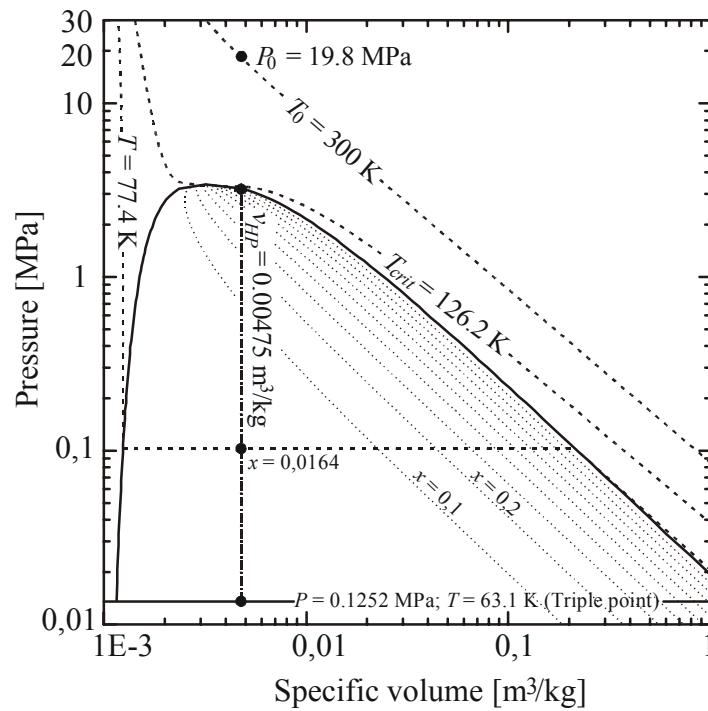|	
Tube material:	AISI 304 Stainless Steel
Tube dimensions:	
Outer diameter	19.05 mm (3/4")
Wall thickness	1.3 mm
Lengths:	
Evaporator	0.30 m
Condenser	0.30 m
Transport section	0.20 m
Nitrogen charge:	31.1 g
Vapor pressure:	
At 300 K	19.8 MPa
At 77.4 K	0.1 MPa
Maximum heat transport capacity (temperature)	2.2 W.m (82 K)
Wick structure:	Metal screen
Mesh	160
Number of layers	8
Thickness	1.676 mm

Figure 4.13. Pressure-specific volume diagram for the proposed cryogenic heat pipe.

4.3 Experimental Facility

The experimental setup used for the tests of the device described in the last subsection consists of a horizontal vacuum chamber (1200 mm long, ∅200 mm ID) and a calorimeter (2.2 liters) through which flows liquid nitrogen. Figure 4.14 shows the vacuum chamber schematic. To accommodate different heat pipe geometries, the calorimeter has an internal cavity with a diameter larger than the external diameter of the heat pipes. A brass sleeve fills the gap between the calorimeter and the heat pipe, to provide a prescribed temperature boundary condition at the condenser region. The temperature at the sleeve is monitored and its distribution is used as the boundary condition for the theoretical model presented in Section 4. Latter, a new calorimeter (2.4 liters) was developed to allow direct contact between the liquid nitrogen and the heat pipe condenser section, providing more cooling capacity to the experimental setup.

The vacuum chamber is connected to an Edwards® RV8 rotary vacuum pump. The pressure in the vacuum chamber is monitored using an active pressure gauge Edwards® APG-M connected to an Edwards® AGD display. At one side of the vacuum chamber, there is a feedthrough for 36 T-type thermocouples and two pairs of electrical connections. The electrical connections will allow the heat generation inside the chamber for tests to be conducted in the future. At the other side of the vacuum chamber, there is a pair of feedthrough where the liquid nitrogen (LN2) flows to the calorimeters. A vacuum relief valve

is also installed on the plate. Two brass sleeves embrace the condenser region of the heat pipe, to fit inside the calorimeter. Figure 4.15 shows the vacuum chamber and the complete experimental setup.
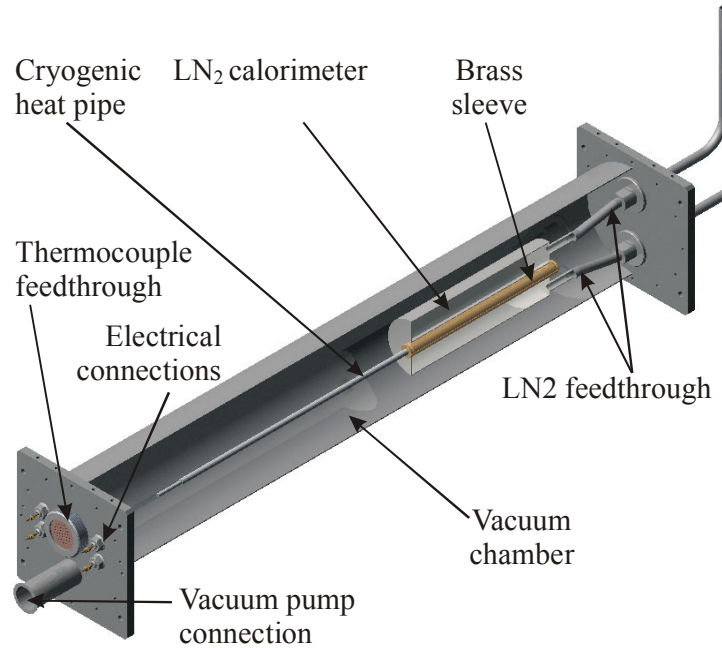

Figure 4.14. Vacuum chamber schematic (partial section).

Figure 4.15. Vacuum chamber (left) and experimental setup (right).

4.4   Heat Pipe Instrumentation

The condenser region of the heat pipe was placed in the calorimeter, while the remaining length was covered with a multi-layer insulation (MLI) composed of 10 layers of aluminum foils each one separated by one nylon screen to avoid radiative conduction of parasitic heat loads. A Hewlett-Packard[®] 34970A Data Acquisition Unit was used to monitor the temperature of 16 Omega[®] T-type AWG40 thermocouples that were installed at the external wall of the heat pipe (see Figure 4.16). Also, the temperature of the following items

was monitored for future parameter estimation: filling valve of the heat pipe; vacuum chamber inner wall; outer and inner layer of the heat pipe's MLI; brass sleeves; and calorimeter. All the thermocouples were thermally grounded to the calorimeter to avoid parasitic heat leakage through the wires.
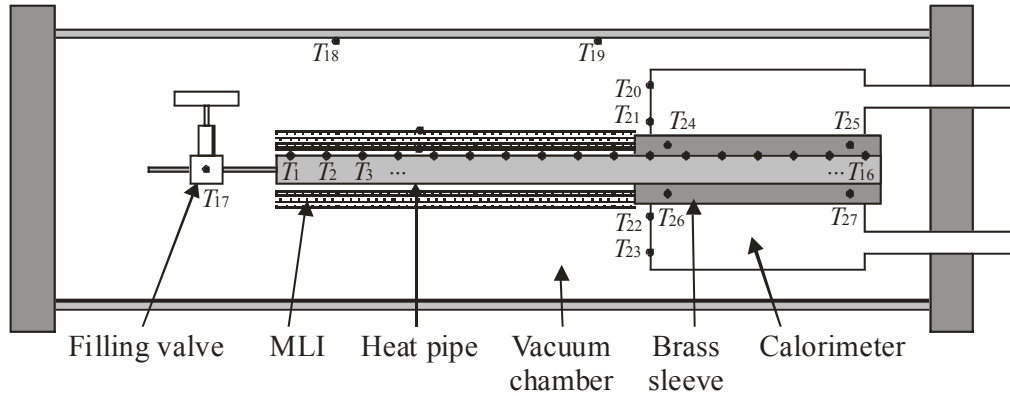

Figure 4.16. Thermocouple positions.

4.5 Uncertainty Analysis

The thermocouples were calibrated at two reference temperatures: ice point temperature at one (01) atmosphere (273.15 K ≡ 0°C) using an Hg precision thermometer and saturation temperature of liquid nitrogen at one (01) atmosphere (77.4 K). At the ice point temperature, the T-type thermocouples presented a random error of ±0.1 K and a systematic error of 0.2 K, while at nitrogen saturation temperature the readings were 73.9 K ± 0.3 K, showing a systematic error of −3.5 K. The variation of the systematic error and random error between 273.15 K and 77.4 K was considered linear:

$$\varepsilon_s = \left(\frac{0.2 - 3.5}{273.15 - 77.4} \right)(Y - 77.4) + 3.5 \tag{4.16}$$

$$\varepsilon_r = \left(\frac{0.1 - 0.3}{273.15 - 77.4} \right)(Y - 77.4) + 0.3 \tag{4.17}$$

where Y is the measured temperature as given by the data acquisition system.

The corrected value of the measured temperature is given by:

$$T = Y + \varepsilon_s \pm \varepsilon_r \tag{4.18}$$

where ε_s is the systematic error and ε_r is the random error.

The measurement of temperature at cryogenic levels is very difficult to be performed. At such low level of temperature, the heat conduction by the thermocouple wires can affect the measured data. The data acquisition system is at room temperature, and to avoid the heat conduction from the data acquisition system, the thermocouple wires are thermally grounded at the calorimeter. The heat conduction through the grounded thermocouple wires can be calculated by:

$$Q_{wire} = n \frac{\pi d_w^2 \Delta T}{4L} \left(k_{Cu} + k_{Co} \right) \tag{4.19}$$

where n is the number of thermocouples, d_w is the thermocouple wire diameter, ΔT is the difference between the local heat pipe temperature and the calorimeter temperature, L is the wire length and k_{Cu} and k_{Co} are the conductivity of the copper and the constantan wires (for a "T" type thermocouple). For a temperature difference of 49 K between the calorimeter and the heat pipe (77 K – 126 K), the heat transferred through the thermocouple wires is 2×10^{-3} W, while at 100 K the heat transport capacity of the heat pipe is 2.2 W. Therefore, the heat lost by conduction through the thermocouple wires is less than 0.1% of the heat pipe transport capacity, being negligible.

4.6   Experimental Procedure

The experimental procedure consists of cleaning, assembling, charging and testing the heat pipe. End-caps were machined and welded to the heat pipe container. The inner surface of the end-caps were machined with a hemispherical shape to avoid sharp corners, which are sensitive to cracking due to the high internal pressure of the heat pipe at room temperature. Figure 4.17 shows a welded end-cap that was cut in its cross section to check the penetration of the welding in the screen wick. It was observed that the welding penetrated completely the wick structure thickness forming a sort of a reservoir at the tip of the end-cap. A filling tube ($^1/_8$" external diameter, 50 mm long) was also machined.

4.6.1 Cleaning

The heat pipe container, metal screen, end-caps and filling tube were cleaned in an ultrasonic cleaning bath, using trichloroethane for degreasing and solid particle removal. After cleaning, a passivation process was performed to remove any iron or copper particles that may

be adhered to the surface of the parts. This process consists in immersing the parts in a solution of 60% nitric acid and deionized water for 2 hours. After the passivation, the parts were wrapped in plastic to prevent contamination prior to assembly.
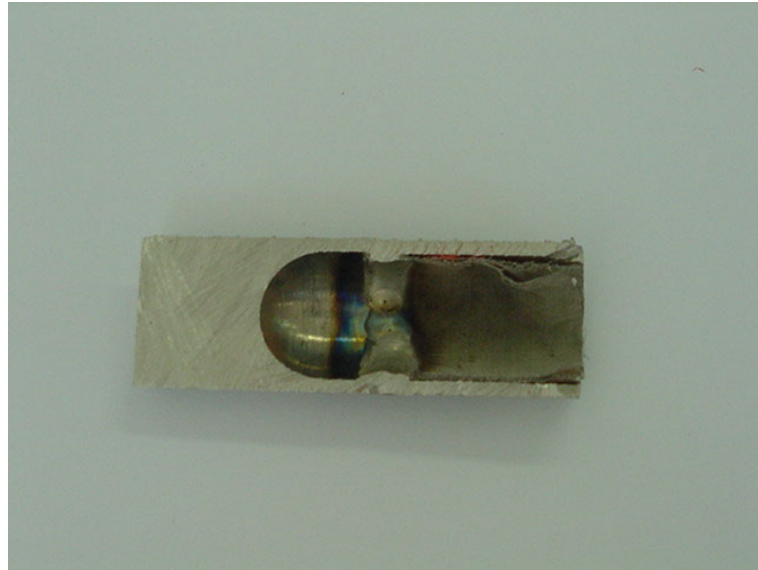

Figure 4.17. Hemispherical end-cap.

4.6.2 Assembling

A metal screen wick mesh 160 was wrapped inside the heat pipe container in order to obtain a wick structure with 8 layers. The material of the metal screen is AISI 316 stainless steel. The end-caps and filling tube were welded to the container by a TIG process. The heat pipe was filled with argon gas to prevent oxidation during the welding process. After welding, the heat pipe was cleaned again as described before. A Swagelok® needle valve was connected to the filling tube to seal the heat pipe after charging.

4.6.3 Charging

The heat pipe was charged with 99.99% pure nitrogen. The process was performed at room temperature. Figure 4.18 shows a schematic for the charging process. The heat pipe was connected to an Edwards® RV8 rotary vacuum pump for evacuation to a pressure of 2×10^{-3} mbar. The needle valve was closed and the pump was disconnected. The heat pipe was weighted empty, prior the charging process. After weighting, the heat pipe is connected to a high-pressure cylinder containing pure nitrogen gas, a pressure control valve, a pressure transducer and a pressure relief valve. With the needle valve closed, the relief valve and the pressure control valve are opened to flood the piping with nitrogen gas. The relief valve is

closed and the needle valve is opened. In this moment, the high pressure of the nitrogen in the piping added to the vacuum inside the heat pipe charges the device. The pressure control valve is set to a pressure higher than that required for the heat pipe charging at room temperature. To maximize the fluid charge when the nitrogen cylinder is at low pressures, the heat pipe wall can be cooled with a LN_2 bath to decrease its temperature and therefore, charging pressure. The pressure control valve is closed and the needle valve is closed. The relief valve is opened to vent the gas from the piping and the heat pipe is disconnected. The heat pipe is weighted again, and compared to the empty weight. The difference gives the working fluid charge. Any excess of fluid is then vented by the needle valve, and the heat pipe is weighted again.
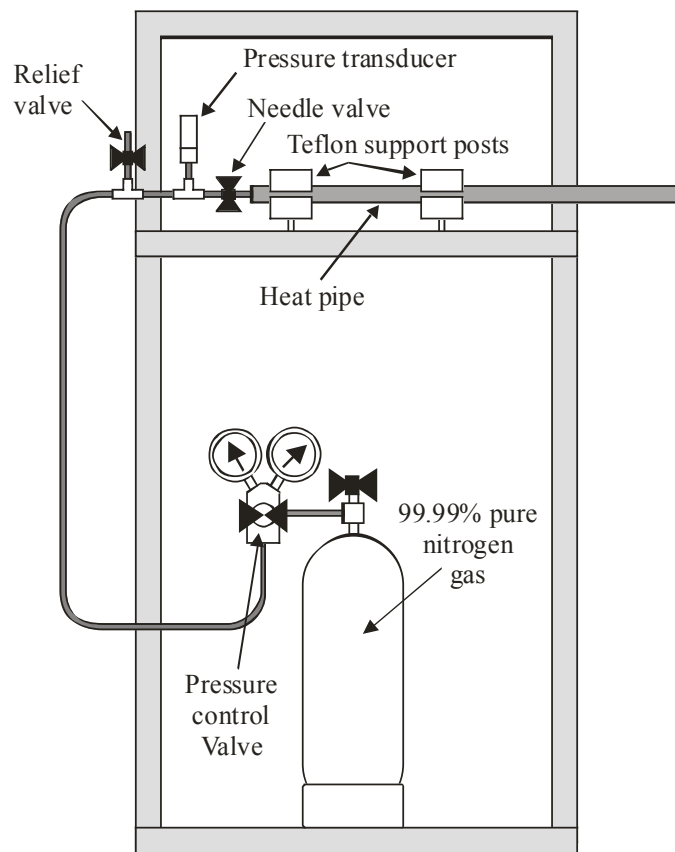

Figure 4.18. Charging apparatus.

4.6.4 Testing

The heat pipe testing consists of cooling the heat pipe's condenser to a temperature below the critical temperature of the nitrogen (126.2 K), in a vacuum environment. Initially, the heat pipe is at room temperature. The preparation for the test begins with the evacuation of the vacuum chamber using the rotary pump. When the pressure is below 2×10^{-2} mbar, the data acquisition system is activated and the calorimeter is flooded with liquid nitrogen,

cooling the brass sleeve and therefore, the condenser region. The temperature of the calorimeter is constantly monitored to avoid a dry-out, which would lead to a temperature increase of the condenser. The test is finished when the largest temperature variation observed is less than 1 K per hour (steady-state condition).

4.7   Summary and Conclusions

The design analysis of a nitrogen/stainless steel cryogenic heat pipe was presented. The design procedure was based on the heat transport capacity and steady state performance of the heat pipe. A simple model for the steady state performance (Faghri, 1995) was successfully implemented and compared well with experimental data available in the literature (Edelstein and Kosson, 1992). This model was used to determine the temperature drop between the condenser and evaporator sections as a function of the heat load, and it can be used to estimate the parasitic heat load based on experimental steady state data.

The experimental setup built at the Satellite Thermal Control Laboratory of the Federal University of Santa Catarina, Brazil, for further testing of cryogenic heat pipes was described. Also, the instrumentation of the heat pipe was presented and the uncertainty of the measurements was discussed.

Finally, the experimental procedure, including cleaning, assembling, charging and testing of the nitrogen/stainless steel cryogenic heat pipe was discussed. The procedure is in agreement with standard procedures for heat pipe testing described in the literature.

4.8   Synopsis

Uma análise do projeto de um tubo de calor criogênico de aço inox/nitrogênio foi apresentado. A análise do projeto foi efetuada baseada na capacidade de transporte de calor e desempenho em regime permanente do tubo de calor. Um modelo simples para prever o desempenho em regime permanente (Faghri, 1995) foi implementado com sucesso e os dados teóricos estão em boa concordância com dados experimentais disponíveis na literatura (Edelstein e Kosson, 1992). Este modelo foi usado para determinar a diferença de temperatura entre a seção do condensador e a seção do evaporador em função da carga térmica imposta no tubo, e pode ser usado também para o cálculo da carga térmica parasita com base em dados experimentais em regime permanente.

O aparato experimental construído no Núcleo de Controle Térmico de Satélites da Universidade Federal de Santa Catarina, Brasil, para posteriores testes de tubos de calor

criogênicos foi descrito. Também, a instrumentação do tubo de calor foi apresentada e a incerteza das medições foi discutida.

Finalmente, o procedimento experimental, incluindo a limpeza, a montagem, a carga e testes do tubo de calor criogênico de aço inox/nitrogênio foi discutido. O procedimento está de acordo com procedimentos padrões para testes de tubo de calor descritos na literatura.

5.1   Introduction

The results obtained from the experiments described in the last chapter are presented in this section. Several experimental runs were performed during the year of 2002 at NCTS/UFSC to study experimentally the supercritical startup of cryogenic heat pipes. These data are compared with theoretical results obtained from the model presented in Chapter 3. Pressure-specific volume diagrams for some experimental tests are shown to help in the understanding of the startup process. Conclusions regarding the experiments are presented at the end of this chapter.

5.2   Results and Discussion

Several tests were conducted at the laboratory, but only those which results are important for the present study are reported in this chapter. The Root Mean Square Error (RMSE) and the Mean Bias Error (MBE) for the comparison between experimental data and theoretical results for transient and steady state operation of the cryogenic heat pipe are also presented. The RMSE quantifies the dispersion of the theoretical results relative to the theoretical data, while the MBE quantifies the deviation of the theoretical results relative to the experimental data. The RMSE and the MBE expressions are given by Holman (1994):

$$\text{RMSE} = \frac{\sqrt{\sum_n (T_n - Y_n)^2 \big/ N}}{\sum_n Y_n \big/ N} \times 100 \tag{5.1}$$

$$\text{MBE} = \sum_k \left[\frac{(T_n - Y_n)/Y_n}{N} \right] \times 100 \tag{5.2}$$

where T_k and Y_k are the theoretical and the experimental data respectively, and N is the total number of data available for comparison.

Experiment 1: April 18ᵗʰ, 2002:

The first test of the nitrogen/stainless steel heat pipe constructed at the LABSOLAR/ NCTS was performed on the April 18ᵗʰ, 2002. After the heat pipe charging process, it was observed that there was a fluid charge deficiency of almost 30%. This was due to leaks on the pipe fittings of the charging apparatus (fixed later) added to inaccuracy of the pressure control valve. Even if the working fluid charge was less than that designed, the tests with this heat pipe were carried out to check other problems that may come to occur in the experimental apparatus. The condenser region of the heat pipe was fitted to the calorimeter using the brass sleeves, and the vacuum chamber was closed and evacuated to a pressure of 4×10^{-2} mbar. Vacuum leakage on the experimental apparatus prevented a lower level of vacuum. No MLI was used on the transport and evaporator section of the heat pipe. At this point, the data acquisition system was activated, and the calorimeter was flooded with liquid nitrogen. After the flooding of the calorimeter, the pressure of the vacuum chamber increased to 0.1 mbar due to differential expansion of the LN_2 feedthrough at very low temperatures. This problem was fixed for later experiments.

Figure 5.1 shows the first experimental data obtained for the nitrogen/stainless steel cryogenic heat pipe (CryoNHP). The transient temperatures during the startup for different axial positions are presented. The heat pipe achieved a non-operational steady state after 1.5 hours of testing, with the liquid column stagnating at $x = 0.47$ m.

According to the measurement uncertainty discussed in Section 4.5, the parasitic heat load for this experiment was estimated to be $q_p = 3.90$ W $\pm$ 0.55 W. The estimation of the parasitic heat loads was performed based on the steady state temperature measurements and based on the network thermal model presented in Section 4.2.2. The total heat load, Q_e, on the network thermal model accounts for the parasitic and for the evaporator heat loads. It was considered that the primed length of the heat pipe ($L = 0.47$ m) was working as a heat pipe transporting the heat by conduction from the dry region and the parasitic heat load as well:

$$Q_e = q_{cond} + q_p \tag{5.3}$$

The total heat load, Q_e, can be estimated by using the network thermal model and the temperature difference measured between the liquid column edge ($Y|_{x=0.47 \text{ m}}$) and the condenser section ($Y|_{x=0}$).

The heat conducted from the dry region, q_{cond}, was estimated based on the first two temperatures measurement in the dry region ($Y|_{x=0.47 \text{ m}}$ and $Y|_{x=0.52 \text{ m}}$):

$$q_{cond} = k_s A_s \left.\frac{\Delta T}{\Delta x}\right|_{x=0.47} = k_s A_s \frac{(T|_{x=0.52} - T|_{x=0.47})}{(0.52 - 0.47)} \tag{5.4}$$

With the estimations of the heat conducted from the dry region, q_{cond}, and the total heat load, Q_e, the parasitic heat load, q_p, can be obtained from Eq. (5.3).

It can be observed that the calorimeter was able to cool the condenser region below the nitrogen critical temperature in less than 1 hour, and after 1.5 hours the condenser achieved a steady-state average temperature of 82 K. Also, after 1.5 hours, the heat pipe achieved a non-operational steady-state condition, where only 58% of the entire length (0.47m) was primed. Two possible reasons for this non-operational condition can be listed:

1. The parasitic heat loads from the environment increased the temperature gradient of the heat pipe during the startup, which was large enough to vaporize all the incoming working fluid at the liquid column leading edge at steady state ($x = 0.47$ m). Also, liquid was vaporized along the primed length of the heat pipe due to the parasitic heat load, reducing de liquid column momentum. The combination of these two effects decreased the rewetting velocity to zero after 1.5 hours of testing;

2. The fluid charge (~70% of the required fluid charge) was not sufficient to provide enough fluid for the liquid column to overcome the effects of the parasitic heat load. There was not enough working fluid to prime completely the heat pipe.
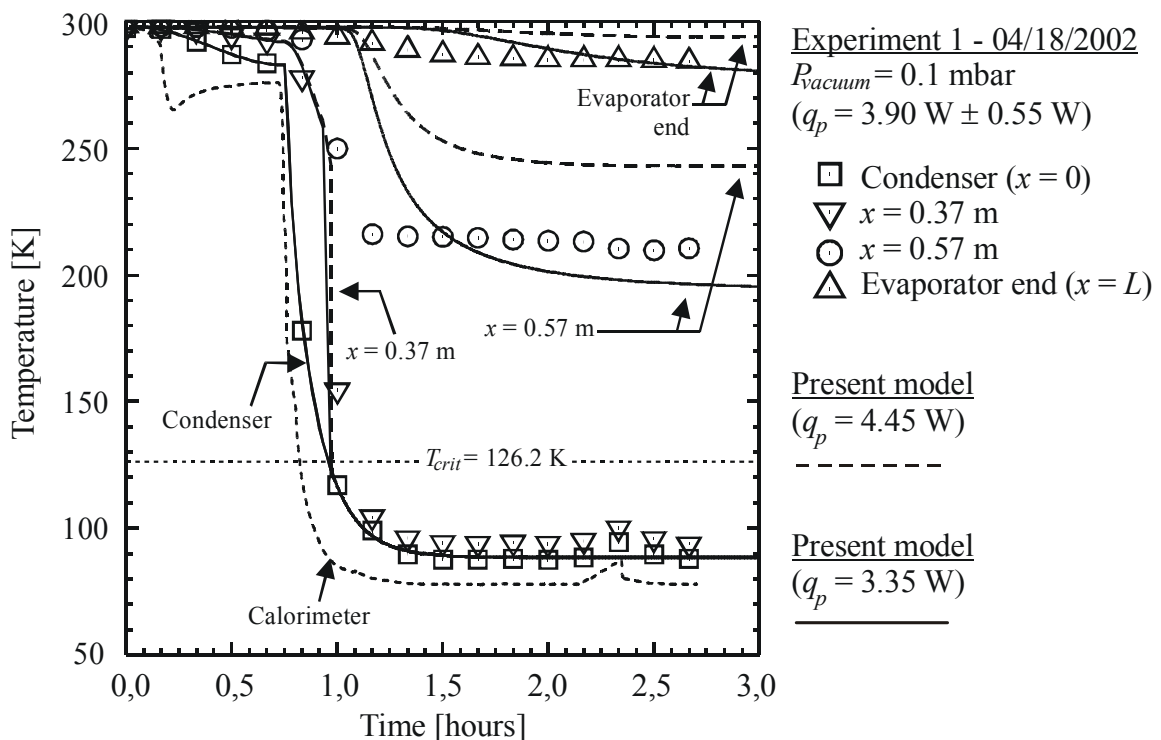

Figure 5.1. CryoNHP first test (04/18/2002) – Transient cool-down.

In fact, the working fluid mass of a heat pipe can be written in terms of the saturated liquid and vapor densities and of the liquid and vapor volumes:

$$m_f = \rho_\ell \, V_\ell + \rho_v V_v = \rho_\ell \, A_\ell \, L + \rho_v A_v L \tag{5.5}$$

Eq. (6.3) provides the working fluid mass, m_f, to prime completely a heat pipe with a defined geometry (L, A_ℓ, A_v) as a function of the saturation temperature. In the other hand, Eq. (6.3) can provide the maximum length L primed by a given working fluid mass as a function of the saturation temperature, which is shown in Figure 5.2. The total length of the heat pipe being tested is shown in dashed line. For this calculation, the working fluid mass in the dry region and the effects of the parasitic heat load were neglected for simplification. It can be observed that a heat pipe with a deficiency of working fluid charge would never prime completely. Also, it can be observed that an excess of 15% in the designed working fluid mass is required for the heat pipe to prime completely below 120 K.
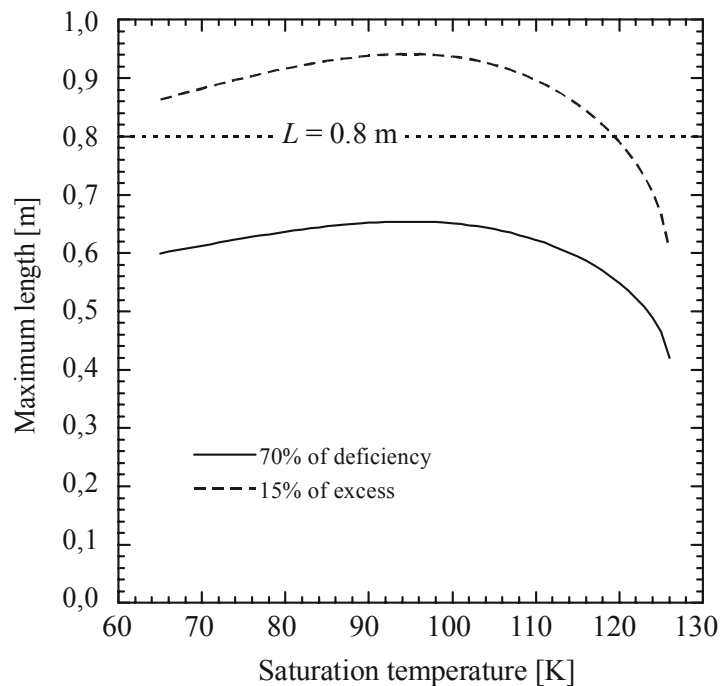

Figure 5.2. Maximum primed length.

Figure 5.3 shows the axial temperature profile during the startup for different times. The model was able to predict the steady state length of the liquid column as well as the steady state axial temperature profile of the first experiment, but in general, it overestimated the transient temperatures during the startup process of the heat pipe. This is because the model considers that any excess of condensed liquid is accumulated in the condenser as a

liquid slug (microgravity environment). In ground tests, the capillary forces cannot support a liquid slug across the vapor diameter and the excess of liquid spreads as a puddle and facilitates the priming of the heat pipe (Brennan *et al.* 1993). The excess of working fluid during the startup is shown in Figure 5.4, which presents the liquid fill rate for the 1st experiment.
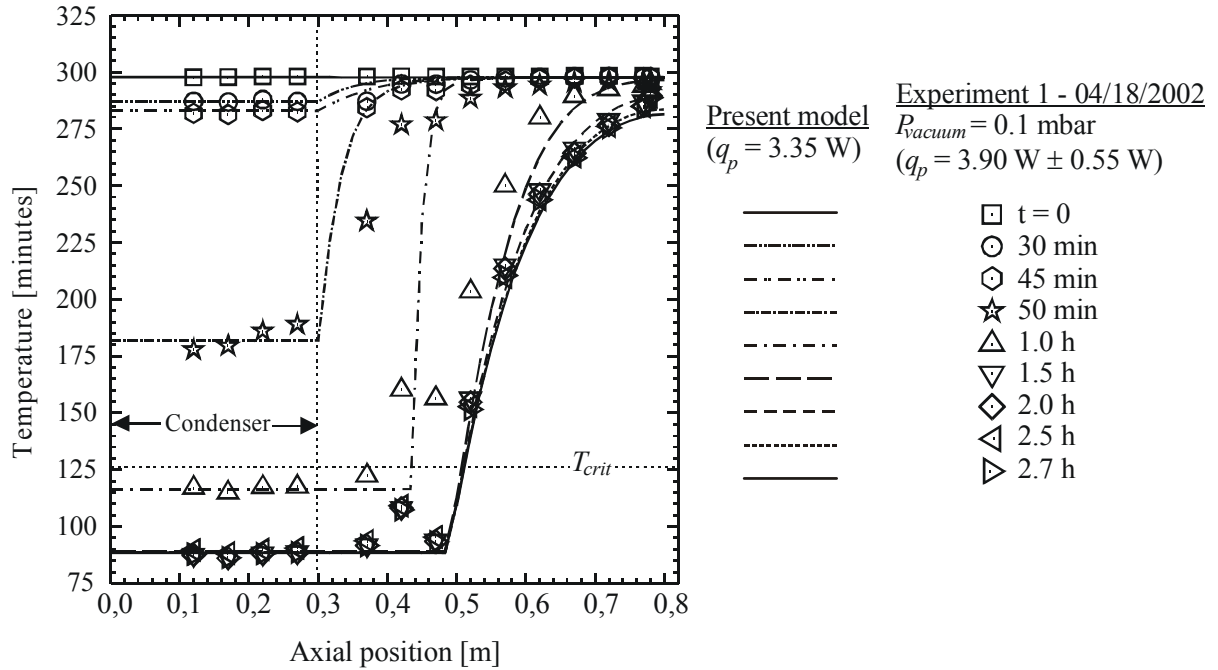

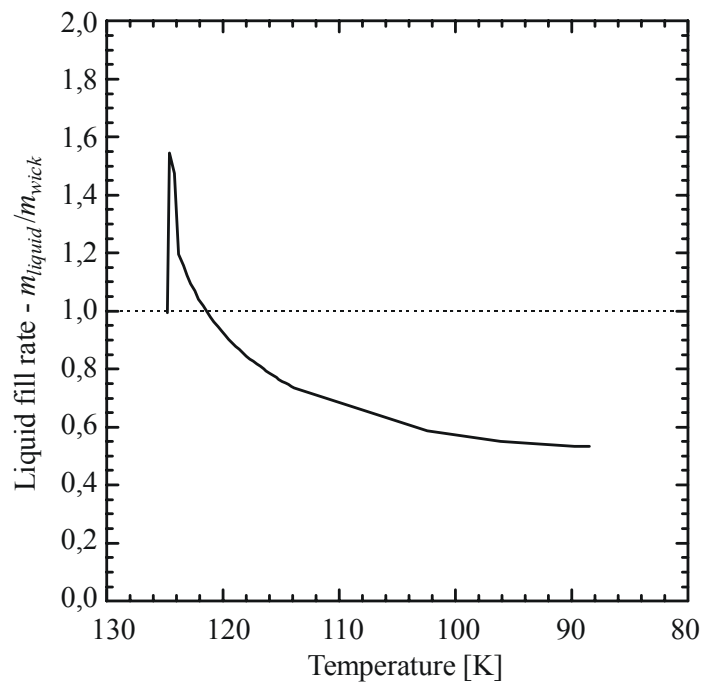Figure 5.3. CryoNHP first test (04/18/2002) – Temperature profiles.

Figure 5.4. Liquid fill rate (1st experiment).

Figure 5.5 shows the comparison between the transient experimental data and theoretical results with a ±10 % margin. The step on the temperature comparison at $x = 0.57$ m occurs because the experimental data was already stable around 210 K, while the temperature obtained from the model was still decreasing (see Figure 5.1). This step is observed, in a smaller scale at $x = L$ around 285 K. Figure 5.6 shows the comparison for the steady state operation. From this graphic it can be observed that the comparison is very good for steady state data.
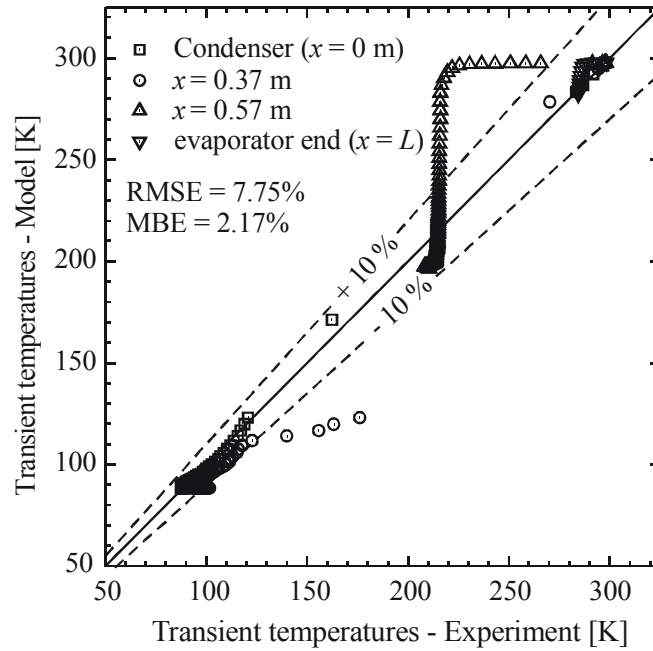

Figure 5.5. Transient experimental and theoretical data comparison.
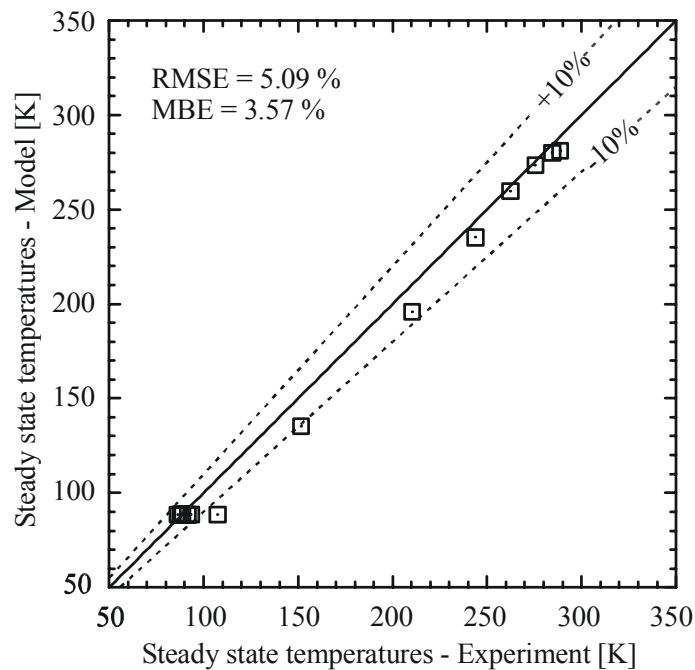

Figure 5.6. Steady state experimental and theoretical data comparison.

The theoretical pressure-specific diagram for the 1st supercritical startup experiment is shown in Figure 5.7, and Figure 5.8 presents the liquid column position as a function of time considering two different parasitic heat loads.

Other problems occurred during the first experimental run, such as disconnected or short-circuited thermocouples, which were fixed for the second test run.
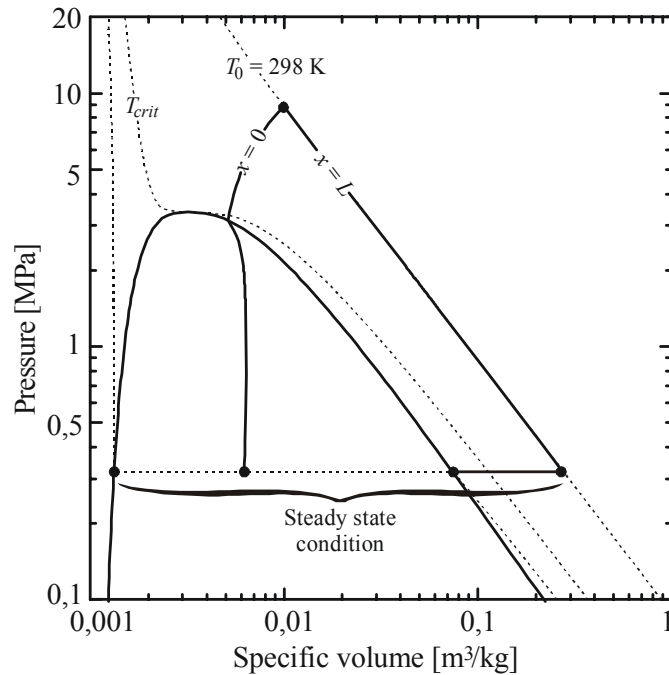
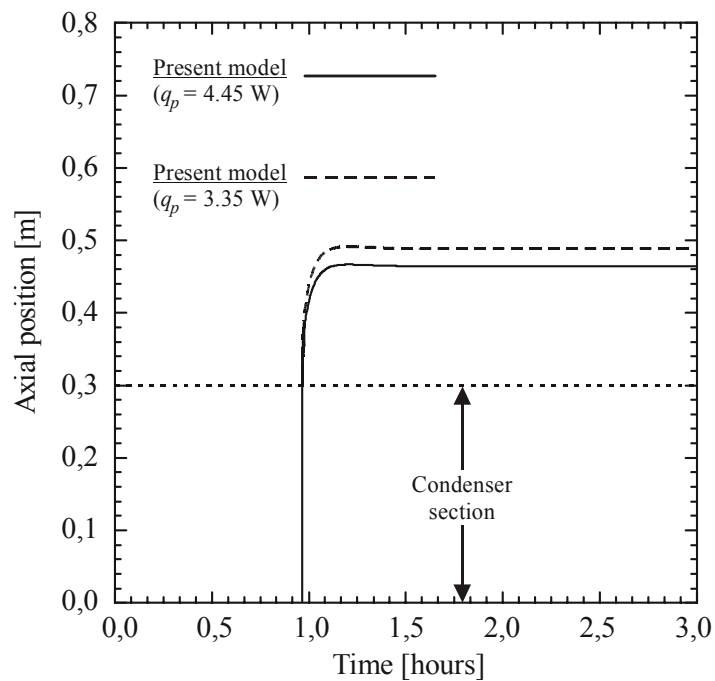Figure 5.7. Pressure-specific volume diagram (1st experiment).

Figure 5.8. Liquid column position (1st experiment).

Experiment 2: April 26th, 2002:

Two tests followed the first one with the same fluid charge on the heat pipe. These tests were performed to evaluate vacuum leak problems at the experimental setup and thermocouple connections to the heat pipe. However, the transport and evaporator sections of the heat pipe were covered with MLI. Figure 5.9 shows the temperature profile as a function of time for different positions along the heat pipe length obtained from the test performed at April 26th, 2002. The parasitic heat load estimated for this test was q_p = 2.95 W ± 0.49 W. For each thermocouple position, two curves were plotted: for the maximum parasitic heat load estimated (3.44 W) and for the minimum parasitic heat load (2.46 W). Again, a non-operational steady-state condition was observed after 1 hour, but the liquid column primed 78% of the length of the heat pipe (0.62 m). Although the heat pipe achieved a non-operational condition, the improved insulation decreased the effects of the parasitic heat load, allowing the liquid column leading edge to advance inside the heat pipe. With increased insulation, the effect of the deficiency of fluid charge seems to be more evident as the heat pipe could not prime completely.
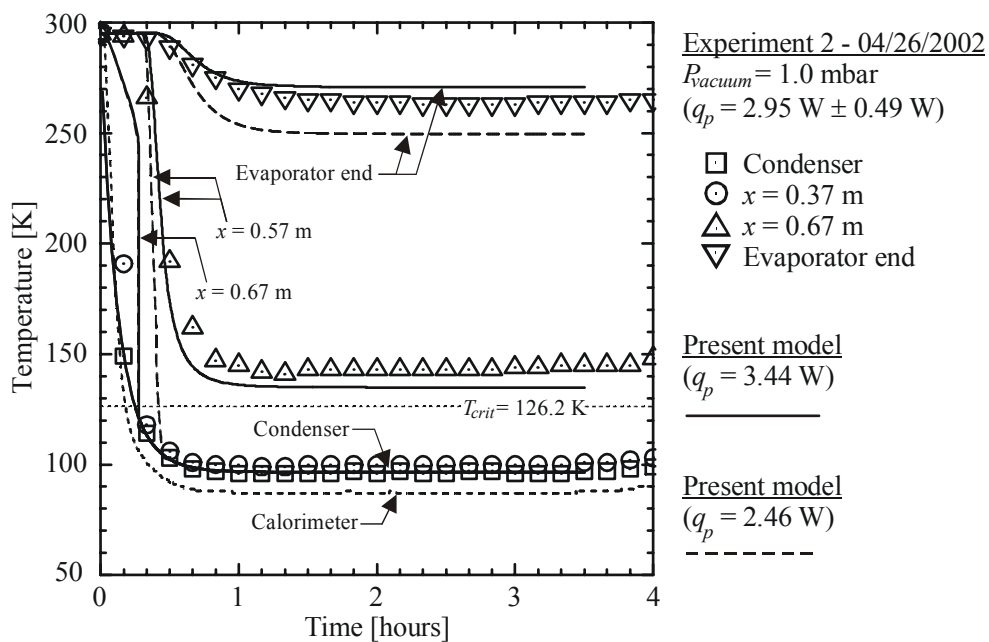

Figure 5.9. CryoNHP second test (04/26/2002) – Transient cool-down.

Figure 5.10 shows the comparison between the experimental and the theoretical temperature profiles for different times. Again, the model overestimated the temperatures during transient operation, but the model was able to reproduce the steady state conditions with a good accuracy.

The comparison between the experimental transient temperature measurements and the theoretical data is shown in Figure 5.11 with a ±10% margin of error, while Figure 5.12 shows the comparison for steady state operation.
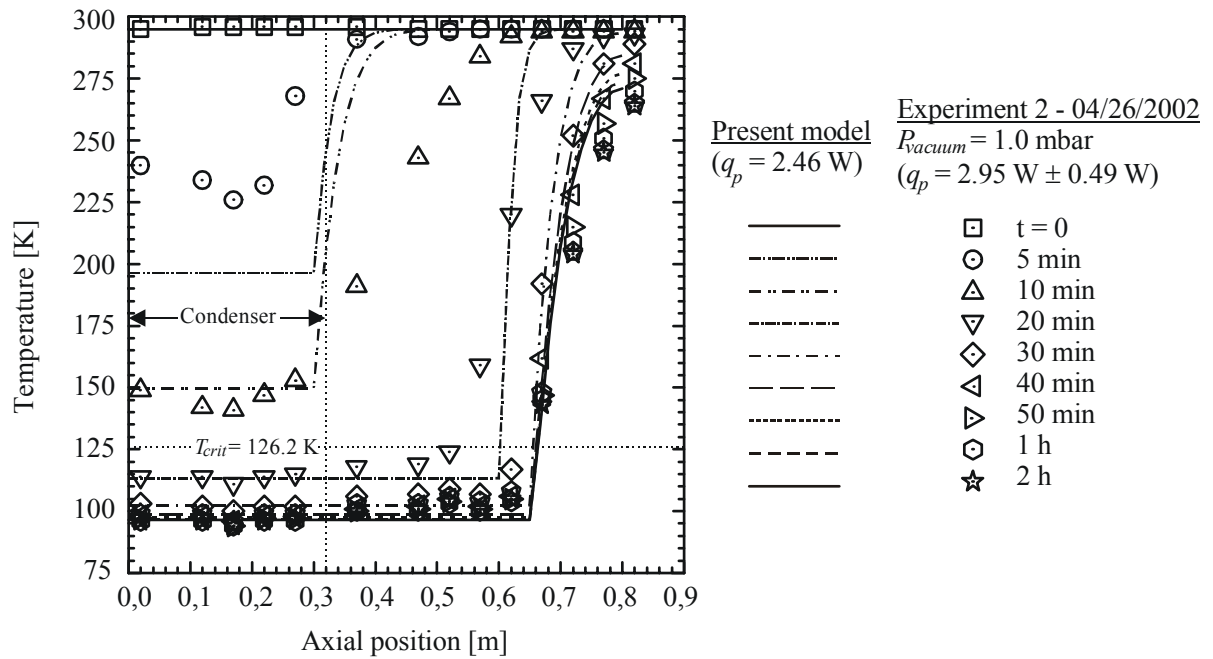

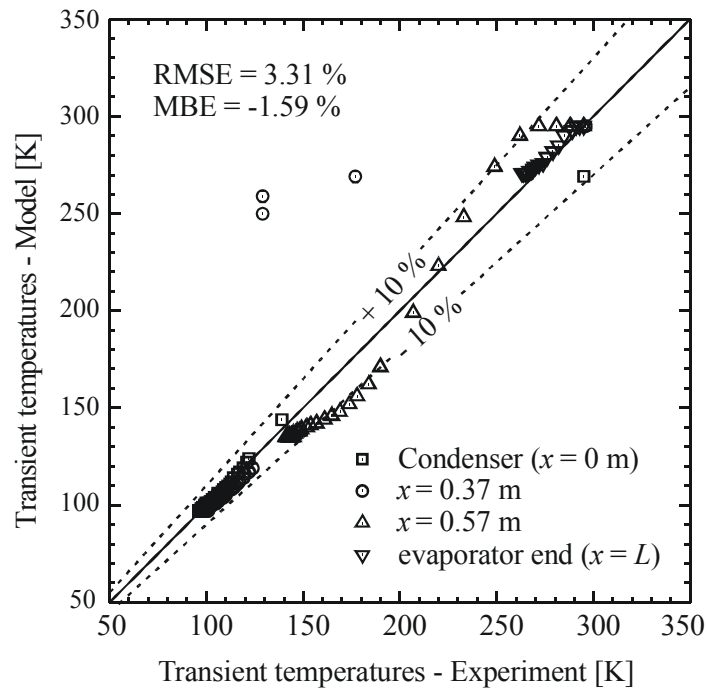Figure 5.10. CryoNHP second test (05/02/2002) – Temperature profiles.

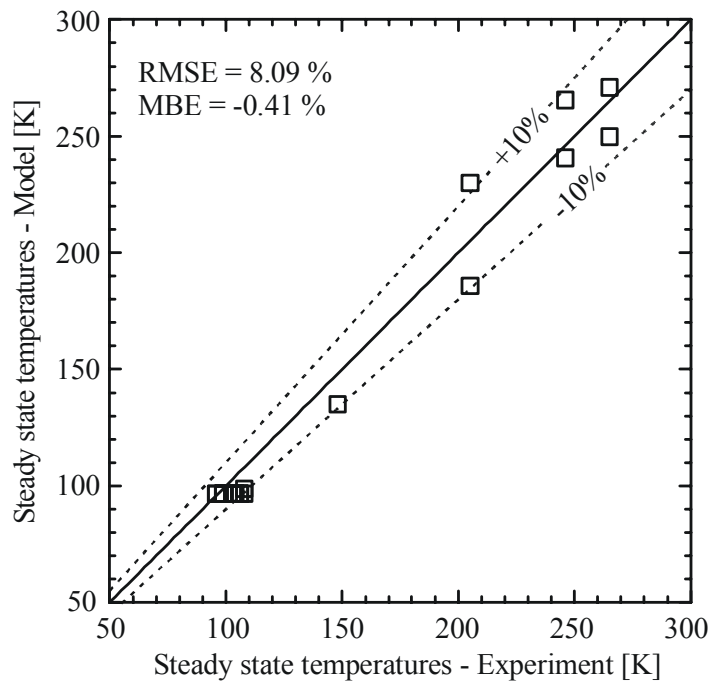Figure 5.11. Transient experimental and theoretical data comparison.

Figure 5.12. Steady state experimental and theoretical data comparison.

Experiment 3: May 2nd, 2002:

A third test was performed on the May 2nd 2002 with similar conditions to those of the 2nd test. The objective of this test was to verify the repeatability of experimental results. Figure 5.13 shows the experimental data obtained in this test. The vacuum chamber pressure was greater than that of the second test (10 mbar), but the experiment showed a good repeatability of results. The temperature at the evaporator end decreased from 280 K on the first test to 260 K and 255 K on the second and third tests, respectively. After the third test, the experimental setup was disassembled to fix the vacuum chamber leakage problems, and the heat pipe was vented and cleaned for re-charging and re-instrumentation.

Experiment 4: October 3rd, 2002:

New tests were performed in October 3rd, 2002. During the charging process, the heat pipe was immersed in a liquid nitrogen bath to decrease the wall temperature, because the pressure of the nitrogen gas cylinder was lower than that required for the charging process at room temperature. The heat pipe was charged with an excess of 27% of working fluid due to inaccuracy of the pressure control valve measurement.

The charged heat pipe was instrumented with 16 T-type thermocouples, and mounted at the calorimeter. The transport and evaporator sections of the heat pipe were covered withMLI, but the filling valve was not. A thermocouple was installed on the filling valve. The vacuum chamber was closed, evacuated to a pressure of 2×10^{-2} mbar, and the acquisition
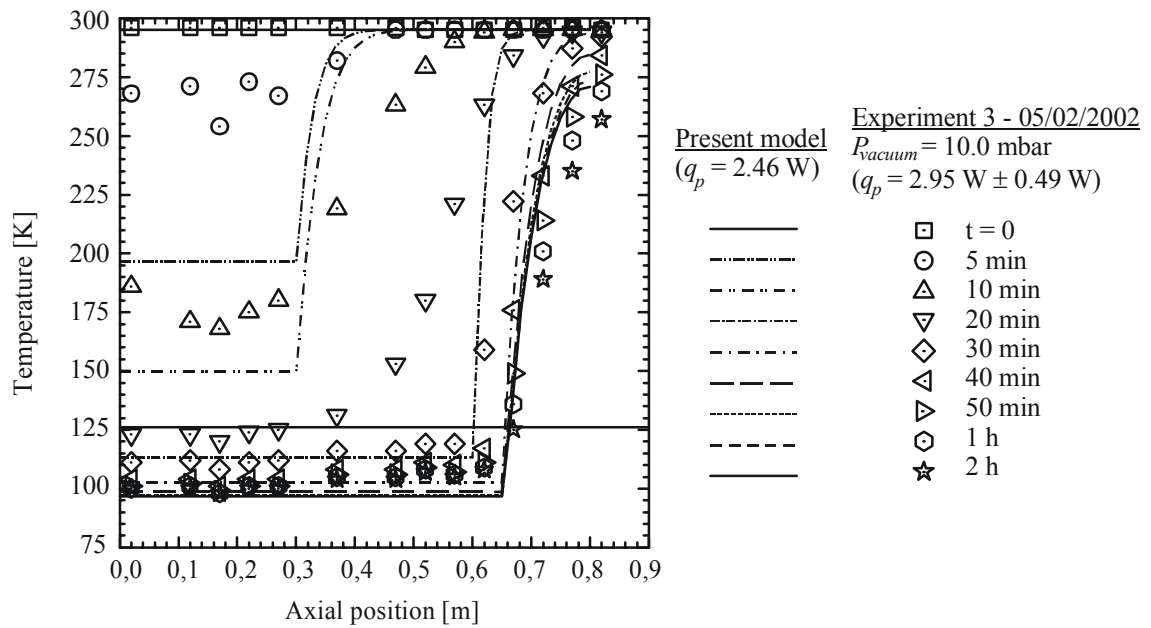
Figure 5.13. CryoNHP third test (05/02/2002) – Temperature profiles.

system was activated. Then, the calorimeter was flooded with liquid nitrogen, and no change at the vacuum chamber pressure was observed. Figure 5.14 shows the experimental temperature at different axial positions along the heat pipe length as a function of time obtained during this test. As the filling valve was not covered with MLI, there was a "leak" of parasitic heat load from the valve to the experiment. To account for this parasitic heat load, experimental data of the temperature of the filling valve and of the evaporator end were used to estimate the conductive heat load coming from the valve. This conductive parasitic heat load (heat flux) was used in the model as the boundary condition at $x = L$, instead of the isolation boundary condition. As the variation of the evaporator end temperature and filling valve temperature were not linear, the conductive parasitic heat load incoming from the valve was obtained as a function of time.

The condenser temperature reached the critical temperature of the nitrogen after 1hour and 20 minutes of test, but the pressure model indicates that the vapor pressure decreased below the critical pressure only after 2 hours, when the condenser temperature was at 118 K. The theoretical model indicates that the heat pipe would prime quickly (in 25 minutes) below 118 K, but in the other hand, the experimental data indicates that there was no priming and the heat pipe was cooled only by conduction (see Figure 5.15). Some possible reasons for the heat pipe startup failure are listed below:

- The vapor pressure never decreased below the critical pressure of the nitrogen due to inaccuracy of the working fluid mass weight and temperature measurement;

- The lowest temperature reached by the condenser was 116 K after 3 hours of testing. This small saturation level provides a saturated liquid with a small latent heat, which makes it very sensitive to parasitic heat loads;

- With increased vacuum level, contact resistance effects between the brass sleeves and the calorimeter provided less cooling capacity of the experimental apparatus.
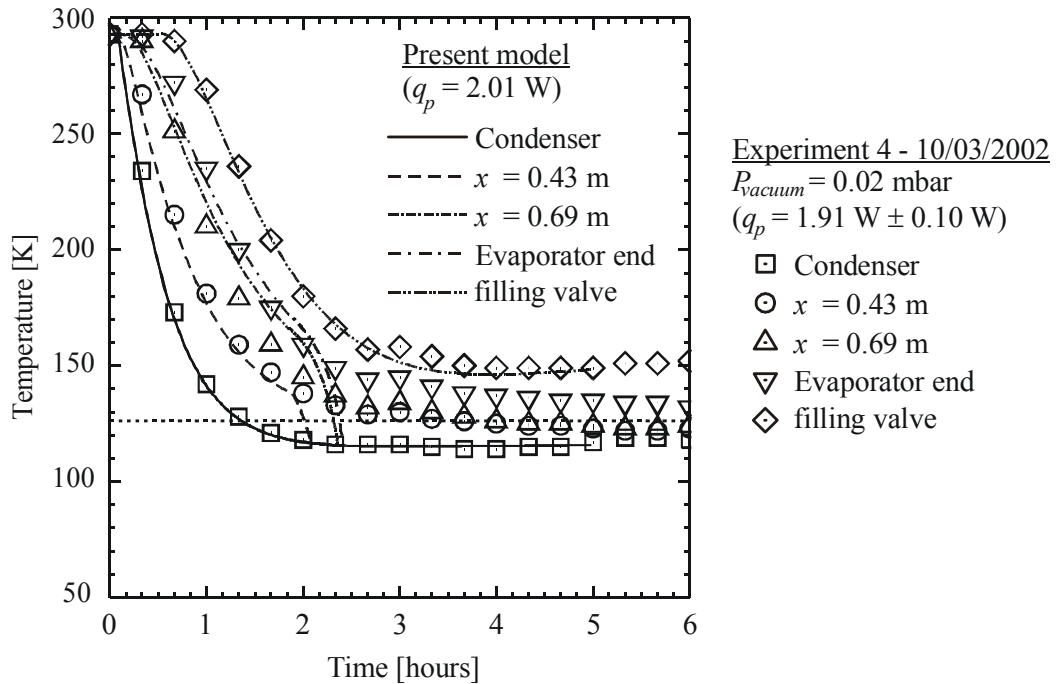

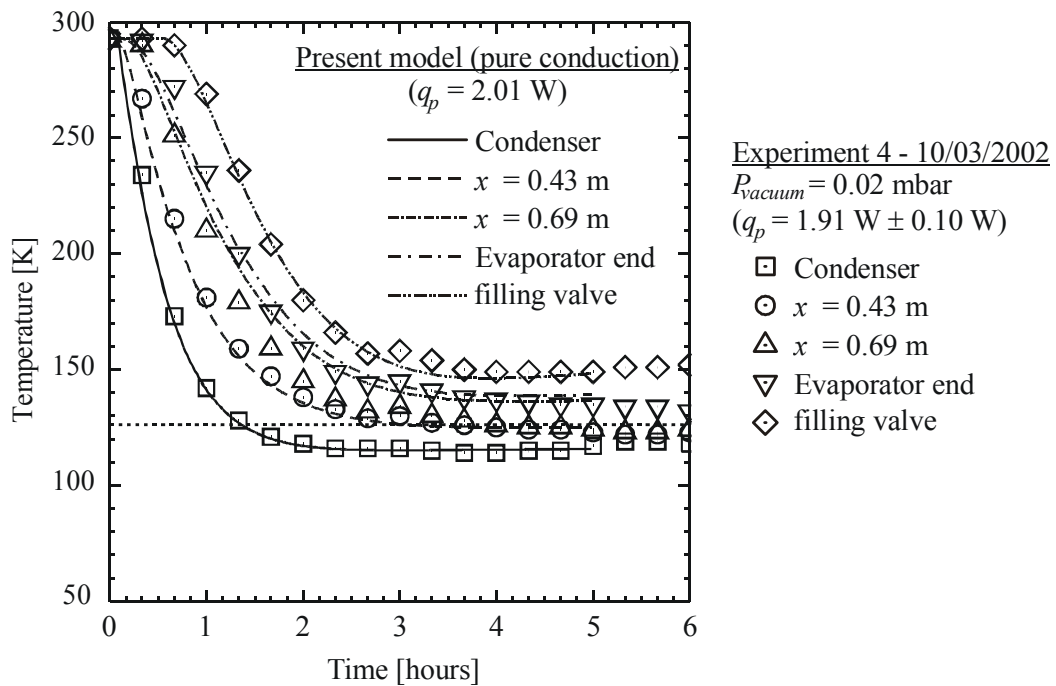Figure 5.14. CryoNHP fourth test (10/03/2002) – Transient cool-down.

Figure 5.15. CryoNHP fourth test (10/03/2002) – Pure conduction cool-down.

The last statement can be verified as follows: the pressure inside the vacuum chamber during this supercritical startup experiment was 2×10^{-2} mbar, or 100 times lower than the pressure of the first experiments. In this rarefied atmosphere any effect of convection over the heat pipe startup can be neglected. With low vacuum level on the first tests, the atmosphere inside the vacuum chamber was cooled by the calorimeter, which has a large thermal mass, improving the heat transfer from the calorimeter to the sleeve, and to the heat pipe condenser.

To check this explanation, the rotary pump of the vacuum chamber was turned off after the non-operational condition was achieved. The pressure in the vacuum chamber increased quickly to 6×10^{-2} mbar in less than one minute, to 2×10^{-1} mbar in five minutes, and to 1 mbar after 15 minutes remaining stable around this value for one hour. The temperature profiles of the heat pipe for this test are shown at Fig. 14. It can be observed that the local temperatures of the heat pipe decreased after the shut down of the rotary pump due to improved convection inside the vacuum chamber. At cryogenic levels of temperature, the heat pipe is very sensitive to small heat loads, even those provided by a rarefied atmosphere.
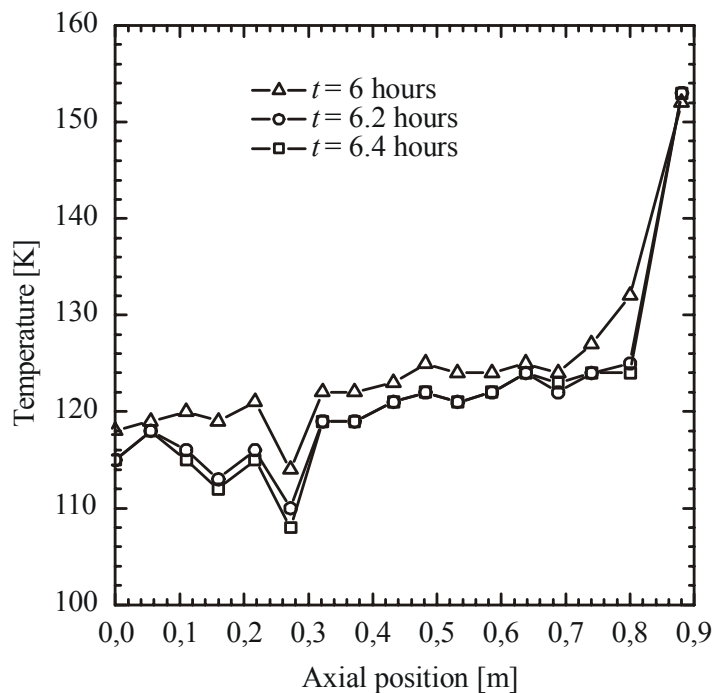
Figure 5.16. CryoNHP fourth test (10/03/2002) – Temperature profiles after rotary pump shut down.

Experiment 5: October 4th, 2002:

A 5th test followed the 4th experiment, on the October 4th 2002, with the same setup. The same startup failure was observed showing that the calorimeter was not able to provide enough cooling to the condenser regions of the heat pipe. Figure 5.17 presents the transient

temperatures measurement for different axial positions, showing a repeatability of the fourth experiment.

After the fifth test, the experimental setup was disassembled. The heat pipe was vented and a new calorimeter was designed. The new calorimeter allowed the liquid nitrogen to be in direct contact with the condenser wall of the cryogenic heat pipe, thus providing a larger cooling capacity.
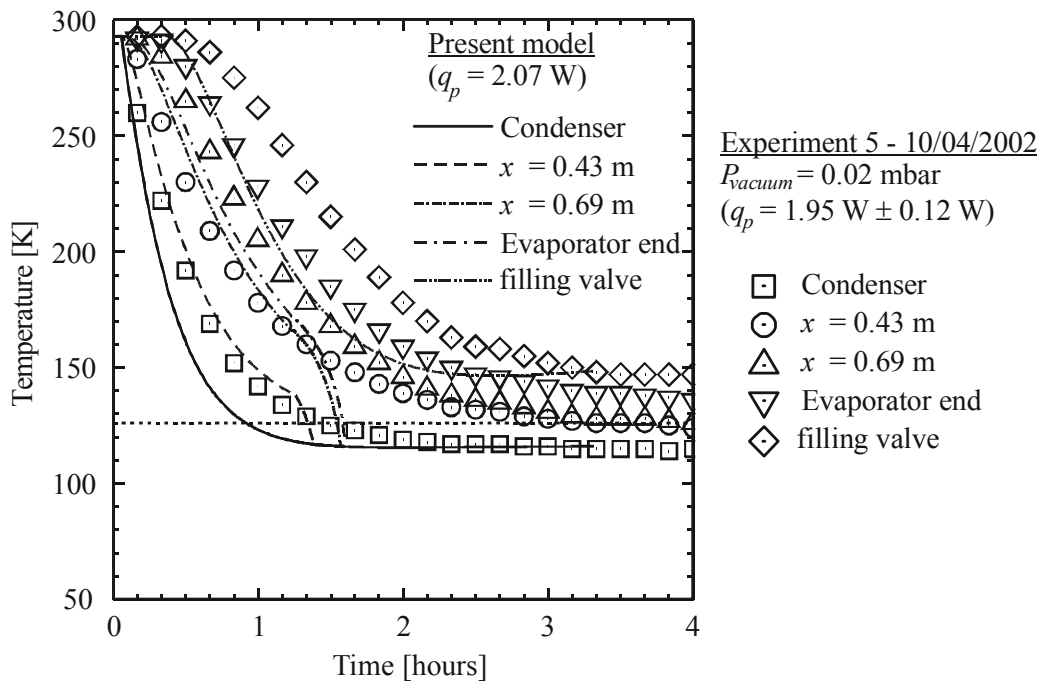

Figure 5.17. CryoNHP fifth test (10/04/2002) – Temperature profiles

Experiment 6: November 26th, 2002:

A last experiment was performed on November 26th 2002. The new calorimeter was used in this experiment. The new calorimeter provided enough cooling to the heat pipe and an "almost" successful startup was obtained, with 97% of the total length primed by the liquid column. The heat pipe did not prime completely because there was still a parasitic heat load incoming from the filling valve. However, the calorimeter imposed an abrupt cooling of the condenser, producing a fast transient: according to the experiment the heat pipe was primed (97% of the total length) in less than 15 minutes (it means a variation of 14 K per second at the condenser section, and a 0.2 K per second at the evaporator end). The numerical solution of the model was not able to reproduce this fast transient due to the large temperature gradient at the leading edge of the liquid column caused by the abrupt cooling of the condenser region. As the temperature of the condenser decreased quickly, the theoretical average liquid column velocity was large, which in turn, provided a long liquid column length. The long length obtained produced a large temperature gradient at the liquid column interface, which pushed

back the liquid column edge, causing the iterative process to diverge. Several time steps as small as 0.1 sec. were tried, but the model took almost 1 minute (to solve this small time step) before the divergence to occur. Therefore, no comparison between theoretical and experimental data was possible for this experiment.

Figure 5.18 shows the transient cool-down experimental data for the sixth test. The condenser region was cooled to the critical temperature of the nitrogen in less than 3 minutes, and the cooling effect spread over the heat pipe in less than 15 minutes. The heat pipe reached a steady state after 45 minutes of testing, with the condenser region in a temperature around 80 K, and the remaining length at 108 K. The filling valve was at 125 K..
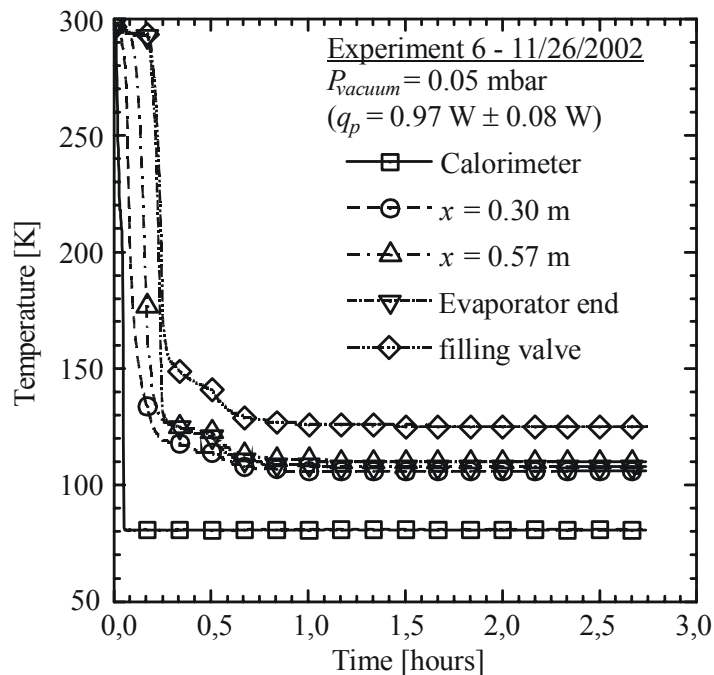

Figure 5.18. CryoNHP sixth test (26/11/2002) – Transient cool-down.

5.3 Summary and Conclusions

The experimental data of the proposed nitrogen/ stainless steel cryogenic heat pipe was shown in this chapter. Six experiments were performed during the year of 2002, and the results provided a good insight on the cryogenic heat pipe supercritical startup. Also, theoretical data was compared to experimental data when possible. The comparison showed that the startup for ground tests was faster than those predicted with the model because of the effects of body forces on the condensed liquid column. In the other hand, theoretical data seems to be in good agreement with steady state experimental data and the network thermal model seems to be appropriate for the parasitic heat load estimation. However the numerical solution of the thermal model presented in Section 4 could not reproduce a fast transient as observed in the

experiment 6. These tests showed that the model is able to predict the startup behavior of cryogenic heat pipes even in adverse situations, excluding a fast startup. They also showed that LABSOLAR/NCTS is able to design and construct successfully cryogenic heat pipes.

5.4 Synopsis

Dados experimentais do tubo de calor de nitrogênio/aço inox proposto foram mostrados neste capítulo. Seis experimentos foram realizados entre Abril e Novembro de 2002, e os resultados forneceram uma boa compreensão do processo de partida de tubos de calor criogênicos. Dados teóricos foram comparados a dados experimentais sempre que possível. Os dados teóricos apresentam boa concordância com dados experimentais e o modelo de resistências térmicas parece ser apropriado para a estimação de cargas térmicas parasitas. Porém, o modelo térmico descrito na Seção 4 não pôde reproduzir o rápido transiente observado no sexto experimento.

<div align="right">

Chapter 6
Conclusions

</div>

A theoretical and experimental analysis of the supercritical startup of cryogenic heat pipes was presented. The analysis focused the investigation of the effects of the parasitic heat loads on the supercritical startup, but effects of fluid charge and cooling rate of the condenser were also observed. The literature review described in Chapter 2 provided good information regarding the startup of cryogenic heat pipes but it also showed the lack of data regarding its startup limits.

A theoretical model was developed and successfully implemented. The startup was modeled taking into account the effects of the parasitic heat loads, vapor pressure, and fluid charge, which provided good information about the supercritical startup phenomena. The model also accounted for variation of the thermophysical properties with the temperature. The equations used in the modeling were numerically solved using finite volume technique. Numerical methods were used due to the non-linearity of the parasitic heat load term. The theoretical data was compared to three sets of microgravity flight experiments. The theoretical results were in good agreement with the experiments for microgravity environment.

The experimental setup built for ground test was fully described at Chapter 4 and showed to be adequate for heat pipe testing. A nitrogen/stainless steel screen wick cryogenic heat pipe designed and built at LABSOLAR/NCTS underwent six experiments with different fluid charges and parasitic heat load levels. Theoretical data was compared to the experimental results and it was shown that the model predicted a slower startup. This is because the model did not include the effects of the gravitational forces existing in ground tests. The model, developed for microgravity conditions, considers that any excess of condensed working fluid is accumulated in the condenser region end as a liquid slug. In ground tests, the capillary forces cannot support a liquid slug across the vapor diameter and

the excess of liquid spreads as a puddle and facilitates the priming of the heat pipe (Brennan *et al.* 1993).

The experimental and theoretical data provided a good insight of the supercritical startup of cryogenic heat pipes and some conclusions are listed below:

1. Cryogenic heat pipes are very sensitive to parasitic heat loads. The rewetting process is driven by the average condensed liquid velocity and it is controlled by the conducted heat flux from the dry region of the heat pipe. The parasitic heat loads increase the temperature gradient in the dry region, increasing the vaporization of fluid at the leading edge of the liquid column. Also, parasitic heat loads vaporize the fluid along the liquid column edge, decreasing the average liquid velocity. These two effects combined decrease the liquid column momentum, and the rewetting process may stagnate before the heat pipe is fully primed for relatively large parasitic heat loads. Additionally, parasitic heat loads may add loads to the heat pipe on the order of the maximum transport capability.

2. As cryogenic working fluids usually exhibits very low values of surface tension and latent heat of vaporization, resulting in low heat transport capacity heat pipes, even a small amount of parasitic heat load is able to vaporize cryogenic working fluids.

3. An excess of fluid charge will cause an increase of the vapor pressure of the heat pipe. Depending on the combination of parasitic heat loads and excess of fluid charge, the vapor pressure may never decrease below the critical pressure of the working fluid, even if the condenser is at a temperature below the critical point.

4. A deficiency of working fluid will decrease the vapor pressure during startup, but total amount of working fluid may not be enough to prime completely the heat pipe.

5. A fast cooling rate of the condenser will cause a large temperature gradient on the dry region of the heat pipe. This will push a large amount of working fluid to the condenser region, which will turn into subcooled liquid before condensation begins. As the heat pipe continues to cool down, the subcooled liquid will turn into saturated fluid at a temperature far below the critical point, which will produce a liquid column with a considerably large momentum, facilitating the priming of the heat pipe. A fast cooling rate may be considered for ground tests when a successful startup is required for heat transport tests of cryogenic heat pipes.

6. The pressure data considered during the development of this work was obtained by calculations using the theoretical data provided by the thermal model, which was

developed for microgravity environment. Experimental data of the vapor pressure
of cryogenic heat pipes during the supercritical startup may be required for a better
understating of the startup process in ground tests. Also vapor temperature during
the startup would provide a good insight of the vapor thermodynamics during the
startup. The experimental data of the vapor pressure and temperature consist in
invaluable insight of the supercritical startup of cryogenic heat pipes and it may be
a good subject for future investigations.

6.1 Synopsis

*Uma análise teórica e experimental da partida supercritica de tubos de calor
criogênicos foi apresentada. A análise focalizou a investigação dos efeitos da carga térmica
parasita sobre a partida, mas efeitos de carga de fluido de trabalho, e taxa de resfriamento
do condensador também foram observados. A revisão bibliográfica descrita no Capítulo 3
forneceu boas informações relativas a partida de tubos de calor criogênicos, mas também
mostrou a falta de dados que no que se refere aos limites de partida.*

*Um modelo teórico foi desenvolvido e implementado com sucesso. O modelo teórico
considerou os efeitos da carga térmica parasita, pressão de vapor, e carga de fluido de
trabalho que por sua vez permitiram o entendimento do fenômeno da partida supercrítica de
tubos de calor criogênicos. O modelo também considerou propriedades termofísicas
variáveis com a temperatura. As equações do modelo foram resolvidas numericamente
utilizando-se a técnica dos volumes finitos. O método numérico foi utilizado devido a não
linearidade produzida pelo termo da carga térmica parasita. Dados teóricos foram
comparados a três conjuntos de dados experimentais obtidos em testes em ambiente de
microgravidade disponíveis na literatura. Os resultados teóricos mostraram boa
concordância com os dados experimentais.*

*O aparato experimental construído para teste no laboratório foi descrito em detalhes
no Capítulo 4 e se mostrou adequado para testes de tubo de calor. Um tubo de calor
criogênico de aço inox e nitrogênio como fluido de trabalho e estrutura capilar composta por
telas metálicas de aço inox projetado e construído no LABSOLAR/NCTS passou por seis
experimentos com diferentes cargas de fluido de trabalho e diferentes níveis de carga térmica
parasitas. Dados teóricos foram comparados aos resultados experimentais, e a comparação
foi favorável e as tendências observadas foram captadas pelo modelo. Porém, os resultados
teóricos superestimam os dados experimentais durante a fase transiente da partida. Isto se
deve ao fato de que o modelo não incluiu os efeitos das forças gravitacionais que existem em*

testes laboratoriais. O modelo, desenvolvido para condições de microgravidade, considera que qualquer excesso de fluido de trabalho condensado é acumulado na extremidade do condensador como um pistão líquido. Em testes de laboratório, as forças capilares não conseguem suportar este pistão líquido na região de vapor e o excesso de líquido se espalha pela estrutura capilar formando uma poça e facilitando o molhamento da estrutura capilar do tubo de calor (Brennan et al. 1993).

Os dados experimentais e teóricos forneceram uma boa compreensão sobre a partida supercrítica de tubos de calor criogênicos e algumas conclusões são listadas a seguir:

1. *Tubos de calor criogênicos são extremamente sensíveis a cargas térmicas parasitas. O processo de molhamento da estrutura capilar é conduzido pela velocidade média do líquido condensado e é controlado pelo fluxo de calor proveniente da região seca do tubo de calor. As cargas térmicas parasitas aumentam o gradiente térmico na região seca, aumentando a vaporização de fluido na extremidade da coluna de líquido. Adicionalmente, cargas térmicas parasitas vaporizam o fluido ao longo do comprimento da coluna líquida, o que diminui a sua velocidade média. Estes dois efeitos combinados diminuem a quantidade de movimento da coluna líquida, e o processo de molhamento pode estagnar antes do final do tubo de calor. Adicionalmente, cargas térmicas parasitas podem ser da ordem da máxima capacidade de transporte de calor do tubo.*

2. *Como fluidos de trabalho criogênicos normalmente possuem baixos valores de tensão superficial e calor latente de vaporização, sua utilização em tubos de calor pode resultar em um dispositivo com baixa capacidade de transporte de calor, de forma que até mesmo uma pequena carga térmica parasita pode vaporizar o fluido de trabalho na estrutura capilar.*

3. *Um excesso de carga de fluido de trabalho causará um aumento da pressão de vapor no tubo de calor. Dependendo da combinação de cargas térmicas parasitas e excesso de carga de fluido, a pressão de vapor pode nunca atingir valores abaixo da pressão crítica do fluido de trabalho, até mesmo se o condensador estiver a uma temperatura abaixo do ponto crítico.*

4. *Uma deficiência de fluido de trabalho diminuirá a pressão de vapor durante a partida, mas a massa total de fluido de trabalho pode não ser suficiente para o molhamento completo do tubo de calor.*

5. *Uma taxa de resfriamento rápida do condensador causará um grande gradiente térmico na região seca do tubo de calor. Isto fará com que mais fluido de trabalho*

seja empurrado para a região do condensador, que se transformará em líquido sub-resfriado antes que a condensação comece. Como o tubo de calor continua resfriando, o líquido sub-resfriado se transformará em fluido saturado a uma temperatura bem abaixo do ponto crítico, o que produzirá uma coluna líquida com uma quantidade de movimento consideravelmente grande, facilitando a partida do tubo de calor. Uma taxa de resfriamento rápida pode ser considerada para testes de laboratório quando uma partida rápida é requerida para testes de capacidade de transporte de calor de tubos de calor criogênicos.

6. *Os dados de pressão considerados durante o desenvolvimento deste trabalho foram obtidos por cálculos baseados em dados teóricos de temperatura fornecidos pelo modelo térmico, que foi desenvolvido para ambiente de microgravidade. Dados experimentais da pressão de vapor em tubos de calor criogênicos durante o processo de partida supercrítica podem ser necessários para uma melhor compreensão da partida em testes de laboratório. Também, a temperatura do vapor forneceria boas informações da termodinâmica do vapor durante a partida supercrítica. Os dados experimentais da pressão e temperatura de vapor são dados de valor inestimável para o entendimento do processo físico da partida supercritica de tubos de calor criogênicos e pode ser um assunto para investigações futuras.*

References

ABROSIMOV, A.; BARYSHEV, O.; HORONENKO, V.; KOSOROTOV, M.; LOBANOV, A. and PARFENTIEV. M. Diode Cryogenic Heat Pipe for SODART Telescope Silicon Detector Cooling. In: 8th INTERNATIONAL HEAT PIPE CONFERENCE, 1992, Beijing, China. **Proceedings…**, pp. E-P54/1 – E-P54/4.

AGÊNCIA ESPECIAL BRASILEIRA. Plano Nacional de Atividades Espaciais – PNAE (*Brazilian Space Agency. Brazilian Policy for Space Activities – PNAE*). Brasilia DF, Brazil: Published by AEB, 1996. Original in Portuguese.

ALARIO, J.; KOSSON, R. and McCREIGHT, C. A Re-entrant Groove Hydrogen Heat Pipe. In: 3rd INTERNATIONAL HEAT PIPE CONFERENCE, May 1978, Palo Alto, CA. **Proceedings…**, pp. 194 – 202.

BARANTSEVICH, V. L. and GUTKIN, A. R. The Application of Heat Pipes for Microcryogenic System Thermal Control. In: 8th INTERNATIONAL HEAT PIPE CONFERENCE, 1992, Beijing, China. **Proceedings…**, pp. E-P55/1 – E-P55/5.

BARRON, R. F. **Cryogenic Systems**. 2nd Edition, New York, NY: Oxford University Press, 1985, pp. 3 – 55.

BEJAN, A. **Convection Heat Transfer**. 2nd Edition, New York, NY: John Wiley & Sons, Inc., 1995, pp. 106.

BOWMAN, W. J. Numerical Modeling of Heat Pipe Transients. **Journal of Thermophysics**, Jul./Sep. 1991, Vol. 5, no. 3, pp. 374 – 379.

BRANDT, O. and SCHLITT, R. Low Temperature Radiator Design for the Abrixas X-Ray Satellite. In: 6th EUROPEAN SYMPOSIUM ON SPACE ENVIRONMENTAL CONTROL SYSTEMS, May 1997, Noordwijk, The Netherlands. **Report ESA SP-400**, Aug. 1997, pp. 151 – 159.

BRENNAN, P. J.; THIENEN, L.; SWANSON, T. and MORGAN, M. Flight Data for the Cryogenic Heat Pipes (CRYOHP) Experiment. In: 28th AIAA THERMOPHYSICS CONFERENCE, Orlando, FL, Jul. 1993. AIAA Paper No. 93-2735, 10 pp.

CHANG, W. S. and COLWELL, G. T. Mathematical Modeling of the Transient Operating Characteristics of a Low-Temperature Heat Pipe, **Numerical Heat Transfer**, 1985, Vol. 8, pp. 169 – 186.

CHI, S. W. and CYGNAROWICZ, T. A. Theoretical Analyses of Cryogenic Heat Pipes. In: SPACE TECHNOLOGY AND HEAT TRANSFER CONFERENCE, Jun. 1970, Los Angeles, CA. **ASME PAPER 70-HT/SpT-6**.

COLWELL, G. T. Prediction of Cryogenic Heat Pipe Performance. **NASA Final Report NSG-2054**, Mar. 1977.

COLWELL, G. T. and CHANG, W. S. Measurements of the Transient Behavior of a Capillary Structure Under Heavy Thermal Loading. **International Journal of Heat and Mass Transfer**, 1983, Vol. 27, no. 4, pp.541 – 551.

COUTO, P. **Development and Design of Passives Cryogenic Radiators for Spacecraft Applications**. Jul. 1999, 156 pp. Thesis (M.Sc. in Mechanical Engineering), Mechanical Engineering Department, Federal University of Santa Catarina, Florianópolis, Brazil (original version in Portuguese).

COUTO, P.; OCHTERBECK, J. M. and MANTELLI, M. B. H. Analysis of Supercritical Start-up Limitations for Cryogenic Heat Pipes with Parasitic Heat Loads. In: 8th AIAA/ASME JOINT THERMOPHYSICS AND HEAT TRANSFER CONFERENCE, Jun. 2002, St. Louis, MI. **AIAA Paper No. 2002-3095**, 11 pp.

EDELSTEIN, F. and KOSSON, R. A High Capacity Re-entrant Groove Heat Pipe for Cryogenic and Room Temperature Space Applications. **Cryogenics**, 1992, Vol. 32, No. 2, pp. 167 – 172.

FAGHRI, A. **Heat Pipe Science and Technology**. 1st Edition, Washington DC: Taylor and Francis, 1995.

FISHER, W. D. Thermal Control Subsystem Technology Projection. In: INTRODUCTION TO SATELLITE THERMAL CONTROL, AIAA Professional Development Short Course, Jun. 1998, Albuquerque, NM.

GILMORE, D. G. "**Satellite Thermal Control Handbook**". 1st Edition, El Segundo, CA: The Aerospace Corporation Press, 1994.

GROLL, M.; RÖSTER, S. and SUPPER, W. Experimental Investigation of a Cryogenic Methane Heat Pipe Diode. In: 16th INTERSOCIETY CONFERENCE ON ENVIRONMENTAL SYSTEMS, San Diego, CA, Jul. 1986. **Proceedings…**, pp. 341 – 348.

GROLL, M.; SCHNEIDER, M.; SARTRE, V.; ZAGHDOUDI, M. C. and LALLEMAND, M. Thermal control of electronic equipment by heat pipes. **Revue Generale de Thermique**, May, 1998, Vol. 37, No. 5, pp. 323 – 352.

HAMILTON, A. and HU, J. An Electronic Cryoprobe for Cryosurgery Using Heat Pipes and Thermoelectric Coolers - A Preliminary Report. **Journal of Medical Engineering and Technology**, May/Jun. 1993, Vol. 17, No. 3, pp. 104 – 109.

HASKINS, W. L. Cryogenic Heat Pipe. **Report No. AFFDL-TR-66-228**, Jun. 1966, Wrigth-Paterson Air Force Base, Dayton, OH.

HOLMAN, J. P., **Experimental Methods for Engineers**, 6th Edition, McGraw-Hill, Singapore, pp. 49-103, 1994.

IMURA, H.; KOZAI, H.; HAYASHIDA, S. and TAKASHIMA, K. Heat Transfer Characteristics in Screen-wick Heat Pipes. **JSME International Journal – Series II**, 1988, Vol. 31, No. 1, pp. 88 – 97.

IMURA, H.; KOZAI, H. and IKEDA, Y. The Effective Pore Radius of Screen Wicks. **Heat Transfer Engineering**, 1994, Vol. 15, No. 4, pp. 24 – 32.

ISHIGOHKA, T.; HIRAYAMA, Y.; NINOMIYA, A. and S. MAEZAWA. Conduction Cooling of High-TC Superconducting Magnet Using Heat Pipe. In: 11th INTERNATIONAL HEAT PIPE CONFERENCE, Sep. 1999, Tokyo, Japan. **Proceedings…**, pp. 139 – 144.

JACOBSEN, R. T.; PENONCELLO, S. G. and LEMMON, E. W. **Thermodynamic Properties of Cryogenic Fluids**, 1st Edition, New York, NY: Plenum Press, 1997.

JACOBSEN, R. T.; STEWART, R. B. and JAHANGIRI, M. Thermodynamic Properties of Nitrogen from the Freezing Line to 2000 K at Pressures to 1000 MPa. **Journal of Physical and Chemical Reference Data**, 1986, Vol. 15, No. 2, pp. 735 – 909.

JOY, P. Optimum Cryogenic Heat Pipe Design. In: SPACE TECHNOLOGY AND HEAT TRANSFER CONFERENCE, Jun. 1970, Los Angeles, CA. **ASME PAPER 70-HT/SpT-7**, 8 pp.

NAKANO, A.; SHIRAISHI, M.; NISHIO, M. and MURAKAMI, M. An Experimental Study of Heat Transfer Characteristics of a Two-phase Nitrogen Thermosyphon Over a Large Dynamic Range Operation. **Cryogenics**, 1998, Vol. 38, No. 12, pp. 1259 – 1266.

NIELD, D. A. and BEJAN, A. **Convection in Porous Media**, 1st Edition, New York, NY: Springer-Verlag NY Inc., 1992, pp. 1 – 28.

OCHTERBECK, J. M.; PETERSON, G. P. and UNGAR, E. K. Depriming/Rewetting of Arterial Heat Pipes: Comparison with Share-II Flight Experiment. **AIAA Journal of Thermophysics and Heat Transfer**, Jan./Mar. 1995, Vol. 9, No. 1, pp. 101 – 108.

PATANKAR, S. V. **Numerical Heat transfer and Fluid Flow**, Washington DC: Hemisphere Pub. Corp., 1980.

PETERSON, G. P. **An Introduction to Heat Pipes – Modeling, Testing and Applications**. 1st Edition, New York, NY: John Wiley and Sons, Inc., 1991.

PETERSON, G. P. and COMPAGNA, G. L. Review of Cryogenic Heat Pipes. **AIAA Journal of Spacecraft**, Mar./Apr. 1987, Vol. 24, No. 2.

ROSENFELD, J. H.; BUCHKO, M. T. and BRENNAN, P. J. A Supercritical Start-Up Limit to Cryogenic Heat Pipes in Microgravity. In: 9th INTERNATIONAL HEAT PIPE CONFERENCE, Albuquerque, NM, 1995. **Proceedings…**, Vol. 2, pp. 742 − 753.

RÖSTER, S.; GROLL, M.; SUPPER, W. and KONEV, S. Analysis and Experimental Investigation of a Cryogenic Methane Heat Pipe. In: 6th INTERNATIONAL HEAT PIPE CONFERENCE, Grenoble, France, May 1987. **Proceedings…**, pp. 352 − 355.

SCHMIDT, R and WAGNER, W. A New Form of the Equation of State for Pure Substances and its Application to Oxygen. **Fluid Phase Equilibria**, 1985, Vol. 19, pp. 175 − 200.

STEWART, R. B.; JACOBSEN, R. T. and WAGNER, W. Thermodynamic Properties of Oxygen from the Triple Point to 300 K with Pressures to 80 MPa. **Journal of Physical and Chemical Reference Data**, 1991, Vol. 20, No. 5, pp. 917-1021.

TIMMERHAUS, K. D. and FLYNN, T. M. Safety with Cryogenic Systems. **Advances in Cryogenic Engineering**, 1978, 1st. Ed., Vol. 23, Editor: K. D. Timmerhaus, Plenum Press, New York, pp. 721 − 729.

TOURNIER, J.-M. and EL-GENK, M. S. A Heat Pipe Transient Analysis Model. **International Journal of Heat and Mass Transfer**, 1994, Vol. 37, No. 5, pp. 753 − 762.

TOURNIER, J.-M. and EL-GENK, M. S. Segregated Solution Technique for Simulating the Transient Operation of Heat Pipes. **Numerical Heat Transfer, Part B**, 1994, Vol. 25, pp. 331 − 355.

VAN OOST, S. and AALDERS, B. Cryogenic Heat Pipe Ageing, In: 10th International Heat Pipe Conference, Stuttgart, Germany, Sep. 1997. **Proceedings…**, pp. J-6/1 − J-6/6.

VAN WYLEN, G. J. and SONNTAG, R. E. **Fundamentals of Classical Thermo-dynamics**, John Wiley & Sons, Inc., 1973.

VOYER, E.; MOSCHETTI, B.; BRIET, R.; ALET, I. and EVIN, R. Heat Pipes for Cryogenic Applications on Satellites. In: 27th INTERNATIONAL CONFERENCE ON ENVIRONMENTAL SYSTEMS, Lake Tahoe, Nevada, Jul. 1997. **SAE Technical Paper No. 972450**, 10 pp.

WRIGHT, J. P. Development of a 5 W 70 K Passive Radiator. In: 15th AIAA THERMOPHYSICS CONFERENCE, Snowmass, Colorado, Jul. 1980. **AIAA Paper No. 80-1512**, 10 pp.

WRIGHT, J. P. and PENCE, W. R. Development of a Cryogenic Heat Pipe Radiator for a Detector Cooling System, In: SAE-ASME-AIAA-ASMA-AIChE INTERSOCIETY CONFERENCE ON ENVIRONMENTAL SYSTEMS, San Diego, California, Jul. 1973. **ASME Paper No. 73-ENAs-47**, 10 pp.

YAN, Y. H. and OCHTERBECK, J. M. Integral Method Solution for Rewetting of Finite Length Surfaces with Uniform Heating. In: 1996 NATIONAL HEAT TRANSFER CONFERENCE, Aug. 1996, Houston, TX, USA, **AIAA Paper No. 96-3975**, 8 pp.

YAN, Y. H. and OCHTERBECK, J. M. Analysis of Supercritical Start-Up Behavior for Cryogenic Heat Pipes, **AIAA Journal of Thermophysics and Heat Transfer**, Jan./Mar. 1999, Vol. 13, No. 1, pp. 140 – 145.

ZELENOV, I. A.; POSKONIN, U. A.; TIMOFEEV, V. N.; KOSTENKO, V. I.; RIBKIN, B. I.; ROMANOVSKY, O. I.; SIDORENKO, E. M. and GUSKOV, A. S. Flexible Low Temperature and Cryogenic Heat Pipes for the Space Controlled Radiator-Emitter. In: 8th INTERNATIONAL HEAT PIPE CONFERENCE, Beijing, China, 1992. **Proceedings…**, pp. E-P66/1 – E-P66/4.

ZUO, Z. J. and FAGHRI, A. A Network Thermodynamic Analysis of the Heat Pipe. **International Journal of Heat and Mass Transfer**, 1998, Vol. 41, No. 11, pp. 1473 – 1484.

Appendixes

Appendix A
List of Parameters

In this appendix, all the parameters used in this work, except the thermophysical properties, are summarized. The thermophysical properties are shown in the Appendix B.

TRW and HAC Heat Pipes' Design Summary (Brennan *et al.* 1993)

Design Parameter	TRW	HAC
Tube material:	Aluminum Alloy, 2024-T6	
Tube dimensions:		
Outer diameter	11.2 mm	15.91 mm
Vapor diameter	7.37 mm	8.64 mm
Wall thickness	1.02 mm	2.54 mm
Lengths:		
Evaporator	0.15 m	0.15 m
Condenser	0.15 m	0.15 m
Transport section	1.02 m	1.07 m
Oxygen charge	10.3 g	33.7 g
Number of Grooves	17	27
Groove width	0.445 mm	0.658 mm
Fin Fip Radius	0.102 mm	0.16 mm
Wetted Perimeter (1 Groove)	2.09 mm	3.25 mm
Total Groove Area	6.07 mm^2	23.2 mm^2

Estimated values for $\varepsilon F_{HP,\infty}$.

q_p	Heat Pipe	$\varepsilon F_{HP,\infty}$
1.10 Watt	TRW	0.077
1.50 Watt	TRW	0.104
1.90 Watt	TRW	0.134
1.48 Watt	NHP	0.114
1.14 Watt	HAC	0.056

NHP Design Summary (Rosenfeld *et al.* 1995)

Design Parameter	NHP
Tube material:	Titanium Alloy, Ti-6Al-4V
Tube dimensions:	
Outer diameter	15.0 mm
Wall thickness	1.026 mm
Lengths:	
Evaporator	0.127 m
Condenser	0.178 m
Transport section	0.613 m
Nitrogen charge	24.1 g
Number of metal cables	6
Cable material	Fibrous copper
Cable diameter	3.20 mm
Porosity	0.520 to 0.895
Permeability $\times 10^{10}$	0.009 to 12.4

Metal screen wick geometry.

Mesh	No. of Layers	Material	Wire spacing	Wire diameter	Thickness	Porosity	Permeability	Effective capillary radius
160	1	AISI 316 Stainless steel	0.090 mm	0.070 mm	0.225 mm	0.671	2.67×10^{-10} m^2	0.08 mm
	2				0.430 mm	0.656	2.27×10^{-10} m^2	
	4				0.812 mm	0.635	1.84×10^{-10} m^2	
	8				1.676 mm	0.647	2.07×10^{-10} m^2	
254	1	AISI 304 Stainless steel	0.060 mm	0.040 mm	0.137 mm	0.734	1.18×10^{-10} m^2	0.05 mm
	2				0.341 mm	0.786	2.24×10^{-10} m^2	
	4				0.502 mm	0.710	0.89×10^{-10} m^2	
	8				1.000 mm	0.708	0.88×10^{-10} m^2	

Nitrogen/stainless steel cryogenic heat pipe design summary.

Tube material:	AISI 304 Stainless Steel
Tube dimensions:	
Outer diameter	19.05 mm (3/4")
Wall thickness	1.3 mm
Lengths:	
Evaporator	0.30 m
Condenser	0.30 m
Transport section	0.20 m
Nitrogen charge:	31.1 g
Vapor pressure:	
At 300 K	19.8 MPa
At 77.4 K	0.1 MPa
Maximum heat transport capacity (temperature)	2.2 W.m (82 K)
Wick structure:	Metal screen
Mesh	160
Number of layers	8
Thickness	1.676 mm

Appendix B
Thermophysical Properties of Nitrogen and Oxygen

The fundamental equation described in this appendix is a general form used for the calculation of thermophysical properties of a large number of fluids. However, this explanation will focus on Oxygen and Nitrogen.

The Fundamental Equation

The fundamental equation by Schmidt and Wagner (1985), Stewart *et al.* (1991), and Jacobsen *et al.* (1986 and 1997) are explicit in reduced Helmholtz energy. The Helmholtz energy is given by:

$$A(\rho,T) = A^{\circ}(\rho,T) + \overline{A}(\rho,T) \tag{B.1}$$

where $A^{\circ}(\rho,\ T)$ is the ideal gas contribution to the Helmholtz energy and the term $\overline{A}(\rho,T)$ represents the contribution related to the compressibility of the fluid. The pressure derived from this expression is obtained from:

$$P = \rho^{2}\left(\frac{\partial A}{\partial \rho}\right)_{T} \tag{B.2}$$

The Helmholtz energy for the ideal gas is given by:

$$A^{\circ} = U^{\circ} - TS^{\circ} = H^{\circ} - RT - TS^{\circ} \tag{B.3}$$

Combining expressions for the ideal gas enthalpy and entropy, the Helmholtz energy for the ideal gas is given by:

$$A^{\circ}(\rho,T) = H_0^{\circ} + \int_{T_0}^{T} C_p^{\circ} dT - RT - T\left[S_0^{\circ} + \int_{T_0}^{T} \frac{C_p^{\circ}}{T} dT - R\ln\left(\frac{\rho T}{\rho_0 T_0}\right) \right] \tag{B.4}$$

where H_0° and S_0° are reference values for the enthalpy and entropy, respectively, obtained at T_0 and P_0. An equation for the ideal gas heat capacity (C_p°) as a function of temperature must be used with Eq. (B.4) to develop the complete expression for a specific fluid. This equation will be shown later.

Practical equations of state generally use reduced variables to simplify computer calculations. Generally, properties are reduced by accepted critical state values or other combinations of properties and constants to make the equations non-dimensional. The non-dimensional variables used for the derivation of the fundamental equation are:

$$\alpha = \frac{A}{RT}; \ \delta = \frac{\rho}{\rho_{crit}}; \text{ and } \tau = \frac{T_{crit}}{T} \tag{B.5}$$

where α is the reduced Helmholtz energy, δ is the reduced density and τ is the reduced temperature. Using these variables, Eq. (B.1) can be rewritten as:

$$\alpha(\delta,\tau) = \alpha^{\circ}(\delta,\tau) + \overline{\alpha}(\delta,\tau) \tag{B.6}$$

The ideal gas contribution to the dimensionless Helmholtz energy can be derived from Eq. (B.4), as:

$$\alpha^{\circ}(\delta,\tau) = \frac{H_0^{\circ}\tau}{RT_{crit}} - \frac{S_0^{\circ}}{R} - 1 + \ln\left(\frac{\delta\tau_0}{\delta_0\tau}\right) - \frac{\tau}{R}\int_{\tau_0}^{\tau} \frac{C_p^{\circ}}{\tau^2} d\tau + \frac{1}{R}\int_{\tau_0}^{\tau} \frac{C_p^{\circ}}{\tau} d\tau \tag{B.7}$$

The non-dimensional contribution of the compressibility of the fluid $\overline{\alpha}(\delta,\tau)$ to the dimensionless Helmholtz energy is based on theoretical and practical considerations required to represent experimental data for a fluid. The general for used by Jacobsen *et al.* (1986 and 1997) is:

$$\overline{\alpha}(\delta,\tau) = \sum_{k=1}^{K} N_k \delta^{i_k} \tau^{j_k} \exp(-\gamma_k \delta^{l_k}) \tag{B.8}$$

where the constants coefficients N_k, i_k, j_k, l_k, and γ_k are determined by a least-square fit to experimental data. The coefficients for Oxygen are presented in Tables B.1 and B.2, and for Nitrogen in Tables B.3 and B.4.

Table B.1. Coefficients and exponents for the fundamental equation of Oxygen.

k	N_k	i_k	j_k	l_k	γ_k
1	0.3983768749	1	0	0	0
2	−1.846157454	1	1.5	0	0
3	0.4183473197	1	2.5	0	0
4	2.370620711 (10^{-2})	2	−0.5	0	0
5	9.771730573 (10^{-2})	2	1.5	0	0
6	3.017891294 (10^{-2})	2	2	0	0
7	2.273353212 (10^{-2})	3	0	0	0
8	1.357254086 (10^{-2})	3	1	0	0
9	−4.052698943 (10^{-2})	3	2.5	0	0
10	5.454628515 (10^{-4})	6	0	0	0
11	5.113182277 (10^{-4})	7	2	0	0
12	2.953466883 (10^{-7})	7	5	0	0
13	−8.687645072 (10^{-5})	8	2	0	0
14	−0.2127082589	1	5	2	−1
15	8.735941958 (10^{-2})	1	6	2	−1
16	0.1275509190	2	3.5	2	−1
17	−9.067701064 (10^{-2})	2	5.5	2	−1
18	−3.540084206 (10^{-2})	3	3	2	−1
19	−3.623278059 (10^{-2})	3	7	2	−1
20	1.327699290 (10^{-2})	5	6	2	−1
21	−3.254111865 (10^{-4})	6	8.5	2	−1
22	−8.313582932 (10^{-3})	7	4	2	−1
23	2.124570559 (10^{-3})	8	6.5	2	−1
24	−8.325206232 (10^{-4})	10	5.5	2	−1
25	−2.626173276 (10^{-5})	2	22	4	−1
26	2.599581482 (10^{-3})	3	11	4	−1
27	9.984649663 (10^{-3})	3	18	4	−1
28	2.199923153 (10^{-3})	4	11	4	−1
29	−2.591350486 (10^{-2})	4	23	4	−1
30	−0.1259630848	5	17	4	−1
31	0.1478355637	5	18	4	−1
32	−1.011251078 (10^{-2})	5	23	4	−1

Table B.2. Fluid constants and Ideal gas reference state properties for Oxygen.

Molecular weight, M	31.9988 g/mol
Universal gas constant, R_g	8.31434 J/mol.K
Critical temperature, T_{crit}	154.581 K
Critical pressure, P_{crit}	5.043 MPa
Critical density, ρ_{crit}	13.63 mol/dm^3
Reference temperature, T_0	298.15 K
Reference pressure, P_0	0.101325 MPa
Reference enthalpy, H_0	8670.0 J/mol
Reference entropy, S_0	191.5 J/mol.K

Table B.3. Coefficients and exponents for the fundamental equation of Nitrogen.

k	N_k		i_k	j_k	l_k	γ_k
1	0.949954183		1	0.25	0	0
2	0.248171851		2	0.25	0	0
3	−0.204628712		3	0.25	0	0
4	−0.174842901		2	0.5	0	0
5	0.638701715		3	0.5	0	0
6	−0.527298617		3	0.75	0	0
7	−2.049741504		1	1	0	0
8	5.551383553	(10^{-2})	4	1	0	0
9	−8.191106396	(10^{-4})	6	1	0	0
10	−5.032519699	(10^{-2})	2	1	2	−1
11	0.26501108		1	1.5	0	0
12	7.311459372	(10^{-2})	2	2	0	0
13	−2.813080718	(10^{-2})	4	2	0	0
14	1.659823569	(10^{-3})	6	2	0	0
15	6.012817812	(10^{-2})	2	2	2	−1
16	−0.378544519		1	3	0	0
17	0.189529043		2	3	0	0
18	−7.001895093	(10^{-3})	4	3	0	0
19	−4.927710927	(10^{-2})	1	3	3	−1
20	6.512013679	(10^{-2})	4	4	2	−1
21	0.113812194		1	4	3	−1
22	−9.551409632	(10^{-2})	2	5	2	−1
23	2.118354140	(10^{-2})	4	6	2	−1
24	−1.100721771	(10^{-2})	2	8	4	−1
25	1.284432210	(10^{-2})	4	14	4	−1
26	−1.054474910	(10^{-2})	4	18	4	−1
27	−1.484600538	(10^{-4})	2	20	4	−1
28	−5.806483467	(10^{-3})	3	22	3	−1

Table B.4. Fluid constants and Ideal gas reference state properties for Nitrogen.

Molecular weight, M	28.0134 g/mol
Universal gas constant, R_g	8.31434 J/mol.K
Critical temperature, T_{crit}	126.193 K
Critical pressure, P_{crit}	3.3978 MPa
Critical density, ρ_{crit}	11.177 mol/dm^3
Reference temperature, T_0	298.15 K
Reference pressure, P_0	0.101325 MPa
Reference enthalpy, H_0	8670.0 J/mol
Reference entropy, S_0	191.5 J/mol.K

Thermodynamic properties from the fundamental equation

Table B.5 shows the thermodynamic property relations for the fundamental equation summarized in this appendix. The functions in this table are readily used in computer programs for the calculation of thermodynamic properties.

Table B.5. Functions for calculation of thermodynamic properties[11].

Property	Relation	
Compressibility factor	$$Z = \frac{P}{\rho RT} = 1 + \delta \left(\frac{\partial \overline{\alpha}}{\partial \delta} \right)$$	(B.9)
Pressure	$$\frac{P}{P_{crit}} = \frac{\delta}{\tau Z_{crit}} \left[1 + \delta \left(\frac{\partial \overline{\alpha}}{\partial \delta} \right) \right]$$	(B.10)
Internal energy	$$\frac{U}{RT} = \tau \left[\left(\frac{\partial \alpha^{\circ}}{\partial \tau} \right) + \left(\frac{\partial \overline{\alpha}}{\partial \tau} \right) \right]$$	(B.11)
Enthalpy	$$\frac{H}{RT} = \tau \left[\left(\frac{\partial \alpha^{\circ}}{\partial \tau} \right) + \left(\frac{\partial \overline{\alpha}}{\partial \tau} \right) \right] + \left[1 + \delta \left(\frac{\partial \overline{\alpha}}{\partial \delta} \right) \right]$$	(B.12)
Entropy	$$\frac{S}{R} = \tau \left[\left(\frac{\partial \alpha^{\circ}}{\partial \tau} \right) + \left(\frac{\partial \overline{\alpha}}{\partial \tau} \right) \right] - \alpha^{\circ} - \overline{\alpha}$$	(B.13)
Isochoric heat capacity	$$\frac{C_v}{R} = -\tau^2 \left[\left(\frac{\partial^2 \alpha^{\circ}}{\partial \tau^2} \right) + \left(\frac{\partial^2 \overline{\alpha}}{\partial \tau^2} \right) \right]$$	(B.14)
Isobaric heat capacity	$$\frac{C_p}{R} = \frac{C_v}{R} + \frac{\left[1 + \delta \left(\frac{\partial \overline{\alpha}}{\partial \delta} \right) - \delta \tau \left(\frac{\partial^2 \overline{\alpha}}{\partial \delta \partial \tau} \right) \right]^2}{\left[1 + 2\delta \left(\frac{\partial \overline{\alpha}}{\partial \delta} \right) - \delta^2 \left(\frac{\partial^2 \overline{\alpha}}{\partial \delta^2} \right) \right]}$$	(B.15)

Saturation pressure ancillary equation

The saturation pressure for a given temperature can be obtained from the following equation:

$$\ln \left(\frac{P}{P_{crit}} \right) = \frac{T_{crit}}{T} \left[\sum_{k=1}^{K} N_k \theta^{i_k} \right] \qquad (B.16)$$

where N_k and i_k are constant coefficients determined by a least-square fit to experimental data and presented in Table B.6 for Oxygen and in Table B.7 for Nitrogen, and θ is given by:

---

[11] Other properties available at Jacobsen *et al.* (1986 and 1997).

$$\theta = \left(1 - \frac{T}{T_{crit}}\right)^{1/2} \tag{B.17}$$

Table B.6. Coefficients and exponents for the vapor pressure equation for Oxygen.

k	N_k	i_k
1	−6.043938	2
2	1.175627	3
3	−0.9940860	6
4	−3.456781	14
5	3.361499	18

Table B.7. Coefficients and exponents for the vapor pressure equation for Nitrogen.

k	N_k	i_k
1	1.0	0
2	−5.072183802	2
3	0.13679907760 (10^2)	3.8
4	−0.11940021330 (10^2)	4.8
5	2.641788411	7
6	−0.378126543	11
7	0.7593697713 (10^{-1})	14

Saturated liquid density ancillary equation

The saturated liquid density is obtained from the following equation:

$$\frac{\rho_\ell}{\rho_{crit}} = 1 + \sum_{k=1}^{K} N_k \theta^{i_k} + N_{1000} \ln\left(\frac{T}{T_c}\right) \tag{B.18}$$

where N_k and i_k are constant coefficients determined by a least-square fit to experimental data and presented in Table B.8 for Oxygen and in Table B.9 for Nitrogen, and θ is given by:

$$\theta = \left(1 - \frac{T}{T_{crit}}\right)^{1/3} \tag{B.19}$$

Table B.8. Coefficients and exponents for the saturated liquid density equation for Oxygen.

k	N_k	i_k
1	1.5076780	1
2	0.85810805	2
3	0.19035504	3
1000	0.0	-

Table B.9. Coefficients and exponents for the saturated liquid density equation for Nitrogen.

k	N_k	i_k
1	1.780437699 (10^1)	2
2	1.202958313 (10^3)	4
3	−4.601087081 (10^3)	5
4	1.051265347 (10^4)	6
5	−1.188582325 (10^4)	7
6	1.740912806 (10^4)	9
7	−1.934202934 (10^4)	10
8	7.191464655 (10^3)	11
9	8.015275102 (10^{-1})	0.975
1000	1.895717510 (10^2)	-

Saturated vapor density ancillary equation

The saturated liquid density for Oxygen is obtained from the following equation:

$$\frac{\rho_v}{\rho_{crit}} = \sum_{k=1}^{K} N_k \theta^{i_k} \tag{B.20}$$

and for Nitrogen, from:

$$\frac{\rho_v}{\rho_{crit}} = 1 + \sum_{k=1}^{K} N_k \theta^{i_k} + N_{1000} \ln\left(\frac{T}{T_c}\right) \tag{B.21}$$

where, for both equations, N_k and i_k are constant coefficients determined by a least-square fit to experimental data and presented in Table B.10 for Oxygen and in Table B.11 for Nitrogen, and θ is given by:

$$\theta = \left(1 - \frac{T}{T_{crit}}\right)^{1/3} \tag{B.22}$$

Table B.10. Coefficients and exponents for the saturated vapor density equation for Oxygen.

K	N_k	i_k
1	−1.498431	1
2	−2.116826	2
3	−0.905713	3
4	−5.659990	5
5	−1.8909640 (10^1)	12
6	−5.3780774 (10^1)	27

Table B.11. Coefficients and exponents for the saturated vapor density equation for Nitrogen.

k	N_k		i_k
1	1.345167397		2
2	2.721335451	(10^1)	3
3	1.189562787	(10^2)	4
4	−2.681972897	(10^2)	5
5	3.292110413	(10^2)	6
6	−1.381052419	(10^2)	7
7	3.447426258	(10^1)	11
8	−1.592975033		0.975
1000	5.724027229	(10^1)	-

Ideal gas heat capacity ancillary equation

The ideal gas heat capacity equation is:

$$\frac{C_p^{\circ}}{R} = \sum_{k=1}^{K} N_k T^{i_k} + A_{1000} \frac{(N_{1000}/T)^2 \exp(N_{1000}/T)}{[\exp(N_{1000}/T)-1]^2} \tag{B.23}$$

where N_k and i_k are constant coefficients determined by a least-square fit to experimental data and presented in Table B.12 for Oxygen and in Table B.13 for Nitrogen.

Table B.12. Coefficients and exponents for the ideal gas heat capacity equation for Oxygen.

k	N_k		i_k	A_k
1	1.067780		−1.5	-
2	3.500420		0	-
3	1.669610	(10^{-8})	2	-
1000	1.012580		-	2.24245 (10^3)

Table B.13. Coefficients and exponents for the ideal gas heat capacity equation for Nitrogen.

k	N_k		i_k	A_k
1	−8.37079888737	(10^2)	−3	-
2	3.79147114487	(10^1)	−2	-
3	−6.01737844275	(10^{-1})	−1	-
4	3.50418363823		0	-
5	−8.74955653028	(10^{-6})	1	-
6	1.48958507239	(10^{-8})	2	-
7	−2.56370354277	(10^{-12})	3	-
1000	1.00773735767		-	3.3534061 (10^3)

Thermophysical properties evaluation method

The methodology used for the evaluation of the thermophysical properties is shown in Figure B.1. The input for the evaluation procedure are pressure and temperature, but it can be used any two properties among pressure, temperature and density. The methodology uses conditional statements (IF-THEN-ELSE) to determine the thermodynamic state of the input data (P_v, T_j). Once the thermodynamic state is determined, Eq. (B.10) is solved for ρ_j, given the pressure P_v and temperature T_j.
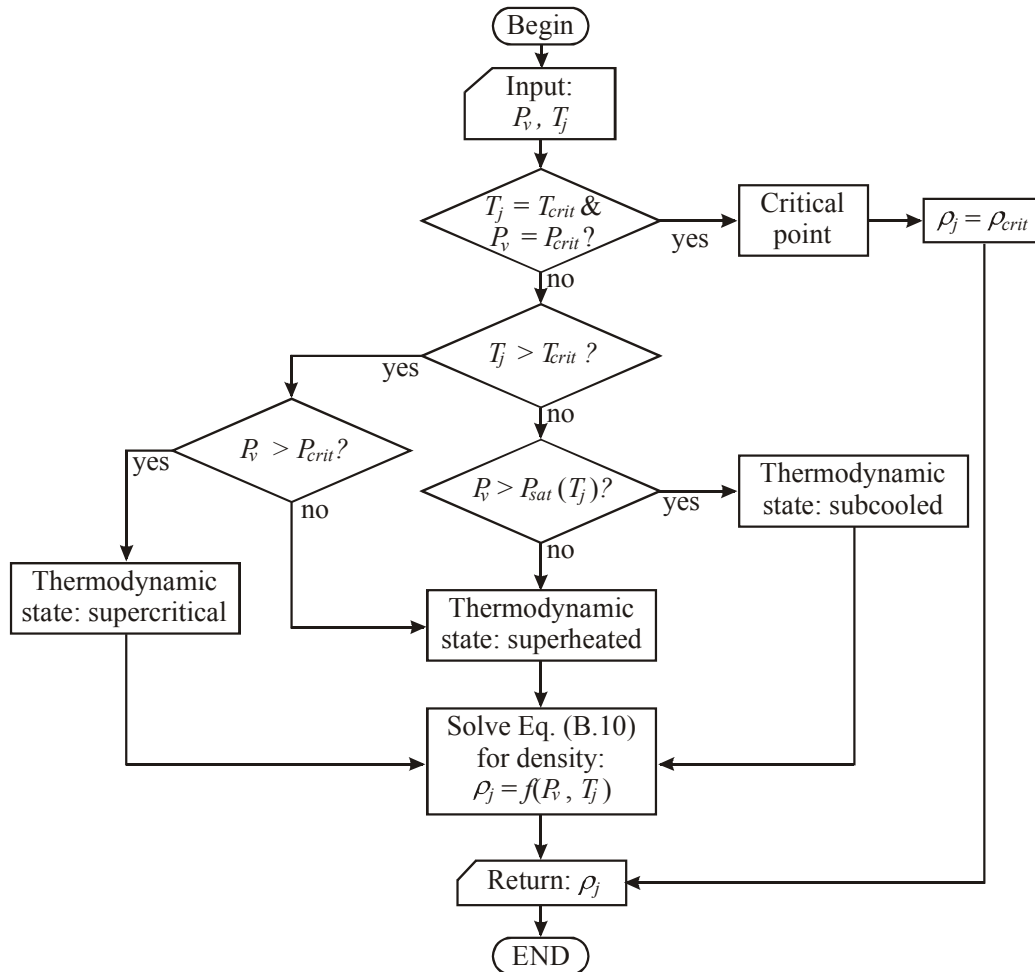
Figure B.1. Thermophysical properties evaluation method.

Latent heat of vaporization evaluation

The latent heat of vaporization (h_{fg}) is calculated only at temperatures below the critical temperature. For a given temperature T_j, the saturated liquid and vapor densities are obtained from Eq. (B.18) and Eq. (B.20) (or B.21). With the pairs [T_j, ρ_l] and [T_j, ρ_v] Eq. (B.12) is used to calculate the saturated liquid and vapor enthalpies, h_ℓ and h_v. The latent heat of vaporization is then obtained from

$$h_{fg} = h_v - h_\ell \tag{B.24}$$

Liquid viscosity and surface tension evaluation

The dynamic viscosity of the saturated liquid, μ_ℓ, and the surface tension, σ, required to determine the average liquid velocity in the liquid column in section 3.3.3 were obtained by a lest-square fit of polynomial expressions to experimental data available at Barron (1985). The resulting equation for the surface tension for Oxygen and Nitrogen, respectively are:

$$\sigma_{oxygen} = 0.04053 - (3.60848 \times 10^{-4})\, T + (6.17419 \times 10^{-7})\, T^2 \qquad \text{(B.25)}$$

$$\sigma_{nitrogen} = 0.03234 - (3.77697 \times 10^{-4})\, T + (9.47003 \times 10^{-7})\, T^2 \qquad \text{(B.26)}$$

and for the dynamic viscosity:

$$\mu_{\ell,\,oxygen} = 0.00228 - (4.99026 \times 10^{-5})\, T + (3.92486 \times 10^{-7})\, T^2 - (1.06039 \times 10^{-9})\, T^3 \quad \text{(B.27)}$$

$$\mu_{\ell,\,nitrogen} = 0.00225 - (5.69858 \times 10^{-5})\, T + 5.04938 \times 10^{-7})\, T^2 - (1.51807 \times 10^{-9})\, T^3 \quad \text{(B.28)}$$

Figures B.2 and B.3 shows the fitting results.
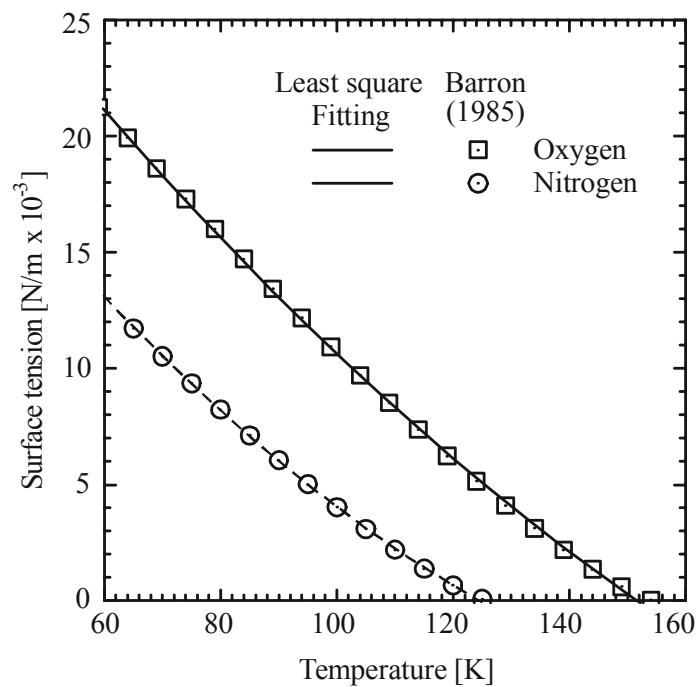
Figure B.2. Least square fitting to the surface tension experimental data.
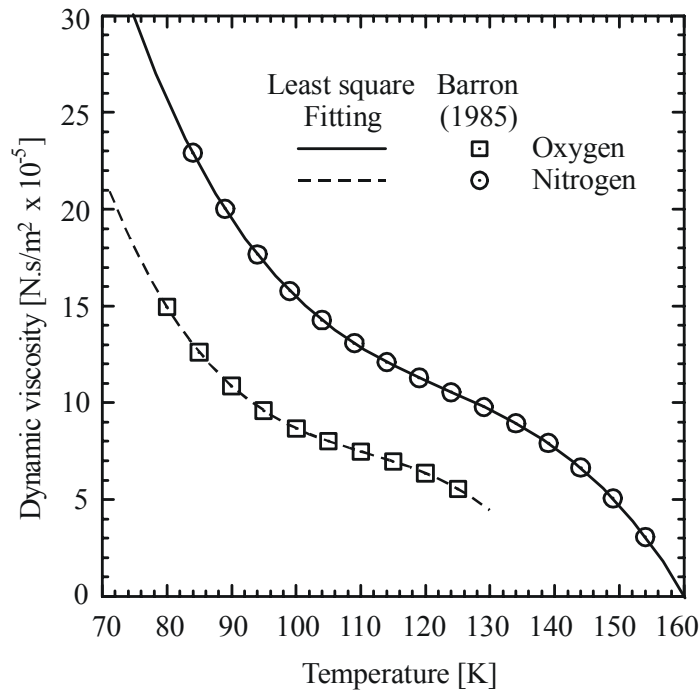
Figure B.3. Least square fitting to the dynamic viscosity experimental data.

Solid wall thermophysical properties

The conductivity, k_s, and the specific heat, c_s, of the solid wall were obtained by a lest-square fit of polynomial expressions to experimental data available at Faghri (1995). The aluminum alloy 2024-T6 data was fitted in three blocks, as shown in Figure B.4. The resulting equation for the aluminum alloy thermal conductivity is:

$$k_{s,\text{aluminum}} = 0.11 + 0.887\,T - 0.0026\,T^2; \quad \text{for } T \leq 80 \text{ K}$$

$$k_{s,\text{aluminum}} = 45.213 - 0.2004\,T + 0.003947\,T^2; \qquad \text{for } 80 \text{ K} < T \leq 200 \text{ K} \qquad \text{(B.29)}$$

$$k_{s,\text{aluminum}} = 140 + 0.115\,T; \qquad\qquad \text{for } T > 200 \text{ K}$$

The equation for the stainless steel 304 thermal conductivity is:

$$k_{s,\text{ss304}} = 4.81543 + 0.04828\,T - 4.94443 \times 10^{-5}\,T^2; \text{ for } 100 \text{ K} < T \leq 300 \text{ K} \qquad \text{(B.30)}$$

and the equation for the thermal conductivity of the titanium is:

$$k_{s,\text{titanium}} = 39.54322 - 0.10413\,T + 1.52828 \times 10^{-4}\,T^2; \quad \text{for } 100 \text{ K} < T \leq 300 \text{ K} \qquad \text{(B.31)}$$
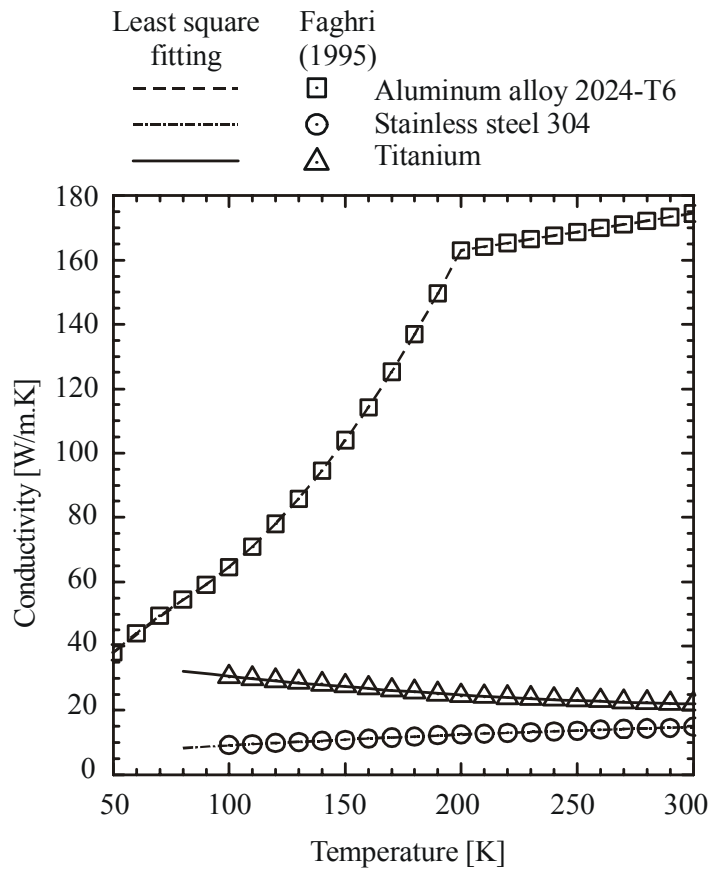
Figure B.4. Thermal conductivity of metals.

The equations for the specific heat of aluminum alloy 2024-T6, stainless steel 304, and titanium are, respectively:

$$c_{s,\text{aluminum}} = -0.40735 + (0.01299)\,T - (4.78084 \times 10^{-5})\,T^2 + (6.17984 \times 10^{-8})\,T^3$$
$$\text{for } 50\text{ K} < T \leq 300\text{ K} \tag{B.32}$$

$$c_{s,\text{ss304}} = 0.09277 + (0.00201)\,T - (2.47221 \times 10^{-6})\,T^2 + (4.63221 \times 10^{-23})\,T^3$$
$$\text{for } 100\text{ K} < T \leq 300\text{ K} \tag{B.33}$$

$$c_{s,\text{aluminum}} = 0.03833 + (0.00305)\,T - (4.85453 \times 10^{-6})\,T^2 + (9.92617 \times 10^{-23})\,T^3$$
$$\text{for } 100\text{ K} < T \leq 300\text{ K} \tag{B.34}$$

Figure B.5 shown the results of the specific heat least square fitting. The density variation with temperature for these metals was neglected. The constant value for the metals density is shown in Table B.14.

Least square fitting	Faghri (1995)	
– – – – –	□	Aluminum alloy 2024-T6
–··–··–··–	⊙	Stainless steel 304
————	△	Titanium
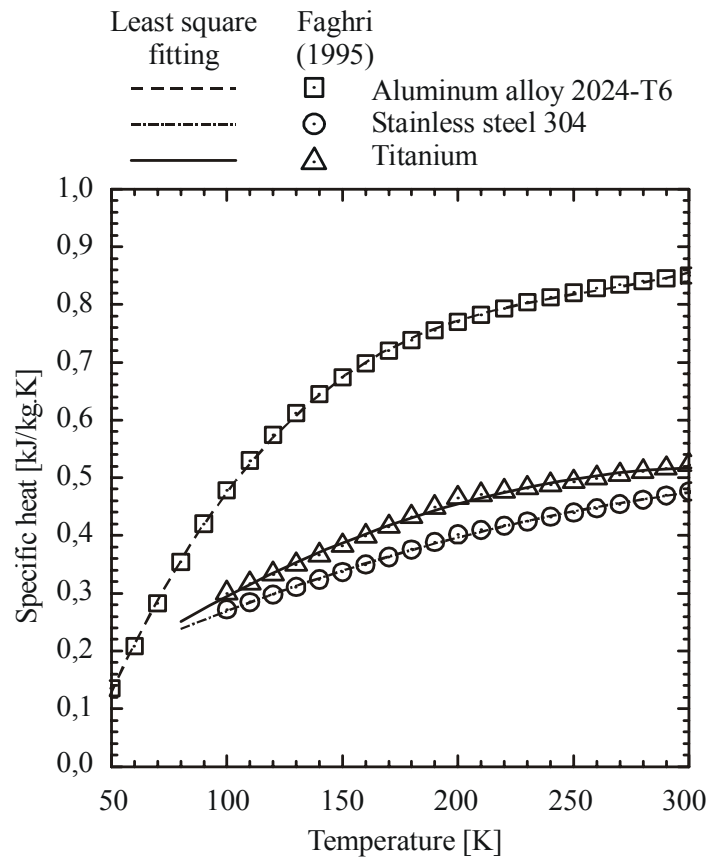
Figure B.5. Specific heat of metals.

Table B.14. Density of metals.

Metal	Density
Aluminum alloy 2024-T6	2770 kg/m^3
Stainless steel 304	7900 kg/m^3
Titanium	4510 kg/m^3

Appendix C
Derivation of the Discrete Equations for the Numerical Solution Method.

The following section shows the discretization of the one dimensional heat conduction equation used on the modeling of the supercritical start-up of cryogenic heat pipes. The finite volume methods described by Patankar (1980) and Maliska (1995) is considered. The basis of this method is to divide the entire domain (heat pipe) into finite volumes, and then, integrate the heat transfer equation inside each volume.

1st stage of the start-up process:

The one-dimensional, transient, heat conduction equation with source term is:

$$\frac{\partial[(\rho c)_{eff} T]}{\partial t} = \frac{\partial}{\partial x}\left(k_s \frac{\partial T}{\partial x}\right) + \frac{S}{A_t L} \tag{C.1}$$

where $T(x,t)$ is a function of position x and time t, $(\rho c)_{eff}$ is the effective heat capacity of the heat pipe, k_s is the thermal conductivity of the solid wall, S is the parasitic heat load source, A_t is the cross sectional area of the solid wall and L is the length of the heat pipe. In this work, the source term S on Eq. (C.1) accounts for radiative heat leaks, but terms to account for radial conductive heat leaks, and time variable heat flux from power dissipation of electronic equipment, can be easily included:

$$S = \sigma \varepsilon F A_e (T_\infty^4 - T^4) + k_s A_c \frac{\partial T}{\partial y} + q(t) \tag{C.2}$$

where σ is the Steffan-Boltzmann constant, F is the view factor between the heat pipe and the surrounding environment, A_e is the external area (emission area) of the heat pipe, ε is the emissivity of its external wall, T_∞ is the temperature of the surrounding environment, k_s is the

conductivity of physical support of the heat pipe, A_c is the conductivity area of this support, and $q(t)$ is a time variable heat flux.

The boundary conditions considered here are time variable temperature specified at $x = 0$, and insulation at $x = L$:

$$T(0,t) = T_c(t); \text{ at } x = 0 \tag{C.3}$$

$$\left.\frac{\partial T}{\partial x}\right|_{x=L} = 0 \text{ ; at } x = L \tag{C.4}$$

Figure C.1 shows the grid used for the discretization of Eq. (C.1). Three different equations are derived: one for the inner volumes, and one for each extreme volume, including the boundary conditions.
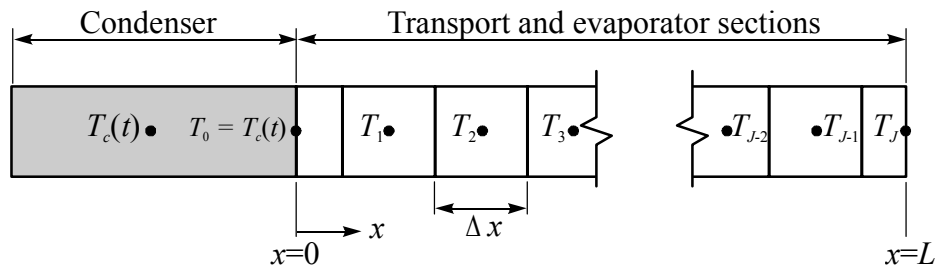
Figure C.1. Grid used for the derivation of the discrete equations (1st stage).

General Equation for the 1st stage of the start-up process:

The general equation is obtained by the integration of Eq. (C.1) inside any volume j, such that $1 < j < J$. The integration volume is called "P" and the boundaries volumes are called "W" and "E" (West and East, respectively). The boundaries of the volume P are called "w" and "e". Figure C.2 shows the grid used for the derivation of the general equation.
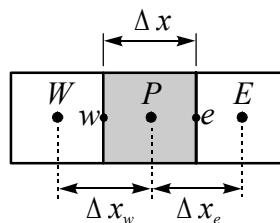
Figure C.2. Grid for the general equation derivation.

It is important to observe that the source term S has a non-linearity in the radiative heat transfer term (T^4). Therefore, a linearization procedure is required. The most common linearization procedure is to expand the source term in a Taylor Series (Patankar, 1980):

$$S = S^k + \frac{dS}{dT}\bigg|_P^k (T_P - T_P^k)$$

(C.5)

Where k represents the temperature available at the last iteration. The substitution of Eq. (C.2) into Eq. (C.5) provides:

$$S = \left[\sigma \varepsilon F A_e (T_\infty^4 + 3T^4) + \frac{k_s A_c T_s}{\Delta y} + q(t) \right] - \left[4\sigma \varepsilon F A_e T_p^{k4} + \frac{k_s A_c}{\Delta y} \right] T_P$$

(C.6)

which can be rewritten as:

$$S = S_c + S_P T_P$$

(C.7)

The integration of Eq. (C.1) inside the volume P provides:

$$\int_t^{t+\Delta t} \int_w^e \frac{\partial}{\partial t}[(\rho c)_{eff} T] dx dt = \int_t^{t+\Delta t} \int_w^e \frac{\partial}{\partial x}\left(k_s \frac{\partial T}{\partial x} \right) dx dt + \int_t^{t+\Delta t} \int_w^e \frac{S_P T_P + S_c}{A_t L} dx dt$$

(C.8)

The integration inside the volume gives:

$$\int_t^{t+\Delta t} \frac{\partial}{\partial t}[(\rho c)_{eff} T] \Delta x dt = \int_t^{t+\Delta t}\left[\left(k_s \frac{\partial T}{\partial x} \right)_{x=e} - \left(k_s \frac{\partial T}{\partial x} \right)_{x=w} \right] dt + \int_t^{t+\Delta t}\left[\frac{S_P T_P + S_c}{A_t L} \right] \Delta x dt$$

(C.9)

Using a fully implicit scheme for the time integration, Eq. (C.9) turns into:

$$[(\rho c)_{eff} T_P - (\rho c)_{eff}^0 T_P^0]\Delta x = \left[\left(k_s \frac{\partial T}{\partial x} \right)_{x=e} - \left(k_s \frac{\partial T}{\partial x} \right)_{x=w} \right]\Delta t + \left[\frac{S_P T_P + S_c}{A_t L} \right]\Delta x \Delta t$$

(C.10)

The superscript 0 (zero) in Eq. (C.10) denotes the temperature and thermal capacity evaluated at the last time step. The derivatives of the temperature with respect to position at the faces of the volume can be written as:

$$\frac{\partial T}{\partial x}\bigg|_{x=e} = \frac{T_E - T_P}{\Delta x_e} \text{ ; and } \frac{\partial T}{\partial x}\bigg|_{x=w} = \frac{T_P - T_W}{\Delta x_w}$$

(C.11)

The substitution of Eq. (C.11) into Eq. (C.10) provides:

$$[(\rho c)_{eff} T_P - (\rho c)_{eff}^0 T_P^0]\Delta x = \left[k_s(T_e)\frac{T_E - T_P}{\Delta x_e} - k_s(T_w)\frac{T_P - T_W}{\Delta x_w}\right]\Delta t + \left[\frac{S_P T_P + S_c}{A_t L}\right]\Delta x \Delta t \quad \text{(C.12)}$$

where:

$$\frac{T_e - T_P}{T_E - T_P} = \frac{\Delta x / 2}{\Delta x_e} \; ; \text{and} \; \frac{T_w - T_P}{T_W - T_P} = \frac{\Delta x / 2}{\Delta x_w}$$

Collecting T_P^0, T_P, T_E and T_W, considering that $\Delta x_e = \Delta x_w = \Delta x$, and rearranging the terms, the final form for equation (C.12) is:

$$\left[(\rho c)_{eff}^0\right]T_P^0 = T_P\left[\frac{k_s(T_w)\Delta t}{\Delta x^2} + \frac{k_s(T_e)\Delta t}{\Delta x^2} - \frac{S_P \Delta t}{A_t L} + (\rho c_p)_{eff}\right] + \\ - T_W\left[\frac{k_s(T_w)\Delta t}{\Delta x^2}\right] - T_E\left[\frac{k_s(T_e)\Delta t}{\Delta x^2}\right] - \left[\frac{S_c \Delta t}{A_t L}\right] \quad \text{(C.13)}$$

and:

$$T_e = \frac{T_E + T_P}{2} \; ; \text{and} \; T_w = \frac{T_W + T_P}{2}$$

or simply:

$$T_P^0 = A_w T_W + A_P T_P + A_e T_E + B \quad \text{(C.14)}$$

where:

$$A_P = \frac{k_s(T_w)\Delta t}{A_P^0 \Delta x^2} + \frac{k_s(T_e)\Delta t}{A_P^0 \Delta x^2} - \frac{S_P \Delta t}{A_P^0 A_t L} + \frac{(\rho c)_{eff}}{A_P^0}$$

$$A_W = -\frac{k_s(T_w)\Delta t}{A_P^0 \Delta x^2} \; ; \; A_E = -\frac{k_s(T_e)\Delta t}{A_P^0 \Delta x^2} \; ; \; B = -\frac{S_c \Delta t}{A_P^0 A_t L} \; ; \text{and} \; A_P^0 = (\rho c)_{eff}^0$$

Boundary condition at $x = 0$ for the 1st stage of the start-up process:

As the boundary condition at $x = 0$ is a specified temperature, there is no need to create an equation for the volume $j = 0$ (Figure C.3). To account for the time variation of the temperature at $x = 0$, an equation for the volume $j = 1$ must be written. The derivation process is similar to the previous, but now, the temperature at the point W is not a variable, but it is the specified boundary condition:
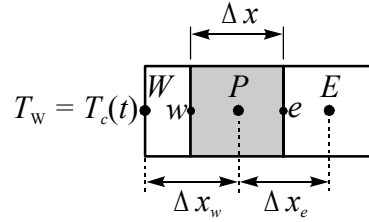
Figure C.3. Grid for the boundary condition at $x = 0$.

$$T_W = T_c(t) \tag{C.15}$$

Therefore, for $j = 1$, Eq. (C.12) can be written as follows:

$$[(\rho c)_{eff} T_P - (\rho c)_{eff}^0 T_P^0]\Delta x = \left[k_s(T_e)\frac{T_E - T_P}{\Delta x_e} - k(T_w)\frac{T_P - T_c(t)}{\Delta x_w} \right]\Delta t + \left[\frac{S_P T_P + S_c}{A_t L} \right]\Delta x \Delta t \tag{C.16}$$

Considering that $\Delta x_e = \Delta x_w = \Delta x$, Eq. (C.16) can be rearranged to the following form:

$$\begin{aligned} \left[(\rho c)_{eff}^0\right]T_P^0 = T_P\left[\frac{k(T_w)\Delta t}{\Delta x^2} + \frac{k(T_e)\Delta t}{\Delta x^2} - \frac{S_P \Delta t}{A_t L} + (\rho c)_{eff} \right] + \\ -T_E\left[\frac{k(T_e)\Delta t}{\Delta x^2} \right] - \left[\frac{S_c \Delta t}{A_t L} + T_c(t)\frac{k(T_w)\Delta t}{\Delta x^2} \right] \end{aligned} \tag{C.17}$$

and:

$$T_e = \frac{T_E + T_P}{2} \; ; \text{and } T_w = \frac{T_c(t) + T_P}{2}$$

Equation (C.17) can be written in a more simplified form:

$$T_P^0 = A_P T_P + A_e T_E + B \tag{C.18}$$

where:

$$A_P = \frac{k(T_w)\Delta t}{A_P^0 \Delta x^2} + \frac{k(T_e)\Delta t}{A_P^0 \Delta x^2} - \frac{S_P \Delta t}{A_P^0 A_t L} + \frac{(\rho c)_{eff}}{A_P^0}$$

$$A_E = -\frac{k(T_e)\Delta t}{A_P^0 \Delta x^2}; \quad B = -\left[\frac{S_c \Delta t}{A_P^0 A_t L} + T_c(t)\frac{k(T_w)\Delta t}{A_P^0 \Delta x^2}\right]; \text{ and } A_P^0 = (\rho c)_{eff}^0$$

Boundary condition at $x = L$ for the 1st stage of the start-up process:

The boundary condition at $x = L$ is $\partial T/\partial x|_{x=L} = 0$. Therefore, an equation for the last volume (at $j = J$) is required to account for the zero heat flux at $x = L$ (Figure C.4). It is important to note that the last volume has a length of $\Delta x/2$, and Eq. (C.1) must be integrated between w and P.

$$\int_t^{t+\Delta t} \int_w^P \frac{\partial}{\partial t}[(\rho c)_{eff} T]dxdt = \int_t^{t+\Delta t} \int_w^P \frac{\partial}{\partial x}\left(k_s \frac{\partial T}{\partial x}\right)dxdt + \int_t^{t+\Delta t} \int_w^P \frac{S_P T_P + S_c}{A_t L}dxdt \qquad (C.19)$$
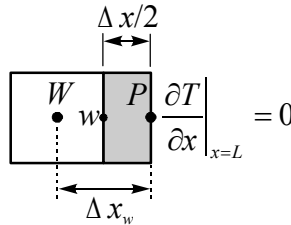
Figure C.4. Grid for the boundary condition at $x = L$.

The integration in space and time of Eq. (C.19) provides:

$$[(\rho c)_{eff} T_P - (\rho c)_{eff}^0 T_P^0]\frac{\Delta x}{2} = \left[\underbrace{\left(k_s \frac{\partial T}{\partial x}\right)_{x=P}}_{0 \text{ (B.C.)}} - \left(k_s \frac{\partial T}{\partial x}\right)_{x=w}\right]\Delta t + \left[\frac{S_P T_P + S_c}{A_t L}\right]\frac{\Delta x}{2}\Delta t \qquad (C.20)$$

The derivative at $x = w$ is identical to Eq. (C.11).

$$[(\rho c)_{eff} T_P - (\rho c)_{eff}^0 T_P^0]\frac{\Delta x}{2} = \left[-k_s(T_w)\frac{T_P - T_W}{\Delta x_w}\right]\Delta t + \left[\frac{S_P T_P + S_c}{A_t L}\right]\frac{\Delta x}{2}\Delta t \qquad (C.21)$$

Equation (C.21) can be rearranged in the following form:

$$T_P^0\left[(\rho c)_{eff}^0\right] = T_P\left[\frac{2k_s(T_w)\Delta t}{\Delta x^2} - \frac{S_P\Delta t}{A_t L} + (\rho c_p)_{eff}\right] - T_W\left[\frac{2k_s(T_w)\Delta t}{\Delta x^2}\right] - \left[\frac{S_c\Delta t}{A_t L}\right] \qquad (C.22)$$

or:

$$T_P^0 = A_P T_P + A_w T_W + B \qquad (C.23)$$

where:

$$A_P = \frac{2k_s(T_w)\Delta t}{A_P^0 \Delta x^2} - \frac{S_P\Delta t}{A_P^0 A_t L} + \frac{(\rho c)_{eff}}{A_P^0}$$

$$A_W = -\frac{2k_s(T_w)\Delta t}{A_P^0 \Delta x^2} ; \quad B = -\frac{S_c\Delta t}{A_P^0 A_t L} ; \text{ and } A_P^0 = (\rho c)_{eff}^0$$

Equation (C.18) is valid for $j = 1$, Eq. (C.14) for $1 < j < J$, and Eq. (C.23) for $j = J$. This set of equations can be written in a matrix form as follows:

$$[T^0] = [A][T] + [B] \qquad (C.24)$$

where the only unknown is the matrix $[T]$. The solution of Eq. (C.24) is:

$$[T] = [A]^{-1}([T^0] + [B]) \qquad (C.25)$$

2nd stage of the start-up process:

The one-dimensional, transient, heat conduction equation with source term for the 2nd stage of the supercritical start-up of a cryogenic heat pipe is identical to Eq. (C.1). Figure C.5 shows the general grid for the discretization of the 2nd stage of the start-up. Now, the boundary condition at the condenser is a moving boundary condition, given by:

$$T(x,t) = T_c(t); \text{ at } x = s(t) - L_c \qquad (C.26)$$

The position of the liquid column as a function of time, $s(t)$, is given by the solution of the following heat balance equation:

$$\left(k_s A_s \frac{\partial T}{\partial x}\right)_{x=s-L_c} = \left[\rho_\ell A_\ell h_{fg}\left(U - \frac{ds}{dt}\right)\right]_{x=s-L_c} \qquad \text{(C.27)}$$

Again, the discretization of Eq. (C.1) for the 2nd stage of the supercritical start-up provides three different equations: one general and one for each boundary condition. The general equation is identical to Eq. (C.14) and the equation for the boundary at $x = L$ is identical to Eq. (C.23).
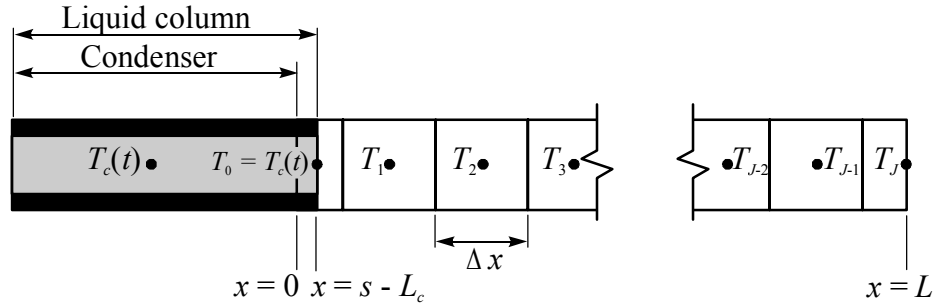
Figure C.5. Grid used for the derivation of the discrete equations (2nd stage).

Boundary condition at $x = s(t) - L_c$ for the 2nd stage of the start-up process:

The equation for $x = s(t) - L_c$ must account for the moving boundary. Figure C.6 shows the grid used for the derivation of this equation. It is important to observe that $\Delta x_e = \Delta x$, but $\Delta x_w \neq \Delta x$ because the boundary at $x = s(t) - L_c$ is moving.
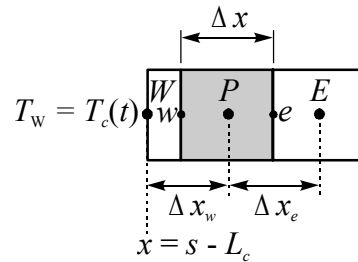
Figure B.6. Grid for the boundary condition at $x = s(t) - L_c$.

Eq. (C.1) is integrated between $x = w$ and $x = e$:

$$\int_t^{t+\Delta t} \int_w^e \frac{\partial}{\partial t}[(\rho c)_{eff} T]\,dxdt = \int_t^{t+\Delta t} \int_w^e \frac{\partial}{\partial x}\left(k_s \frac{\partial T}{\partial x}\right)dxdt + \int_t^{t+\Delta t} \int_w^e \frac{S_P T_P + S_c}{A_t L}\,dxdt \qquad \text{(C.28)}$$

which results in:

$$[(\rho c)_{eff} T_P - (\rho c)^0_{eff} T^0_P] \Delta x = \left[k_s(T_e) \frac{T_E - T_P}{\Delta x} - k_s(T_w) \frac{T_P - T_c(t)}{\Delta x_w} \right] \Delta t + \left[\frac{S_P T_P + S_c}{A_t L} \right] \Delta x \Delta t \quad \text{(C.29)}$$

Rearranging the terms, E. (C.29) can be rewritten as:

$$\left[(\rho c)^0_{eff} \right] T^0_P = T_P \left[\frac{k_s(T_e) \Delta t}{\Delta x^2} + \frac{k_s(T_w) \Delta t}{\Delta x \Delta x_w} - \frac{S_P \Delta t}{A_t L} + (\rho c)_{eff} \right] +$$
$$- T_E \left[\frac{k_s(T_e) \Delta t}{\Delta x^2} \right] - \left[\frac{S_c \Delta t}{A_t L} + T_c(t) \frac{k_s(T_w) \Delta t}{\Delta x \Delta x_w} \right] \quad \text{(C.30)}$$

and:

$$T_e = \frac{T_E + T_P}{2} \text{ ; and } T_w = \frac{\Delta x}{2} \left(\frac{T_W - T_P}{\Delta x_w} \right) + T_P$$

or:

$$T^0_P = A_P T_P + A_e T_E + B \quad \text{(C.31)}$$

where:

$$A_P = \frac{k_s(T_e) \Delta t}{A^0_P \Delta x^2} + \frac{k_s(T_w) \Delta t}{A^0_P \Delta x \Delta x_w} - \frac{S_P \Delta t}{A^0_P A_t L} + \frac{(\rho c)_{eff}}{A^0_P}$$

$$A_E = - \frac{k_s(T_e) \Delta t}{A^0_P \Delta x^2} \text{ ; } B = - \left[\frac{S_c \Delta t}{A^0_P A_t L} + T_c(t) \frac{k_s(T_w) \Delta t}{A^0_P \Delta x \Delta x_w} \right] \text{; and } A^0_P = (\rho c)^0_{eff}$$

The length Δx_w needed for Eq. (C.31) is obtained according to Figure C.7. The length of the liquid column, $s(t) - L_c$, is divided by the length of the volumes, Δx. The nearest integer to this ratio shows the volume in which the liquid column leading edge is, J_v:

$$J_v = \text{Round} \left(\frac{s(t) - L_c}{\Delta x} \right) \quad \text{(C.32)}$$
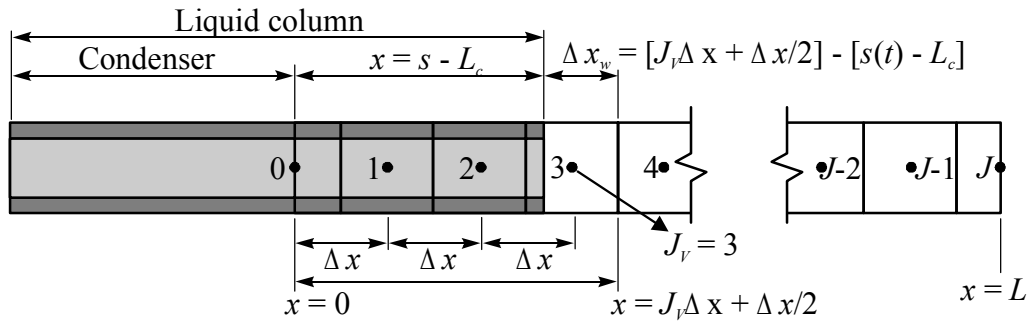
Figure C.7. Determination of Δx_w.

Then, the length Δx_w can be obtained by:

$$\Delta x_w = \left[J_V \Delta x + \frac{\Delta x}{2} \right] - \left[s(t) - L_c \right] \tag{C.33}$$

Discretization for $J_V = J - 2$:

According to Figure C.8, when the liquid column reaches the volume $J - 2$, only two equations are required: one for the volume $J - 1$ and another for the volume J. These equations are identical to Eqs. (C.31) and (C.23) respectively.
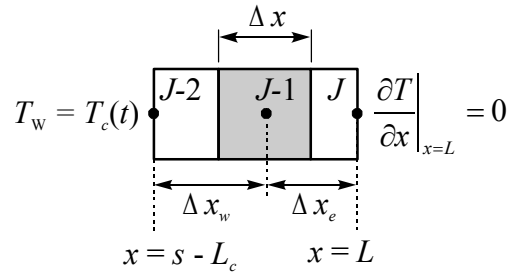
Figure C.8. Discretization when $J_V = J - 2$.

Discretization for $J_V = J - 1$:

When the liquid column reaches the volume $J - 1$, only one equation for the volume J is needed (see Figure C.9). The discretization of Eq. (C.1) is done by integrating this equation between w and P, as follows:

$$\int_{t}^{t+\Delta t} \int_{w}^{P} \frac{\partial}{\partial t} [(\rho c)_{eff} T] dx dt = \int_{t}^{t+\Delta t} \int_{w}^{P} \frac{\partial}{\partial x} \left(k_s \frac{\partial T}{\partial x} \right) dx dt + \int_{t}^{t+\Delta t} \int_{w}^{P} \frac{S_P T_P + S_c}{A_t L} dx dt \tag{C.34}$$

$$[(\rho c)_{eff} T_P - (\rho c)_{eff}^0 T_P^0] \frac{\Delta x}{2} = \left[\left(k_s \frac{\partial T}{\partial x} \right)_{x=P} - \left(k_s \frac{\partial T}{\partial x} \right)_{x=w} \right] \Delta t + \left[\frac{S_P T_P + S_c}{A_t L} \right] \frac{\Delta x}{2} \Delta t \tag{C.35}$$

0 (B.C.)

$$T_W = T_c(t) \quad \frac{\partial T}{\partial x}\bigg|_{x=L} = 0$$
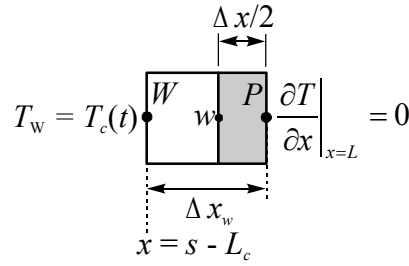
Figure C.9. Discretization for $J_V = J - 1$.

The derivative at $x = w$ is similar to Eq. (C.11):

$$[(\rho c)_{eff} T_P - (\rho c)_{eff}^0 T_P^0]\frac{\Delta x}{2} = \left[-k_s(T_w)\frac{T_P - T_c(t)}{\Delta x_w}\right]\Delta t + \left[\frac{S_P T_P + S_c}{A_t L}\right]\frac{\Delta x}{2}\Delta t \qquad (C.36)$$

Equation (C.36) can be rearranged in the following form:

$$T_P^0\left[(\rho c)_{eff}^0\right] = T_P\left[\frac{2k_s(T_w)\Delta t}{\Delta x \Delta x_w} - \frac{S_P \Delta t}{A_t L} + (\rho c)_{eff}\right] - T_c(t)\left[\frac{2k_s(T_w)\Delta t}{\Delta x \Delta x_w}\right] - \left[\frac{S_c \Delta t}{A_t L}\right] \qquad (C.37)$$

or:

$$T_P^0 = A_P T_P + B \qquad (C.38)$$

where:

$$A_P = \frac{2k_s(T_w)\Delta t}{A_P^0 \Delta x \Delta x_w} - \frac{S_P \Delta t}{A_P^0 A_t L} + \frac{(\rho c)_{eff}}{A_P^0}; \quad B = -\left[T_c(t)\frac{2k_s(T_w)\Delta t}{A_P^0 \Delta x \Delta x_w} + \frac{S_c \Delta t}{A_P^0 A_t L}\right]; \text{ and } A_P^0 = (\rho c)_{eff}^0$$

Eqs. (C.31), (C.38), and the other equations required for the 2nd stage of the supercritical start-up of a cryogenic heat pipe can be written in a matrix for, as expressed by Eq. (C.24), whose solution is given by Eq. (C.25).

Liquid column discretization:

Equation (C.27) is discretized as follows:

$$k_s(T_w)A_s \frac{T_c(t) - T_P}{\Delta x_w} = \rho_\ell h_{fg} A_w\left(U - \frac{s - s_0}{\Delta t}\right) \qquad (C.39)$$

where s_0 is the position of the liquid column in the beginning of the time step Δt. The position s is then obtained from:

$$s = s_0 + U\Delta t - \frac{k_s(T_w)A_s\Delta t}{\rho_\ell h_{fg}A_w\Delta x_w}\left[T_c(t) - T_P\right] \qquad (C.40)$$

It is important to observe that in the finite volume equations derived here, the conductivity of the solid wall (k_s) is evaluated at the interfaces of the volumes at T_e and T_w, respectively, while the effective heat capacity [$(\rho c)_{eff}$] is evaluated at the center of the volume at T_P. The density of the saturated liquid (ρ_ℓ) and the latent heat of vaporization (h_{fg}) in Eq. (C.40) are evaluated at the condenser temperature, $T_c(t)$.

The start-up limitation for an axially grooved cryogenic heat pipe is discussed based on the theoretical results given by the thermal model presented in Section 3. The analysis will focus on the effects of the parasitic heat load over the temperature profile and liquid column length, as well as the effects of some geometrical parameter. The TRW heat pipe is considered here. All the geometric parameters were kept equal to those shown in Table 3.1, except when specified.

Figure D.1 shows the effect of the parasitic heat load over the temperature of the heat pipe. The figure shows different transient temperatures for different values of εF. The number inside the brackets in the legend refers to the corresponding parasitic heat load, for a heat pipe isothermal at 60 K, with the same geometry of the TRW heat pipe. Temperatures are shown for three different positions: $x = 0$ (condenser), $x = 0.15$ m (inside the transport section), and $x = L$ (evaporator end).

As it was expected, the priming of the heat pipe is slower as the parasitic heat load increases. It appears that the TRW heat pipe is almost at the edge of the parasitic heat load. It primed for a parasitic heat load of 1.5 W, but did not for a parasitic heat load of 1.9 W and above (see Figs. 3.9 and 3.12, in Section 3). It is important to note that the TRW heat pipe was specifically designed to have a low transport capability such that data could be obtained for analytical model validation.

The position of the liquid column as a function of the start-up time is shown in Fig. D.2. If there is no parasitic heat load, the heat pipe will prime completely in 3.67 h. The time that the liquid column stays stagnated in the interface between the condenser and the transport section is 11 min for no parasitic heat load, up to 15 min. for 2.9 W. In the later case, only 0.82 m of the heat pipe could be primed.

Figure D.3 presents the effect of the condenser length on the transient temperature of the heat pipe during the start-up. The time for the complete priming of the heat pipe decreases as the relative length of the condenser increases. This occurs because a longer condenser

corresponds to a larger heat pipe length being cooled directly. The position of the liquid column as a function of time is presented at Fig. D.4.
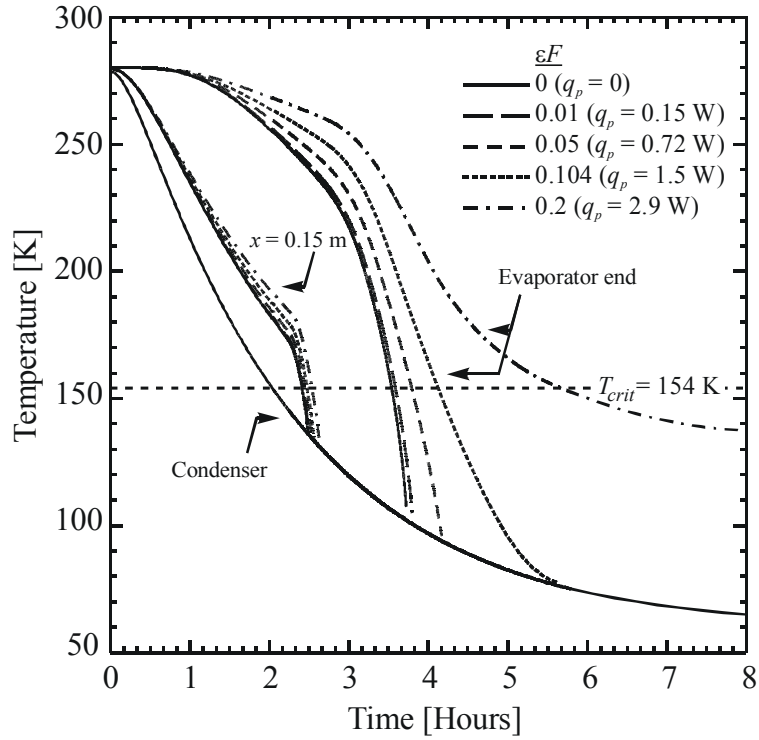
Figure D.1. Effects of the parasitic heat load.
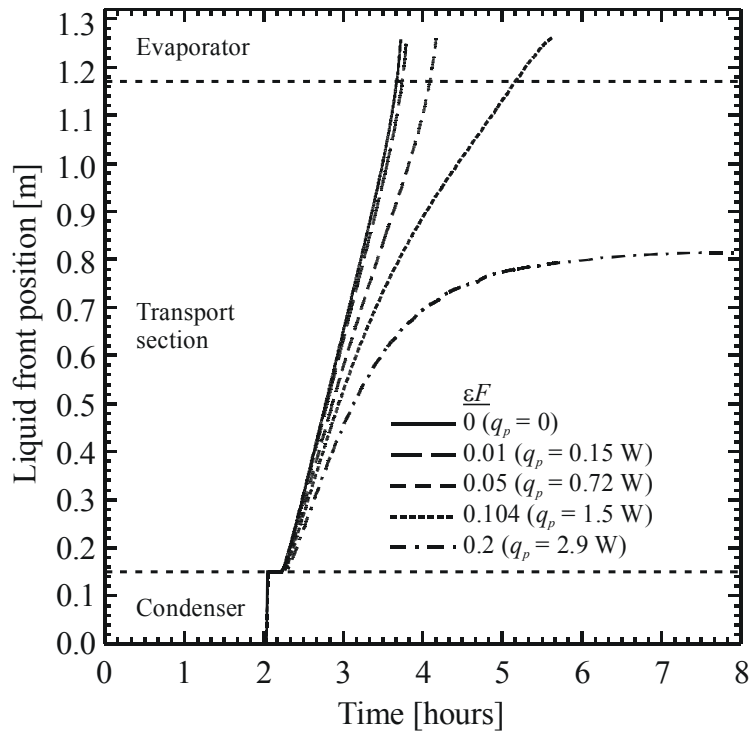
Figure D.2. Liquid column length.
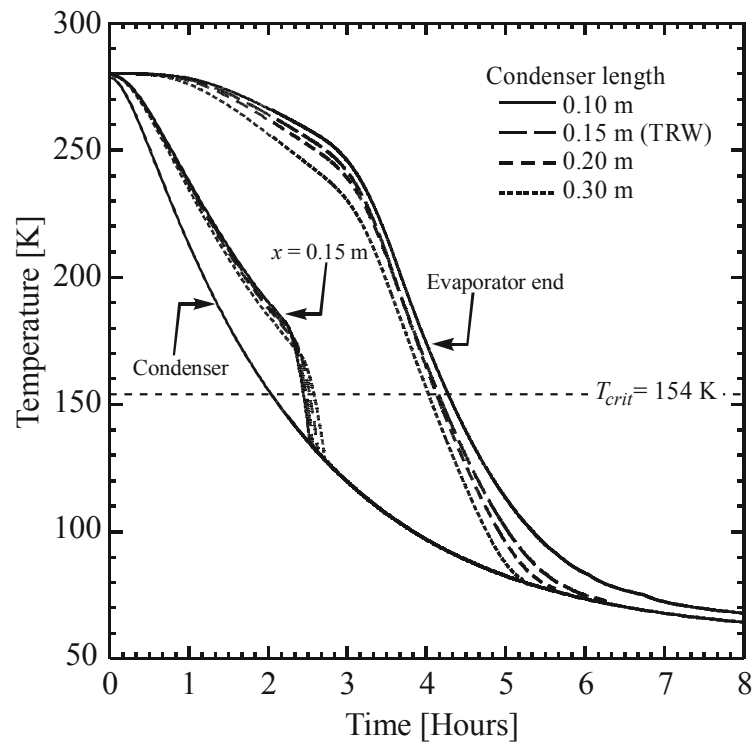
Figure D.3. Effects of the condenser length.
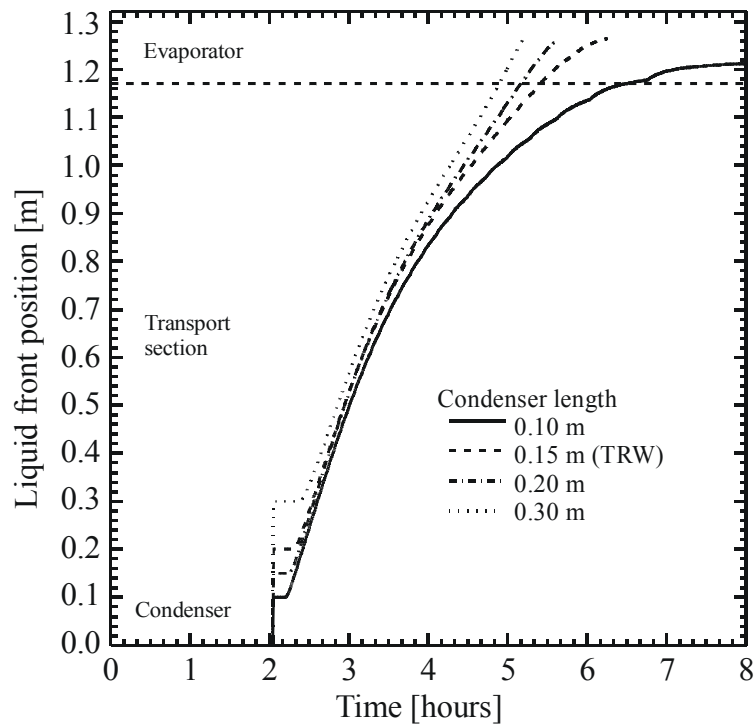
Figure D.4. Liquid column length.

The effect of the cross sectional area of the groove on the temperatures of the heat pipe is given in Fig. D.5. The aspect ratio for all groove areas presented in this figure is constant and equal to the aspect ratio of the TRW heat pipe ($h/w = 1.8$).

Figure D.6 shows the position of the liquid column for the three groove areas presented in Fig. D.5. For the largest groove area, the start-up time was 4.17 h. For the smallest groove area, steady state was not reached even after 8 h from the beginning of the start-up.
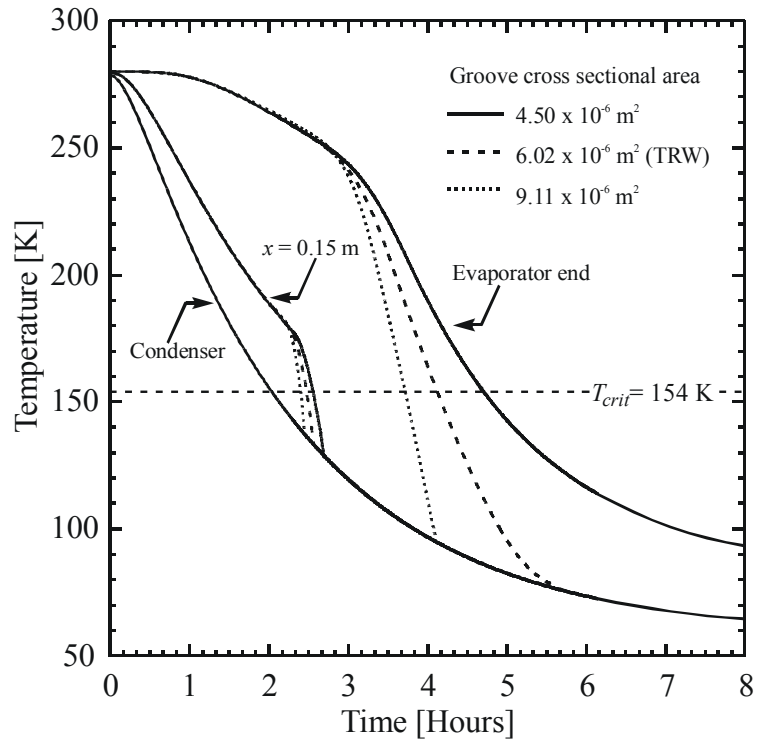
Figure D.5. Effects of groove cross sectional area.
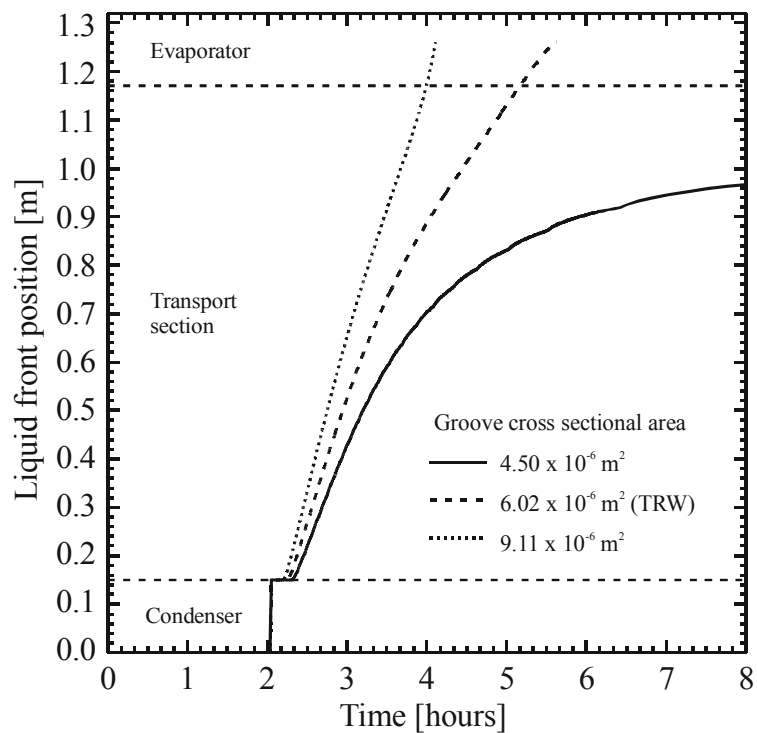
Figure D.6. Liquid column length.

The effect of the external diameter of the heat pipe container on the transient temperature is presented in Fig. D.7. The groove area and the vapor area were kept constant for the three diameters shown in this figure, and their values are the same as those in the TRW heat pipe. A larger external diameter will provide a larger external area of the heat pipe, which will increase the incidence of parasitic heat load. More importantly, the larger diameter corresponds to an increased wall thickness, which increases the thermal mass of the heat pipe. Additionally, the greater wall thickness will increase the heat transfer from the dry region to the liquid column (see Eq. 3.9, Section 3.3.2). Thus, more liquid from the leading edge of the liquid column will be evaporated, decreasing the rewetting velocity. Figure D.8 shows the liquid front position for the three diameters presented in Fig. D.7.
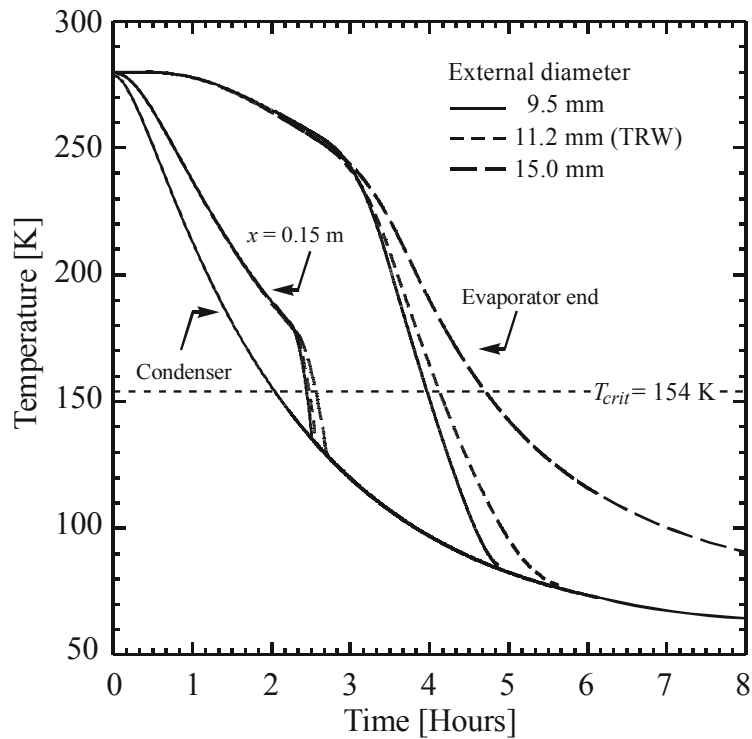
Figure D.7. Effects of the heat pipe external diameter.
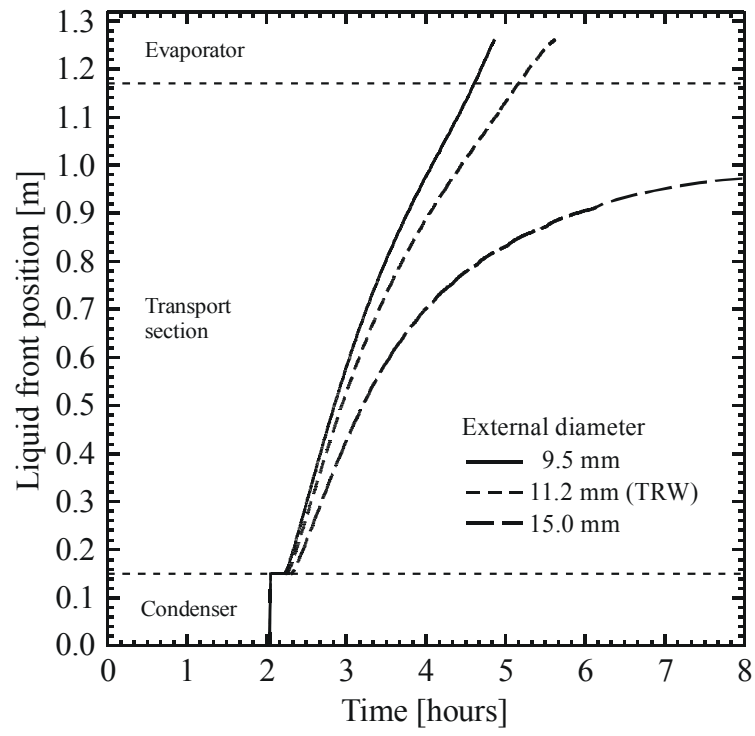
Figure D.8. Liquid column length.

Author Index

Subject Index